1-1-2003

Numerical simulation of unsteady incompressible flow past two-dimensional elliptic cylinders

Ayan Sengupta
Iowa State University

Numerical simulation of unsteady incompressible flow past two-dimensional elliptic cylinders

by

Ayan Sengupta

A thesis submitted to the graduate faculty

in partial fulfillment of the requirements for the degree of

MASTER OF SCIENCE

Major: Aerospace Engineering

Program of Study Committee:
R. Ganesh Rajagopalan, Major Professor
Thomas J. McDaniel
Nicola Elia

Iowa State University

Ames, Iowa

2003

Graduate College
Iowa State University

This is to certify that the master's thesis of

Ayan Sengupta

has met the thesis requirements of Iowa State University

TABLE OF CONTENTS

LIST OF FIGURES

NOMENCLATURE

Lower Case

$a_{i,j}$	coefficients of the discretized equation
$b_{v\xi}, b_{v\eta}$	discretized source terms for the v_ξ and v_η momentum equations
b	general source term in the discretized equation
d	diameter of the cylinder
$\hat{e}_\xi, \hat{e}_\eta$	unit vectors in the body intrinsic coordinates
$\hat{e}_x, \hat{e}_y$	unit vectors in the cartesian coordinates
h_1	scale factor in the ξ-direction
$\vec{n}$	unit normal to symmetry boundary
p	static pressure of the fluid
$p^\star$	latest value of pressure
p'	pressure correction
v_ξ, v_η	components of the velocity vector V
${v_\xi}', {v_\eta}'$	velocity corrections
${v_\xi}^\star, {v_\eta}^\star$	latest values of v_ξ and v_η velocities

$\hat{v}_\xi, \hat{v}_\eta$	pseudo velocities of v_ξ and v_η
x, y	Cartesian coordinate directions

Upper Case

C_p	pressure coefficient
C_f	skin friction coefficient
D	diffusive conductance at control volume face
F	mass flux at the control volume face
L	reference length
NI	number of grid points in the ξ-direction
NJ	number of grid points in the η-direction
P	Peclet number
$R(\xi)$	radius of curvature at ξ
Re	Reynolds number based on L
$S_{v\xi}, S_{v\eta}$	source terms for the u and v momentum equations
T	static temparature of the fluid
V	velocity vector
V_∞	magnitude of freestream velocity
AR	aspect ratio of an ellipse

Greek Symbols

α	scalar constant for time integration
ΔA	area of the control volume
$\Delta\xi, \Delta\eta$	ξ and η width of a control volume
$\delta\xi, \delta\eta$	grid space between adjacent control points
ϵ	η direction grid stretching parameter
μ	coefficient of viscosity
ρ	density of the fluid
$\tilde{\Pi}_{i,j}$	stress tensor
ξ, η	2-D body intrinsic coordinate directions

ACKNOWLEDGEMENTS

First of all I would like to express my sincere appreciation and gratitude to my major professor, Dr. Ganesh Rajagopalan, for his guidance throughout the course of this work. A very special note of thanks to Ashvin for his help during any problems pertaining with the Linux machines. at the Aerospace Engineering department computing lab. I would also like to thank Arindam and Anindya for standing beside me throughout the course of this work. Last, but certainly not the least, I would like to thank my father, mother and brother for their constant support in every possible way.

ABSTRACT

Unsteady algorithms Fully Implicit and Crank Nicholson were developed for body fitted curvilinear coordinate system to study the incompressible flow over two-dimensional ellipses. In addition, explicit cyclic boundary condition was implemented to facilitate analysis of vortex shedding.

Unsteady flow over circular cylinders was simulated for different Reynolds numbers and compared with experimental data. Flow over ellipses was simulated to study the effect of aspect ratio on drag coefficient. It was observed that the drag coefficient increased as the aspect ratio increased reaching an asymptotic value as the ellipse approached a flat plate.

CHAPTER 1 INTRODUCTION

The aim of the present work is to study certain flow characteristics of bluff bodies for a wide range of Reynolds number in the incompressible flow regime. In the present work, only elliptic cylinders are considered.

1.1 Background

The earliest recorded observation of the phenomenon of vortex shedding can be traced back to the sixteenth century when Leonardo da Vinci made drawings of surface pattern of the fluid flow past an obstacle [1]. Up until now, very little has been understood about the formation of vortices that accompany the flow past two- or three-dimensional bluff bodies. This research is an attempt to study the unsteady fluid flow past two-dimensional ellipses in the incompressible regime.

Traditionally, computational methods for Navier-Stokes equations have been developed separately for incompressible and compressible flows. The primary distinction is that almost all the schemes suitable for compressible flows use density as one of the main dependent variables. The difficulty arises when these schemes are used to compute incompressible flows where the density changes are very small. This gives rise to a very large local speed of sound and consequently, the Courant number required for these schemes to remain stable becomes impractical. As a result, most incompressible flow solvers use pressure as one of the dependent variables since pressure changes are always finite for all the Mach numbers.

Current techniques for the solution of incompressible viscous flow can be categorized as: a) vorticity stream-function methods [2], b) artificial incompressible methods [3] and c) projection methods. These formulations generally lead to indirect solution of the discretized continuity equation. This is typically done either by adding 'artificial compressibility' to the continuity equation or by indirectly satisfying the continuity equation with the pressure Poisson equation.

The vorticity stream-function method solves the vorticity transport equation, which is constructed by taking the curl of the momentum equation. The terms containing the pressure may be eliminated by using the components of the equation of motion. The method requires the use of vorticity boundary conditions, which are difficult to implement, and an additional calculation is required if the pressure is desired.

The projection method is a fractional step method in which an intermediate velocity and pressure are calculated. The intermediate pressure and velocity are then corrected sequentially by the pressure gradient and the divergence of the intermediate velocity (continuity equation), respectively. New values for pressure and velocity are obtained until the divergence of the velocity vanishes. The SIMPLE [4, 5] method and all related methods fall in this class. The family of SIMPLE will be given more importance later in this chapter.

An artificial equation of state $P = \delta\rho$ is the basis of the method of artificial compressibility [6]. This method differs from the projection method in that the continuity equation is not satisfied until a steady state is reached. Chorin [6] uses central difference in space and time to arrive at a scheme designed for steady state solutions. Methods for unsteady solutions using artificial compressibility have also been developed by later researchers [3].

Out of the three methods described above, the class of SIMPLE originally developed by Spalding is the most popular method to solve for incompressible Navier-Stokes equation. There have been a lot of attempts to improve SIMPLE, making a class of

incompressible flow algorithm on its own. Patankar developed a new algorithm named SIMPLER (SIMPLE Revised) [4]. Van Doormal and Raithby came up with another algorithm named SIMPLEC [7] in 1984, which worked without the under-relaxation α_p [4] for the pressure correction equation. Van Doormal and Raithby also came up with another algorithm of the same class named SIMPLEX [8] in the following year. All the above formulations are based on staggered grids. Patankar showed in [4] that if collocated grids are used, then Poisson formulations can lead to an odd-even decoupling of pressure, and hence collocated grid or non-staggered grid was not so popular before Thiart [9] proposed another SIMPLE type algorithm named SIMPLEN (SIMPLE Non-staggered) in 1990. Other researchers who worked on non-staggered grids and incompressible flow but not necessarily SIMPLE class of algorithms were Shih and Ren [10], Rhie and Chow [11], Yen and Liu [12], Majumdar [13]. Other SIMPLE class algorithms are SIMPLEM [14] by Acharya and Moukalled, PISO [15] by Issa, PRIME [16], SIMPLESSE [17] and SIMPLESSEC [18]. More recently, Ozoe and Tao [19] came up with another algorithm, MSIMPLER (Modified SIMPLER), in 2001. Also, Karki [20] extended SIMPLER algorithm to solve for flows of all speeds, and from that point on, researchers have extensively worked on SIMPLE family of algorithms to make them work for all speeds. A detailed description can be found in [21].

Pressure-based methods have always been extremely popular in the field of incompressible flow solvers. Researchers Mathur and Murthy [22], Kang and Kim [23] and many others worked on extending the idea towards unstructured grids. Hutchinson and Raithby [24], Gjesdal and Lossius [18] and others worked on multigrid solutions. Majumdar [13], Yu, Tao, Wei, Kawaguchi, Tagawa, and Ozoe [25] and others developed momentum interpolation methods.

For spatial discretization of the Navier-Stokes equations, different techniques can be used. However, Patankar [4] showed that the power law scheme ideally fits for all the Peclet numbers. In this work, power law scheme is used. Some of the other higher order

schemes include SOU [26], QUICK [27, 28] and FOUB [29].

1.2 Current Research

The basic objective of the present research was to study the unsteady flow pattern past elliptic cylinders for different Reynolds number in the incompressible regime. In his master's thesis, Lim [30] studied the steady flow past a half cylinder for flows ranging from incompressible to supersonic speeds. Two major developments were needed in the present work to study the unsteady behavior past a full cylinder. First, the algorithm had to be extended to solve for unsteady flow. Hence, the unsteady form of Navier-Stokes equations was used. For the temporal integration, two methods were chosen, Fully Implicit and Crank Nicolson [31, 32]. The discretized equations were solved using a segregated approach where the discretized equation for each variable is solved sequentially. The resulting algebraic equations were cast into tridiagonal systems over the entire computational domain and solved using a line-by-line, under-relaxation technique known as the TriDiagonal Matrix Algorithm (TDMA). The detailed derivation can be found in chapters 2 and 3.

Secondly, the algorithm had to be extended to work for a full cylinder. The reason for that was the fact that a half cylinder does not show any oscillatory pattern in the flow, which is known to be a characteristic of the flow past a circular cylinder from previous researchers. In the conclusion, this is described in detail. There are two ways to make the necessary changes. One is to implicitly incorporate the circular boundary condition in the solver and the other is to apply the conditions explicitly. The second method, for its inherent simplicity, was chosen. In chapter 4, the implementation of the boundary conditions is explained in detail.

It should be pointed out at this point that though the flow past a circular cylinder was sought after, a 2-d body intrinsic orthogonal curvilinear coordinate system was used.

The discretization of the computaional domain was based on simple algebraic techniques. The stretching transformation by Cebeci [33] was used to generate an adequately refined viscous grid near the body surface. The flow over the circular cylinder was used as a test bed for studying the unsteady behavior of the flow past elliptic cylinders. The Fully Implicit and Crank Nicolson results for circular cylinders is presented in chapter 5.1 and for elliptic cylinders is presented in chapter 5.2. Chapter 6 concludes the study with future recommendations.

CHAPTER 2 DISCRETIZATION METHODOLOGY

2.1 Navier-Stokes Equations

The conservation equations applied to a fluid passing through an infinitesimal, fixed control volume can be written in the divergence form as

Continuity Equation:

$$\frac{\partial \rho}{\partial t} + \nabla \bullet (\rho V) = 0 \tag{2.1}$$

Momentum Equation:

$$\frac{\partial}{\partial t}(\rho V) + \nabla \bullet (\rho V V) = \rho f + \nabla \bullet \tilde{\Pi}_{ij} \tag{2.2}$$

where ρf is the body force per unit volume and $\nabla \bullet \tilde{\Pi}_{ij}$ is the surface forces per unit volume due to external stresses on the fluid element. The stress tensor $\tilde{\Pi}_{ij}$ consists of both the normal and shearing viscous stresses.

For Newtonian flows, the stress at a point is linearly dependent on the rate of strain of the fluid. A general deformation law which relates the stress tensor to the pressure and velocity components is given by

$$\tilde{\Pi}_{ij} = -p\tilde{I} + \mu \left[\nabla V + (\nabla V)^T - \frac{2}{3} \nabla \bullet V \tilde{I} \right] \tag{2.3}$$

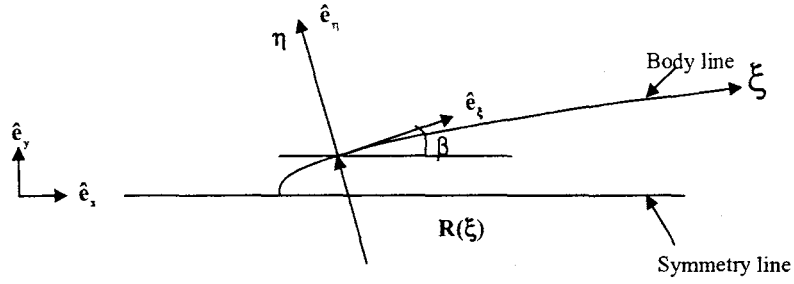

Figure 2.1 Two-dimensional body-intrinsic coordinate system and coordinate nomenclature

However, for incompressible case,

$$\tilde{\Pi}_{ij} = -p\tilde{I} + \mu\nabla V \tag{2.4}$$

For the present analysis, the flow is assumed to be unsteady, incompressible, laminar and two-dimensional. The inertial coordinate system is taken to be a two-dimensional, body-intrinsic, orthogonal curvilinear coordinate system shown in Fig. 2.1 wherein the ξ-direction is taken to be along the body while the η-direction is perpendicular to the body surface. With these assumptions, Eqns. 2.1 through 2.2 (upon substitution of Eqn 2.4) are expanded and rearranged (detailed derivation in [30]) to yield

Continuity Equation:

$$\frac{\partial \rho}{\partial t} + \frac{1}{h_1}\frac{\partial}{\partial \xi}(\rho v_\xi) + \frac{1}{h_1}\frac{\partial}{\partial \eta}(h_1 \rho v_\eta) = 0 \tag{2.5}$$

v_ξ momentum Equation:

$$\frac{\partial}{\partial t}(\rho v_\xi) + \frac{1}{h_1}\frac{\partial}{\partial \xi}\left(\rho v_\xi v_\xi - \frac{1}{h_1}\mu\frac{\partial v_\xi}{\partial \xi}\right) + \frac{1}{h_1}\frac{\partial}{\partial \eta}\left(h_1\rho v_\eta v_\xi - h_1\mu\frac{\partial v_\xi}{\partial \eta}\right) = -\frac{1}{h_1}(\rho v_\xi v_\eta)\frac{\partial h_1}{\partial \eta} - \frac{1}{h_1}\frac{\partial p}{\partial \xi} + \frac{\mu}{h_1}\left[\frac{\partial}{\partial \xi}\left(\frac{v_\eta}{h_1}\frac{\partial h_1}{\partial \eta}\right) + \left(\frac{1}{h_1}\frac{\partial v_\eta}{\partial \xi} - \frac{v_\xi}{h_1}\frac{\partial h_1}{\partial \eta}\right)\frac{\partial h_1}{\partial \eta}\right] \tag{2.6}$$

v_η momentum Equation:

$$\frac{\partial}{\partial t}(\rho v_\eta) + \frac{1}{h_1}\frac{\partial}{\partial \xi}\left(\rho v_\xi v_\eta - \frac{1}{h_1}\mu\frac{\partial v_\eta}{\partial \xi}\right) + \frac{1}{h_1}\frac{\partial}{\partial \eta}\left(h_1\rho v_\eta v_\eta - h_1\mu\frac{\partial v_\eta}{\partial \eta}\right) = \frac{1}{h_1}(\rho v_\xi v_\xi)\frac{\partial h_1}{\partial \eta} - \frac{\partial p}{\partial \eta} + \frac{\mu}{h_1}\left[\frac{\partial}{\partial \xi}\left(\frac{v_\xi}{h_1}\frac{\partial h_1}{\partial \eta}\right) - \left(\frac{1}{h_1}\frac{\partial v_\xi}{\partial \xi} - \frac{v_\eta}{h_1}\frac{\partial h_1}{\partial \eta}\right)\frac{\partial h_1}{\partial \eta}\right] \tag{2.7}$$

It should be pointed out that the above expressions for momentum equations were derived assuming constant viscosity, which may be a poor assumption for a non-isothermal flow of a liquid whose viscosity is highly dependent on temperature. However, as in the case here, the viscosity of gases is moderately dependent on temperature and therefore the momentum equations derived are a good approximation for incompressible flow of gas.

2.2 Time Integration

In the present work, Crank-Nicolson and Fully Implicit methods were used for time integration. Both of them can be conveniently stated as

$$\int_{t_o}^{t} \phi dt = \left[\alpha\phi + (1-\alpha)\,\phi_o\right]\Delta t \tag{2.8}$$

where the ϕ is the quantity to be integrated and the value of α may be different depending on the scheme of choice. All time integrations in the following sections are done using the

above stencil. The value of $\alpha = 0.5$ corresponds to the Crank-Nicolson time integration scheme and $\alpha = 1$ corresponds to the Fully Implicit scheme.

2.3 Control-Volume Approach

The control volume approach for discretizing the governing equations maintains the conservative property in the final discretized form by dividing the computational domain into a set of non-overlapping control volumes. The conservation laws are then expressed in integral form in each of these control volumes. If the finite-volume representation approximates the conservation law closely in each of the control volumes, then it is reasonable to expect that the conservation law will be over the entire domain. Another feature of this approach is that the conservative nature exists not only in a limiting case where the control volumes are small, but also for any reasonable size of control volumes. Thus, even the solution to a coarser control volume, especially in the vicinity of the outer boundary, would exhibit the exact integral balance.

2.4 Domain Discretization

In the present work, the computational domain is divided into quadrilateral volumes where the vertices of each volume are defined by the intersections of the coordinate lines in the body intrinsic coordinate system. This will ensure orthogonality over the entire computational domain. A typical distretized domain or grid is shown in Fig. 2.2. The solid lines represent the domain boundaries and the dashed lines represent the faces of the control volumes. The grid points are placed at the geometrical centers of the quadrilaterals. The placement of the control volume faces and the grid points is based on practice B of Patankar found in [4]. In this practice, the faces of the control volumes are generated first and the position of the grid points follows as a consequence. This approach eliminates the need for half control volumes around the boundary points.

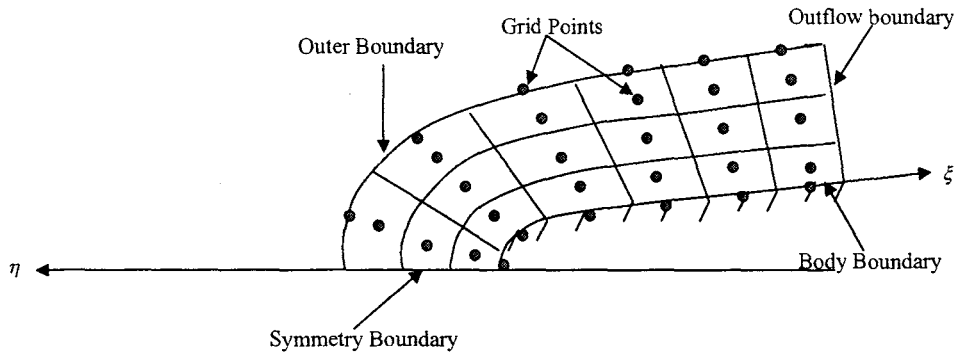

Figure 2.2 Typical computational grid arrangement for the entire domain

The grids are generated such that the grid width is uniform in the ξ direction. The η-lines are generated using a constant ratio scheme such as that used by Cebeci [33]. This constant ratio stretching results in a geometric progression in the size of the spacing such that

$$\Delta\eta_j = \epsilon^{j-1}\Delta\eta_1 \tag{2.9}$$

$$\eta_j = \Delta\eta_1 \frac{\epsilon^{j-1} - 1}{\epsilon - 1} \qquad j = 1, 2, 3, ...NJ \tag{2.10}$$

The attractive feature of this constant ratio scheme is that it allows the explicit specification of the first control volume width $\Delta\eta_1$ and the desired stretching can be controlled through ϵ.

The above method of clustering is essential to properly resolve the boundary layer near the body where the flow gradients are the largest.

2.5 Staggered Grid Arrangement

The discretization of the momentum equations would require the integration of the pressure gradient, for example $-\partial p/\partial \xi$ in the ξ-direction. The resulting contribution to the discretized equation is the pressure drop $p_{i+\frac{1}{2}} - p_{i-\frac{1}{2}}$ where $p_{i+\frac{1}{2}}$ is the pressure on the right face and $p_{i-\frac{1}{2}}$ is the pressure on the left face of a control volume. To express the face pressures in terms of the grid point pressures, a piecewise-linear profile for pressure may be assumed. However, such an interpolation can lead to a so-called checkerboard pattern in the face pressures in the converged solution. A similar kind of difficulty also arises in the discretization of the continuity equation. This leads to the conservation of mass over alternate grid points and not adjacent ones. A detailed discussion of these shortcomings can be found in [34].

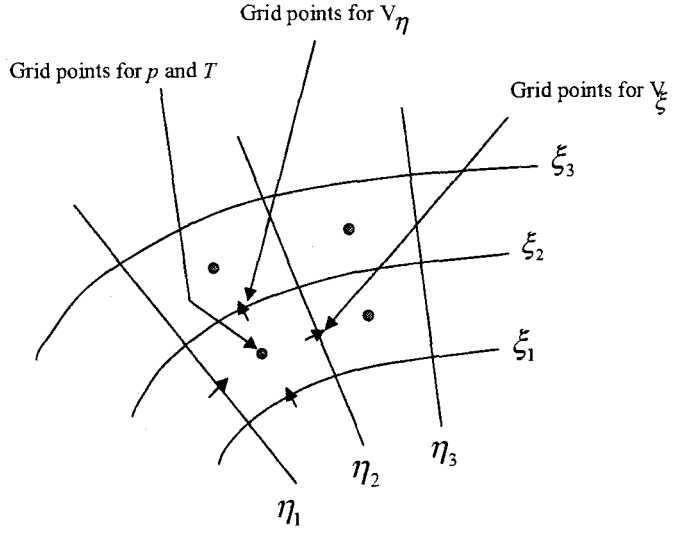

Figure 2.3 Location of velocities, pressure and temperature in the staggered grid arrangement

The above difficulties can be avoided by using a staggered grid arrangement where all the flow variables are not defined at the main grid point and a different grid is used for

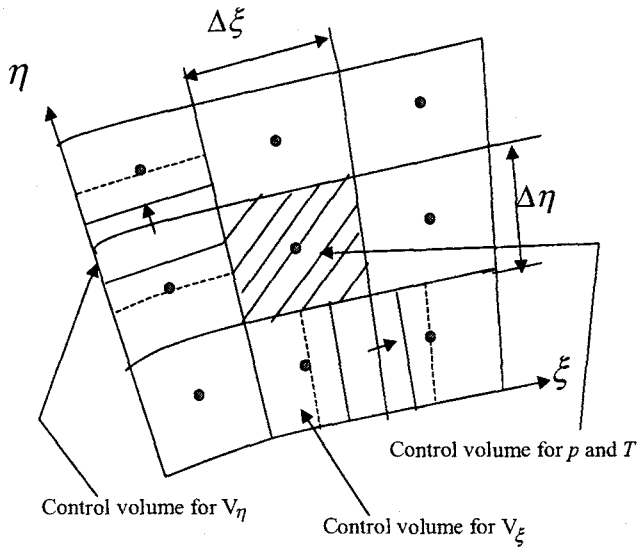

Figure 2.4 Control volumes for velocities, pressure and temperature in the staggered grid arrangement

each variable. Such a staggered grid arrangement was first used by Harlow and Welch [35] in the MAC method and now forms the basis of the SIVA procedure by Caretto, Curr and Spalding [36] and the SIMPLER procedure [4, 5] used in the present work.

In the staggered grid shown in Fig. 2.3, the v_ξ velocities are staggered in the ξ-direction and the v_η velocities are staggered in the η-direction. Pressure and temperature is stored at the main grid points. However, in this study, temperature is not important and hence will not be mentioned hereafter. Fig. 2.4 shows collectively the resulting control volumes for v_ξ and v_η velocities and pressure p. Figs. 2.5 through 2.7 show the convention for the indexing of the indices used to identify the various staggered variables. The discretization of the governing equations is discussed next.

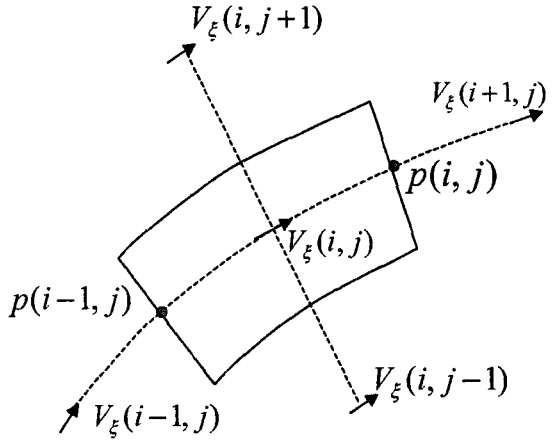

Figure 2.5 Control volume and indexing convention for v_ξ-velocity

2.6 Discretization of Continuity Equation

The surface and time integration of the continuity equation given by Eqn. 2.5 over a control volume shown in Fig. 2.7 can be done in a term by term following manner. For convenience, the equation is reproduced here :

$$\frac{\partial \rho}{\partial t} + \frac{1}{h_1}\frac{\partial}{\partial \xi}(\rho v_\xi) + \frac{1}{h_1}\frac{\partial}{\partial \eta}(h_1 \rho v_\eta) = 0 \tag{2.11}$$

The elemental area in the body-intrinsic coordinate system is given by $h_1 \Delta\xi \Delta\eta$. Hence, upon integration of the first term,

$$\int_{t_0}^{t} \int_{i-\frac{1}{2}}^{i+\frac{1}{2}} \int_{j-\frac{1}{2}}^{j+\frac{1}{2}} \frac{\partial \rho}{\partial t} dt d\xi d\eta = \int_{t_0}^{t} \left(\frac{\partial \rho}{\partial t} dt \right) h_1 \Delta\xi \Delta\eta = \left[\rho - \rho^0 \right] h_1 \Delta\xi \Delta\eta \tag{2.12}$$

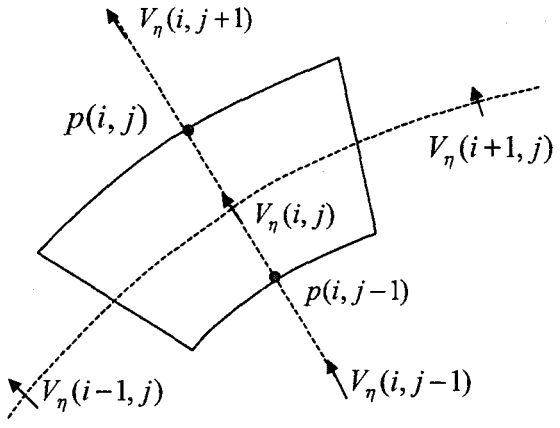

Figure 2.6 Control volume and indexing convention for v_η-velocity

Upon integration of the second term,

$$\begin{aligned}\int_{t_0}^{t}\int_{i-\frac{1}{2}}^{i+\frac{1}{2}}\int_{j-\frac{1}{2}}^{j+\frac{1}{2}}\left(\frac{\partial(\rho v_\xi)}{\partial\xi}d\xi\right)d\eta dt &= \int_{t_0}^{t}\Delta\eta\left[\int\frac{\partial(\rho v_\xi)}{\partial\xi}\right]dt \\ &= \int_{t_0}^{t}\left[(\rho v_\xi)_{i+\frac{1}{2},j}-(\rho v_\xi)_{i-\frac{1}{2},j}\right]\Delta\eta dt\end{aligned} \tag{2.13}$$

To simplify the above equation, the following terms may be introduced :

$$(\rho v_\xi)_{i+\frac{1}{2},j} = F_{i+\frac{1}{2},j} \tag{2.14}$$

$$(\rho v_\xi)_{i-\frac{1}{2},j} = F_{i-\frac{1}{2},j} \tag{2.15}$$

$$(h_1\rho v_\eta)_{i,j+\frac{1}{2}} = F_{i,j+\frac{1}{2}} \tag{2.16}$$

$$(h_1\rho v_\eta)_{i,j-\frac{1}{2}} = F_{i,j-\frac{1}{2}} \tag{2.17}$$

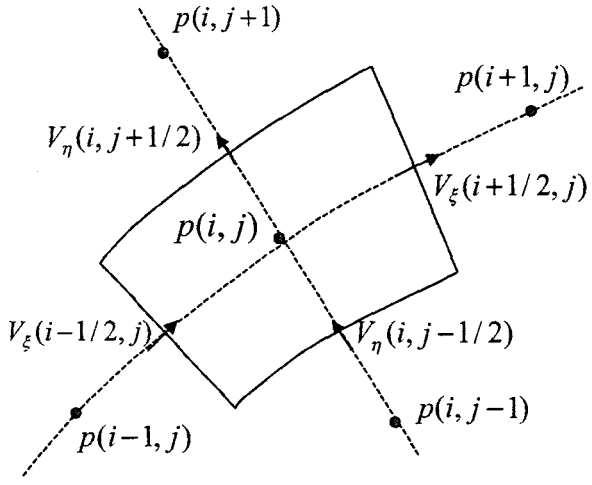

Figure 2.7 Control volume and indexing convention for pressure

Therefore, using Eqns. 2.14 through 2.17 and the time stencil (Eqn. 2.8), Eqn. 2.13 becomes

$$\begin{aligned}\int_{t_0}^{t}\left(F_{i+\frac{1}{2},j}-F_{i-\frac{1}{2},j}\right) &= \left[\alpha F_{i+\frac{1}{2},j}+(1-\alpha)F^0_{i+\frac{1}{2},j}-\alpha F_{i-\frac{1}{2},j}-(1-\alpha)F^0_{i-\frac{1}{2},j}\right]\Delta t \\ &= \left[\alpha(F_{i+\frac{1}{2},j}-F_{i-\frac{1}{2},j})+(1-\alpha)(F^0_{i+\frac{1}{2},j}-F^0_{i-\frac{1}{2},j})\right]dt\end{aligned} \tag{2.18}$$

Similarly, integration of the third term of the continuity equation yields

$$\begin{aligned}&\int_{t_0}^{t}\int_{i-\frac{1}{2}}^{i+\frac{1}{2}}\int_{j-\frac{1}{2}}^{j+\frac{1}{2}}\left(\frac{\partial(h_1\rho v_\eta)}{\partial\eta}d\eta\right)d\xi dt = \\ &\qquad\left[\alpha(F_{i,j+\frac{1}{2}}-F_{i,j-\frac{1}{2}})+(1-\alpha)(F^0_{i,j+\frac{1}{2}}-F^0_{i,j-\frac{1}{2}})\right]dt\end{aligned} \tag{2.19}$$

Upon collecting all the terms from Eqns. 2.12, 2.18 and 2.19 and rearranging, the

continuity equation becomes

$$\begin{aligned}(\rho-\rho^0)\frac{h_1\Delta\xi\Delta\eta}{\Delta t}+\alpha(F_{i+\frac{1}{2},j}-F_{i-\frac{1}{2},j}+F_{i,j+\frac{1}{2}}-F_{i,j-\frac{1}{2}})\\ +(1-\alpha)(F^0_{i+\frac{1}{2},j}-F^0_{i-\frac{1}{2},j}+F^0_{i,j+\frac{1}{2}}-F^0_{i,j-\frac{1}{2}})=0\end{aligned} \tag{2.20}$$

It might be restated here that the value of α defines the type of the scheme. For Fully Implicit scheme, $\alpha = 1$ and for Crank Nicolson, $\alpha = \frac{1}{2}$.

Also, it should be pointed out that in arriving at the above expression, the velocity and other properties at the center of the face are assumed to prevail over the entire face.

2.7 Discretization of the Momentum Equations

2.7.1 v_ξ Momentum Equation

For convenience, the v_ξ-momentum equation is reproduced here :

$$\begin{aligned}\frac{\partial}{\partial t}(\rho v_\xi)+\frac{1}{h_1}\frac{\partial}{\partial\xi}\left(\rho v_\xi v_\xi-\frac{1}{h_1}\mu\frac{\partial v_\xi}{\partial\xi}\right)+\frac{1}{h_1}\frac{\partial}{\partial\eta}\left(h_1\rho v_\eta v_\xi-h_1\mu\frac{\partial v_\xi}{\partial\eta}\right)=-\frac{1}{h_1}(\rho v_\xi v_\eta)\frac{\partial h_1}{\partial\eta}-\\ \frac{1}{h_1}\frac{\partial p}{\partial\xi}+\frac{\mu}{h_1}\left[\frac{\partial}{\partial\xi}\left(\frac{v_\eta}{h_1}\frac{\partial h_1}{\partial\eta}\right)+\left(\frac{1}{h_1}\frac{\partial v_\eta}{\partial\xi}-\frac{v_\xi}{h_1}\frac{\partial h_1}{\partial\eta}\right)\frac{\partial h_1}{\partial\eta}\right]\end{aligned} \tag{2.21}$$

The equation can be rewritten as

$$\frac{\partial(\rho v_\xi)}{\partial t}+\frac{1}{h_1}\frac{\partial J_{v_\xi\xi}}{\partial\xi}+\frac{1}{h_1}\frac{\partial J_{v_\xi\eta}}{\partial\eta}=-\frac{1}{h_1}\frac{\partial p}{\partial\xi}+S_{v_\xi} \tag{2.22}$$

where

$$J_{v_\xi\xi}=\left(\rho v_\xi v_\xi-\frac{1}{h_1}\mu\frac{\partial v_\xi}{\partial\xi}\right) \tag{2.23}$$

$$J_{v_\xi\eta}=\left(h_1\rho v_\xi v_\eta-h_1\mu\frac{\partial v_\xi}{\partial\eta}\right) \tag{2.24}$$

$$S_{v_\xi} = -\frac{1}{h_1}(\rho v_\xi v_\eta)\frac{\partial h_1}{\partial \eta} + \frac{\mu}{h_1}\left[\frac{\partial}{\partial \xi}\left(\frac{v_\eta}{h_1}\frac{\partial h_1}{\partial \eta}\right) + \left(\frac{1}{h_1}\frac{\partial v_\eta}{\partial \xi} - \frac{v_\xi}{h_1}\frac{\partial h_1}{\partial \eta}\right)\frac{\partial h_1}{\partial \eta}\right] \tag{2.25}$$

Upon integration of the above equation term by term, as done in the continuity equation, the following can be obtained :

$$\begin{aligned}\left[(\rho v_\xi) - (\rho v_\xi)^0\right]\frac{h_1 \Delta\xi\Delta\eta}{\Delta t} + \alpha\left(J_{v_{\xi_{i+\frac{1}{2},j}}} - J_{v_{\xi_{i-\frac{1}{2},j}}} + \right. \\ \left. J_{v_{\xi_{i,j+\frac{1}{2}}}} - J_{v_{\xi_{i,j-\frac{1}{2}}}}\right) + (1-\alpha)\left(J^0_{v_{\xi_{i+\frac{1}{2},j}}} - J^0_{v_{\xi_{i-\frac{1}{2},j}}} + \right. \\ \left. J^0_{v_{\xi_{i,j+\frac{1}{2}}}} - J^0_{v_{\xi_{i,j-\frac{1}{2}}}}\right) = \left(\alpha S_{v_\xi} + (1-\alpha)S^0_{v_\xi}\right)_{i,j} h_1 \Delta\xi\Delta\eta \\ + (p_{i-1,j} - p_{i,j})\Delta\eta\end{aligned} \tag{2.26}$$

2.7.2 v_η-Momentum Equation

For convenience, the v_η-momentum equation is reproduced here

$$\begin{aligned}\frac{\partial}{\partial t}(\rho v_\eta) + \frac{1}{h_1}\frac{\partial}{\partial \xi}\left(\rho v_\xi v_\eta - \frac{1}{h_1}\mu\frac{\partial v_\eta}{\partial \xi}\right) + \frac{1}{h_1}\frac{\partial}{\partial \eta}\left(h_1\rho v_\eta v_\eta - h_1\mu\frac{\partial v_\eta}{\partial \eta}\right) = \frac{1}{h_1}(\rho v_\xi v_\xi)\frac{\partial h_1}{\partial \eta} - \\ \frac{\partial p}{\partial \eta} + \frac{\mu}{h_1}\left[\frac{\partial}{\partial \xi}\left(\frac{v_\xi}{h_1}\frac{\partial h_1}{\partial \eta}\right) - \left(\frac{1}{h_1}\frac{\partial v_\xi}{\partial \xi} - \frac{v_\eta}{h_1}\frac{\partial h_1}{\partial \eta}\right)\frac{\partial h_1}{\partial \eta}\right]\end{aligned} \tag{2.27}$$

The equation can be rewritten as

$$\frac{\partial(\rho v_\eta)}{\partial t} + \frac{1}{h_1}\frac{\partial J_{v_\eta\xi}}{\partial \xi} + \frac{1}{h_1}\frac{\partial J_{v_\eta\eta}}{\partial \eta} = -\frac{\partial p}{\partial \eta} + S_{v_\eta} \tag{2.28}$$

where

$$J_{v_\eta\xi} = \left(\rho v_\eta v_\xi - \frac{1}{h_1}\mu\frac{\partial v_\xi}{\partial \xi}\right) \tag{2.29}$$

$$J_{v_\xi\eta} = \left(h_1\rho v_\eta v_\eta - h_1\mu\frac{\partial v_\eta}{\partial \eta}\right) \tag{2.30}$$

$$S_{v_\eta} = -\frac{1}{h_1}(\rho v_\xi v_\xi)\frac{\partial h_1}{\partial \eta} + \frac{\mu}{h_1}\left[\frac{\partial}{\partial \xi}\left(\frac{v_\xi}{h_1}\frac{\partial h_1}{\partial \eta}\right) - \left(\frac{1}{h_1}\frac{\partial v_\xi}{\partial \xi} - \frac{v_\eta}{h_1}\frac{\partial h_1}{\partial \eta}\right)\frac{\partial h_1}{\partial \eta}\right] \tag{2.31}$$

In a similar fashion, integration of this equation gives

$$\begin{aligned}\left[(\rho v_\eta) - (\rho v_\eta)^0\right]\frac{h_1 \Delta\xi\Delta\eta}{\Delta t} + \alpha\Big(J_{v_{\eta_{i+\frac{1}{2},j}}} - J_{v_{\eta_{i-\frac{1}{2},j}}} + \\ J_{v_{\eta_{i,j+\frac{1}{2}}}} - J_{v_{\eta_{i,j-\frac{1}{2}}}}\Big) + (1-\alpha)\Big(J^0_{v_{\eta_{i+\frac{1}{2},j}}} - J^0_{v_{\eta_{i-\frac{1}{2},j}}} + \\ J^0_{v_{\eta_{i,j+\frac{1}{2}}}} - J^0_{v_{\eta_{i,j-\frac{1}{2}}}}\Big) = \Big(\alpha S_{v_\eta} + (1-\alpha)S^0_{v_\eta}\Big)_{i,j} h_1 \Delta\xi\Delta\eta \\ +(p_{i,j-1} - p_{i,j})h_1\Delta\xi\end{aligned} \tag{2.32}$$

2.7.3 Defining Coefficients

Assuming incompressible flow (constant density, ρ), the first term of Eqn. 2.20 goes to zero. Since the choice of α is arbitrary, Eqn. 2.20, which is the continuity equation, can be written as

$$(F_{i+\frac{1}{2},j} - F_{i-\frac{1}{2},j} + F_{i,j+\frac{1}{2}} - F_{i,j-\frac{1}{2}}) = 0 \tag{2.33}$$

$$(F^0_{i+\frac{1}{2},j} - F^0_{i-\frac{1}{2},j} + F^0_{i,j+\frac{1}{2}} - F^0_{i,j-\frac{1}{2}}) = 0 \tag{2.34}$$

Multipying Eqn. 2.33 by $\alpha v_{\xi_{ij}}$ and Eqn. 2.34 by $(1-\alpha)v^0_{\xi_{ij}}$ and subtracting both from Eqn. 2.26 yields

$$\begin{aligned}
&\left(v_\xi - {v_\xi}^0\right)_{i,j}\frac{h_1\rho\Delta\xi\Delta\eta}{\Delta t} + \alpha\left[\left(J_{v_{\xi_{i+\frac{1}{2},j}}} - F_{i+\frac{1}{2},j}v_{\xi_{i,j}}\right)\right. \\
&\quad - \left(J_{v_{\xi_{i-\frac{1}{2},j}}} - F_{i-\frac{1}{2},j}v_{\xi_{i,j}}\right) + \left(J_{v_{\xi_{i,j+\frac{1}{2}}}} - F_{i,j+\frac{1}{2}}v_{\xi_{ij}}\right) \\
&\left. - \left(J_{v_{\xi_{i,j-\frac{1}{2}}}} - F_{i,j-\frac{1}{2}}v_{\xi_{i,j}}\right)\right] + (1-\alpha)\left[\left(J^0_{v_{\xi_{i+\frac{1}{2},j}}} - F^0_{i+\frac{1}{2},j}v^0_{\xi_{i,j}}\right)\right. \\
&\quad - \left(J^0_{v_{\xi_{i-\frac{1}{2},j}}} - F^0_{i-\frac{1}{2},j}v^0_{\xi_{i,j}}\right) + \left(J^0_{v_{\xi_{i,j+\frac{1}{2}}}} - F^0_{i,j+\frac{1}{2}}v^0_{\xi_{i,j}}\right) \\
&\left. - \left(J^0_{v_{\xi_{i,j-\frac{1}{2}}}} - F^0_{i,j-\frac{1}{2}}v^0_{\xi_{i,j}}\right)\right] \\
&= \left(\alpha S_{v_\xi} + (1-\alpha)S^0_{v_\xi}\right)_{i,j} h_1\Delta\xi\Delta\eta + (p_{i-1,j} - p_{i,j})\Delta\eta
\end{aligned} \tag{2.35}$$

Using the notation in Patankar [4], the following simplifications are used to help the algebraic manipulation of the conservative equations:

$$J_{v_{\xi_{i+\frac{1}{2},j}}} - F_{i+\frac{1}{2},j}v_{\xi_{i,j}} = \bar{a}_{v_{\xi_{i+1,j}}}\left(v_{\xi_{i,j}} - v_{\xi_{i+1,j}}\right) \tag{2.36}$$

$$J_{v_{\xi_{i-\frac{1}{2},j}}} - F_{i-\frac{1}{2},j}v_{\xi_{i,j}} = \bar{a}_{v_{\xi_{i-1,j}}}\left(v_{\xi_{i,j}} - v_{\xi_{i-1,j}}\right) \tag{2.37}$$

$$J_{v_{\xi_{i,j+\frac{1}{2}}}} - F_{i,j+\frac{1}{2}}v_{\xi_{i,j}} = \bar{a}_{v_{\xi_{i,j+1}}}\left(v_{\xi_{i,j}} - v_{\xi_{i,j+1}}\right) \tag{2.38}$$

$$J_{v_{\xi_{i,j-\frac{1}{2}}}} - F_{i,j-\frac{1}{2}}v_{\xi_{i,j}} = \bar{a}_{v_{\xi_{i,j-1}}}\left(v_{\xi_{i,j}} - v_{\xi_{i,j-1}}\right) \tag{2.39}$$

$$J^0_{v_{\xi_{i+\frac{1}{2},j}}} - F^0_{i+\frac{1}{2},j}v^0_{\xi_{i,j}} = \bar{a}^0_{v_{\xi_{i+1,j}}}\left(v^0_{\xi_{i,j}} - v^0_{\xi_{i+1,j}}\right) \tag{2.40}$$

$$J^0_{v_{\xi_{i-\frac{1}{2},j}}} - F^0_{i-\frac{1}{2},j} v^0_{\xi_{i,j}} = \bar{a}^0_{v_{\xi_{i-1,j}}} \left(v^0_{\xi_{i,j}} - v^0_{\xi_{i-1,j}} \right) \tag{2.41}$$

$$J^0_{v_{\xi_{i,j+\frac{1}{2}}}} - F^0_{i,j+\frac{1}{2}} v^0_{\xi_{i,j}} = \bar{a}^0_{v_{\xi_{i,j+1}}} \left(v^0_{\xi_{i,j}} - v^0_{\xi_{i,j+1}} \right) \tag{2.42}$$

$$J^0_{v_{\xi_{i,j-\frac{1}{2}}}} - F^0_{i,j-\frac{1}{2}} v^0_{\xi_{i,,j}} = \bar{a}^0_{v_{\xi_{i,j-1}}} \left(v^0_{\xi_{i,j}} - v^0_{\xi_{i,j-1}} \right) \tag{2.43}$$

where the coefficient $\bar{a}$'s are defined as

$$\bar{a}_{i+1,j} = D_{i+\frac{1}{2},j} A \left(\mid P_{i+\frac{1}{2},j} \mid \right) + \parallel -F_{i+\frac{1}{2},j}, 0 \parallel \tag{2.44}$$

$$\bar{a}_{i-1,j} = D_{i-\frac{1}{2},j} A \left(\mid P_{i-\frac{1}{2},j} \mid \right) + \parallel F_{i-\frac{1}{2},j}, 0 \parallel \tag{2.45}$$

$$\bar{a}_{i,j+1} = D_{i,j+\frac{1}{2}} A \left(\mid P_{i,j+\frac{1}{2}} \mid \right) + \parallel -F_{i,j+\frac{1}{2}}, 0 \parallel \tag{2.46}$$

$$\bar{a}_{i,j-1} = D_{i,j-\frac{1}{2}} A \left(\mid P_{i,j-\frac{1}{2}} \mid \right) + \parallel F_{i,j-\frac{1}{2}}, 0 \parallel \tag{2.47}$$

and D's are defined as

$$D_{i+\frac{1}{2},j} = \frac{\mu_{i+\frac{1}{2},j} \Delta\eta}{(h_1)_{i+\frac{1}{2},j} \delta\xi_{i+\frac{1}{2},j}} \tag{2.48}$$

$$D_{i-\frac{1}{2},j} = \frac{\mu_{i-\frac{1}{2},j} \Delta\eta}{(h_1)_{i-\frac{1}{2},j} \delta\xi_{i-\frac{1}{2},j}} \tag{2.49}$$

$$D_{i,j+\frac{1}{2}} = \frac{\mu_{i,j+\frac{1}{2}} (h_1)_{i,j+\frac{1}{2}} \Delta\xi}{\delta\eta_{i,j+\frac{1}{2}}} \tag{2.50}$$

$$D_{i,j-\frac{1}{2}} = \frac{\mu_{i,j-\frac{1}{2}}(h_1)_{i,j-\frac{1}{2}}\Delta\xi}{\delta\eta_{i,j-\frac{1}{2}}} \tag{2.51}$$

$$P_{i+\frac{1}{2},j} = \frac{F_{i+\frac{1}{2},j}}{D_{i+\frac{1}{2},j}} \tag{2.52}$$

$$P_{i-\frac{1}{2},j} = \frac{F_{i-\frac{1}{2},j}}{D_{i-\frac{1}{2},j}} \tag{2.53}$$

$$P_{i,j+\frac{1}{2}} = \frac{F_{i,j+\frac{1}{2}}}{D_{i,j+\frac{1}{2}}} \tag{2.54}$$

$$P_{i,j-\frac{1}{2}} = \frac{F_{i,j-\frac{1}{2}}}{D_{i,j-\frac{1}{2}}} \tag{2.55}$$

and

$$A(\mid P \mid) = \parallel 0, (1 - 0.1 \mid P \mid)^5 \parallel \tag{2.56}$$

Eqn. 2.56 is a statement of Power-law scheme. Upon substitution of Eqns. 2.36 through 2.43, the v_ξ monentum equation becomes

$$\begin{aligned}
&v_{\xi_{i,j}}\frac{h_1\rho\Delta\xi\Delta\eta}{\Delta t} + \alpha\left(\bar{a}_{i+1,j} + \bar{a}_{i-1,j} + \bar{a}_{i,j+1}\right.\\
&\left.+\bar{a}_{i,j-1}\right)v_{\xi_{i,j}} = \alpha\left(\bar{a}_{i+1,j}v_{\xi_{i+1,j}} + \bar{a}_{i-1,j}v_{\xi_{i-1,j}}\right.\\
&\left.+\bar{a}_{i,j+1}v_{\xi_{i,j+1}} + \bar{a}_{i,j-1}v_{\xi_{i,j-1}}\right) + v^0_{\xi_{i,j}}\frac{h_1\rho\Delta\xi\Delta\eta}{\Delta t}\\
&-(1-\alpha)\left(\bar{a}^0_{i+1,j} + \bar{a}^0_{i-1,j} + \bar{a}^0_{i,j+1} + \bar{a}^0_{i,j-1}\right)v^0_{\xi_{i,j}}\\
&+(1-\alpha)\left(\bar{a}^0_{i+1,j}v^0_{\xi_{i+1,j}} + \bar{a}^0_{i-1,j}v^0_{\xi_{i-1,j}} + \bar{a}^0_{i,j+1}v^0_{\xi_{i,j+1}}\right.\\
&\left.+\bar{a}^0_{i,j-1}v^0_{\xi_{i,j-1}}\right) + \left(\alpha S_{v_\xi} + (1-\alpha)S^0_{v_\xi}\right)_{i,j}h_1\Delta\xi\Delta\eta\\
&+(p_{i-1,j} - p_{i,j})\Delta\eta
\end{aligned} \tag{2.57}$$

Or, in a more compact form,

$$\begin{aligned} a_{i,j}v_{\xi_{i,j}} = \; & a_{i+1,j}v_{\xi_{i+1,j}} + a_{i-1,j}v_{\xi_{i-1,j}} + a_{i,j+1}v_{\xi_{i,j+1}} \\ & + a_{i,j-1}v_{\xi_{i,j-1}} + b_{v_\xi} + (p_{i-1,j} - p_{i,j})\Delta\eta \end{aligned} \tag{2.58}$$

where

$$a_{i,j} = \frac{h_1\rho\Delta\xi\Delta\eta}{\Delta t} + \alpha\left(\bar{a}_{i+1,j} + \bar{a}_{i-1,j}\bar{a}_{i,j+1} + \bar{a}_{i,j-1}\right) \tag{2.59}$$

$$a_{i+1,j} = \alpha\bar{a}_{i+1,j} \tag{2.60}$$

$$a_{i-1,j} = \alpha\bar{a}_{i-1,j} \tag{2.61}$$

$$a_{i,j+1} = \alpha\bar{a}_{i,j+1} \tag{2.62}$$

$$a_{i,j-1} = \alpha\bar{a}_{i,j-1} \tag{2.63}$$

and

$$\begin{aligned} b_{v_\xi} = \; & (1-\alpha)\left[\bar{a}^0_{i+1,j}v^0_{\xi_{i+1,j}} + \bar{a}^0_{i-1,j}v^0_{\xi_{i-1,j}} + \bar{a}^0_{i,j+1}v^0_{\xi_{i,j+1}}\right. \\ & + \bar{a}^0_{i,j-1}v^0_{\xi_{i,j-1}} - \left(\bar{a}^0_{i+1,j} + \bar{a}^0_{i-1,j} + \bar{a}^0_{i,j-1}\right. \\ & \left.\left. + \bar{a}^0_{i,j-1}\right)v^0_{\xi_{i,j}}\right] + v^0_{\xi_{i,j}}\frac{h_1\rho\Delta\xi\Delta\eta}{\Delta t} + \\ & \left(\alpha S_{v_\xi} + (1-\alpha)S^0_{v_\xi}\right)_{i,j} h_1\Delta\xi\Delta\eta \end{aligned} \tag{2.64}$$

A similar expression can be obtained proceeding in the same manner for v_η-momentum equation. It will be of the form

$$\begin{aligned} a_{i,j}v_{\eta_{i,j}} = \quad & a_{i+1,j}v_{\eta_{i+1,j}} + a_{i-1,j}v_{\eta_{i-1,j}} + a_{i,j+1}v_{\eta_{i,j+1}} \\ & + a_{i,j-1}v_{\eta_{i,j-1}} + b_{v_\eta} + (p_{i,j-1} - p_{i,j})h_1\Delta\xi \end{aligned} \tag{2.65}$$

The coefficients are defined similar to those for the v_ξ- momentum equation.

At this point, the governing equations have been discretized. The original differential equations are now written in algebraic equivalences. The next step is to solve this set of algebraic equations. The procedure used to solve these algebraic equations is presented in the next chapter.

CHAPTER 3 SOLUTION PROCEDURE

The solution procedure used in the present work is outlined here. The procedure is based on the SIMPLER algorithm developed by Patankar [4] in conjunction with the time integration method such as Crank Nicolson and Fully Implicit.

In the SIMPLER algorithm, an equation for pressure is derived by manipulating the discretized continuity and momentum equation. For incompressible flows, the pressure equation takes the form of Poisson equation. In addition, a pressure correction equation is solved to correct the velocities such that the continuity equation is satisfied.

The developments of these two equations are presented next.

3.1 Pressure Equation

Consider the momentum equation for $v_{\xi_{i+\frac{1}{2},j}}$ given by

$$a_{i+\frac{1}{2},j} v_{\xi_{i+\frac{1}{2},j}} = \Sigma a_{nb} v_{\xi_{nb}} + \frac{\Delta A}{\Delta \xi} (p_{i,j} - p_{i+1,j}) + b_{v\xi} \tag{3.1}$$

where $b_{v\xi}$ includes all the source terms except the pressure gradient.

The equation can be rewritten as

$$v_{\xi_{i+\frac{1}{2},j}} = \hat{v}_{\xi_{i+\frac{1}{2},j}} + d_{i+\frac{1}{2},j} (p_{i,j} - p_{i+1,j}) \tag{3.2}$$

where $\hat{v}_{\xi_{i+\frac{1}{2},j}}$ is called the pseudovelocity and is defined by

$$\hat{v}_{\xi_{i+\frac{1}{2},j}} = \frac{\Sigma a_{nb} v_{\xi_{nb}} + b}{a_{i+\frac{1}{2},j}} \tag{3.3}$$

Similarly, the momentum equation for $v_{\eta_{i,j+\frac{1}{2}}}$ is given by

$$v_{\eta_{i,j+\frac{1}{2}}} = \hat{v}_{\eta_{i,j+\frac{1}{2}}} + d_{i,j+\frac{1}{2}} \left(p_{i,j} - p_{i,j+1}\right) \tag{3.4}$$

The discretized continuity equation obtained in Chapter 2 is reproduced here :

$$\begin{aligned} \left(\frac{\partial \rho_{ij}}{\partial t}\right) + (\rho v_\xi)_{i+\frac{1}{2},j} \Delta\eta - (\rho v_\xi)_{i-\frac{1}{2},j} \Delta\eta + \\ (h_1 \rho v_\eta)_{i,j+\frac{1}{2}} \Delta\xi - (h_1 \rho v_\eta)_{i,j-\frac{1}{2}} \Delta\xi = 0 \end{aligned} \tag{3.5}$$

Substituting the momentum equations, i.e., Eqns. 3.3 and 3.4, in the continuity equation (Eqn. 3.5), the pressure equation is caste in the following form :

$$\begin{aligned} a_{i,j} p''_{i,j} = \; & a_{i+1,j} p''_{i+1,j} + a_{i-1,j} p''_{i-1,j} + a_{i,j+1} p''_{i,j+1} + \\ & a_{i,j-1} p''_{i,j-1} - b_{i,j} \end{aligned} \tag{3.6}$$

where

$$a_{i+1,j} = \rho_{i+\frac{1}{2},j} d_{i+\frac{1}{2},j} \Delta\eta \tag{3.7}$$

$$a_{i-1,j} = \rho_{i-\frac{1}{2},j} d_{i-\frac{1}{2},j} \Delta\eta \tag{3.8}$$

$$a_{i,j+1} = \rho_{i,j+\frac{1}{2}} d_{i,j+\frac{1}{2}} (h_1)_{i,j+\frac{1}{2}} \Delta\xi \tag{3.9}$$

$$a_{i,j-1} = \rho_{i,j-\frac{1}{2}} d_{i,j-\frac{1}{2}} (h_1)_{i,j-\frac{1}{2}} \Delta\xi \tag{3.10}$$

$$a_{i,j} = a_{i+1,j} + a_{i-1,j} + a_{i,j+1} + a_{i,j-1} \tag{3.11}$$

$$\begin{aligned} b_{i,j} = (\rho\hat{v_\xi})_{i+\frac{1}{2},j}\Delta\eta - (\rho\hat{v_\xi})_{i-\frac{1}{2},j}\Delta\eta + \\ (\rho\hat{v_\eta})_{i,j+\frac{1}{2}}(h_1)_{i,j+\frac{1}{2}}\Delta\xi - (\rho\hat{v_\eta})_{i,j-\frac{1}{2}}(h_1)_{i,j-\frac{1}{2}}\Delta\xi \end{aligned} \tag{3.12}$$

3.2 Pressure Correction Equation

The discretized momentum equations can be written in the following forms for the v_ξ and v_η respectively (see Fig. 2.7) as

$$a_{i+\frac{1}{2},j}v_{\xi i+\frac{1}{2},j} = \Sigma a_{nb}v_{\xi nb} - \Delta A\left(\frac{\partial p}{\partial \xi}\right)_{i+\frac{1}{2},j} + b_{v\xi} \tag{3.13}$$

$$a_{i,j+\frac{1}{2}}v_{\eta i,j+\frac{1}{2}} = \Sigma a_{nb}v_{\eta nb} - \Delta A\left(\frac{\partial p}{\partial \eta}\right)_{i,j+\frac{1}{2}} + b_{v\eta} \tag{3.14}$$

The subscript 'nb' denotes the neighboring points in the 5-point, finite-volume representation, b's are the source term in the momentum equations excluding the pressure gradients and ΔA is the area of the control volume.

The momentum equations for each control volume can be solved completely if the pressure field is known. Unless the correct pressure field is used, the tentative velocity field obtained after solving the momentum equations will not, in general, satisfy the continuity equation. If these imperfect fields are denoted by a star superscript, it follows then the starred variables satisfy the following discretized momentum equations

$$a_{i+\frac{1}{2},j}v^*_{\xi i+\frac{1}{2},j} = \Sigma a_{nb}v^*_{\xi nb} - \Delta A\left(\frac{\partial p^*}{\partial \xi}\right)_{i+\frac{1}{2},j} + b_{v\xi} \tag{3.15}$$

$$a_{i,j+\frac{1}{2}} v^*_{\eta_{i,j+\frac{1}{2}}} = \Sigma a_{nb} v^*_{\eta_{nb}} - \Delta A \left(\frac{\partial p^*}{\partial \eta}\right)_{i,j+\frac{1}{2}} + b_{v\eta} \tag{3.16}$$

If the imperfect pressure field p^* is improved or corrected, the resulting velocity field will progressively get closer to satisfying the continuity equation. The corrected pressure field can be obtained from

$$p = p^* + p' \tag{3.17}$$

where p' is the pressure correction field. The velocities will react to the change in pressure and the corresponding corrections can be introduced as

$$\begin{aligned} v_\xi &= v^*_\xi + v'_\xi \\ v_\eta &= v^*_\eta + v'_\eta \end{aligned} \tag{3.18}$$

where v'_ξ and v'_η are the velocity corrections due to the pressure correction p'. These velocity corrections have to be functionally related to the pressure correction.

The relation between the velocity correction v'_ξ and the pressure correction p' can be obtained by subtracting Eqn. 3.13 from Eqn. 3.15, and the resulting equation is

$$a_{i+\frac{1}{2},j} v'_{\xi_{i+\frac{1}{2},j}} = \Sigma a_{nb} v'_{\xi_{nb}} - \Delta A \left(\frac{\partial p'}{\partial \xi}\right)_{i+\frac{1}{2},j} + b_{v\xi} \tag{3.19}$$

The term $\Sigma a_{nb} v'_{\xi_{nb}}$ is omitted for computational simplicity (the justification for doing this will be discussed subsequently). The result is

$$v'_{\xi_{i+\frac{1}{2},j}} = -d'_{i+\frac{1}{2},j} \left(\frac{\partial p'}{\partial \xi}\right)_{i+\frac{1}{2},j} \tag{3.20}$$

where

$$d'_{i+\frac{1}{2},j} = \frac{\Delta A}{a_{i+\frac{1}{2},j}} \tag{3.21}$$

Similarly, the relation between v'_η and p' is obtained as

$$v'_{\eta_{i,j+\frac{1}{2}}} = -d'_{i,j+\frac{1}{2}} \left(\frac{\partial p'}{\partial \eta} \right)_{i,j+\frac{1}{2}} \tag{3.22}$$

where

$$d'_{i,j+\frac{1}{2}} = \frac{\Delta A}{a_{i,j+\frac{1}{2}}} \tag{3.23}$$

Therefore, the velocity correction formulae become

$$v_{\xi_{i+\frac{1}{2},j}} = v^*_{\xi_{i+\frac{1}{2},j}} - d'_{i+\frac{1}{2},j} \left(\frac{\partial p'}{\partial \xi} \right)_{i+\frac{1}{2},j} \tag{3.24}$$

$$v_{\eta_{i,j+\frac{1}{2}}} = v^*_{\eta_{i,j+\frac{1}{2}}} - d'_{i,j++\frac{1}{2}} \left(\frac{\partial p'}{\partial \eta} \right)_{i,j+\frac{1}{2}} \tag{3.25}$$

In deriving the velocity correction formulae, the terms $\Sigma a_{nb} v'_{\xi_{nb}}$ and $\Sigma a_{nb} v'_{\eta_{nb}}$ are omitted. The omission of any term would be unacceptable if the final solution does not satisfy the discretized forms of the momentum and continuity equations. However, this is not the case here because in the converged pressure field, the corresponding starred velocity obtained from solving the momentum equations satisfies the continuity equation. Therefore, the details of the construction of the velocity correction formula become irrelevant once the converged solution is obtained. As long as the correction model is reasonably related to the differential equation representing the physics of the problem (even though it may be an approximation), the solution procedure will not be prone to divergence.

The pressure correction p' has to be obtained in each iteration before the respective corrections can be made. This requires an equation for p'. An equation for the pressure correction p' can be obtained in the following manner in which the continuity equation is expressed in terms of the pressure correction. The discretized continuity equation

obtained in Chapter 2 is again reproduced here :

$$\left(\frac{\partial \rho_{ij}}{\partial t}\right) + (\rho v_\xi)_{i+\frac{1}{2},j}\Delta\eta - (\rho v_\xi)_{i-\frac{1}{2},j}\Delta\eta + (h_1 \rho v_\eta)_{i,j+\frac{1}{2}}\Delta\xi - (h_1 \rho v_\eta)_{i,j-\frac{1}{2}}\Delta\xi = 0 \tag{3.26}$$

The mass flux, say at the $(i+\frac{1}{2}, j)$ face, can be expanded and written as

$$\begin{aligned}(\rho v_\xi)_{i+\frac{1}{2},j}\Delta\eta &= \left[\rho\left(v_\xi^* + v_\xi'\right)\right]_{i+\frac{1}{2},j}\Delta\eta \\ &= \left[\left(\rho v_\xi^*\right)_{i+\frac{1}{2},j} + \left(\rho v_\xi'\right)_{i+\frac{1}{2},j}\right]\Delta\eta\end{aligned} \tag{3.27}$$

Substituting Eqns. 3.24 and 3.25 for v_ξ' in the above expression yields

$$(\rho v_\xi)_{i+\frac{1}{2},j}\Delta\eta = \left[\left(\rho v_\xi^*\right)_{i+\frac{1}{2},j} - \rho_{i+\frac{1}{2},j} d'_{i+\frac{1}{2},j}\left(\frac{\partial p'}{\partial \xi}\right)_{i+\frac{1}{2},j}\right]\Delta\eta \tag{3.28}$$

Similar expressions can be done for the mass flux at other faces and the resulting expressions are :

For the $(i-\frac{1}{2}, j)$ face,

$$(\rho v_\xi)_{i-\frac{1}{2},j}\Delta\eta = \left[\left(\rho v_\xi^*\right)_{i-\frac{1}{2},j} - \rho_{i-\frac{1}{2},j} d'_{i-\frac{1}{2},j}\left(\frac{\partial p'}{\partial \xi}\right)_{i-\frac{1}{2},j}\right]\Delta\eta \tag{3.29}$$

For the $(i, j+\frac{1}{2})$ face,

$$(\rho v_\eta)_{i,j+\frac{1}{2}}(h_1)_{i,j+\frac{1}{2}}\Delta\eta = \left[\left(\rho v_\eta^*\right)_{i,j+\frac{1}{2}} - \rho_{i,j+\frac{1}{2}} d'_{i,j+\frac{1}{2}}\left(\frac{\partial p'}{\partial \eta}\right)_{i,j+\frac{1}{2}}\right](h_1)_{i,j+\frac{1}{2}}\Delta\xi \tag{3.30}$$

For the $(i, j-\frac{1}{2})$ face,

$$(\rho v_\eta)_{i,j-\frac{1}{2}}(h_1)_{i,j-\frac{1}{2}}\Delta\eta = \left[\left(\rho v_\eta^*\right)_{i,j-\frac{1}{2}} - \rho_{i,j-\frac{1}{2}} d'_{i,j-\frac{1}{2}}\left(\frac{\partial p'}{\partial \eta}\right)_{i,j-\frac{1}{2}}\right](h_1)_{i,j-\frac{1}{2}}\Delta\xi \tag{3.31}$$

With proper pressure differencing and substituting these fluxes in the continuity equation and rearranging, it can be caste into the form

$$a_{i,j}p'_{i,j} = a_{i+1,j}p'_{i+1,j} + a_{i-1,j}p'_{i-1,j} + a_{i,j+1}p'_{i,j+1} + a_{i,j-1}p'_{i,j-1} - b_{i,j} \tag{3.32}$$

where

$$a_{i+1,j} = \rho_{i+\frac{1}{2},j} d_{i+\frac{1}{2},j} \Delta\eta \tag{3.33}$$

$$a_{i-1,j} = \rho_{i-\frac{1}{2},j} d_{i-\frac{1}{2},j} \Delta\eta \tag{3.34}$$

$$a_{i,j+1} = \rho_{i,j+\frac{1}{2}} d_{i,j+\frac{1}{2}} (h_1)_{i,j+\frac{1}{2}} \Delta\xi \tag{3.35}$$

$$a_{i,j-1} = \rho_{i,j-\frac{1}{2}} d_{i,j-\frac{1}{2}} (h_1)_{i,j-\frac{1}{2}} \Delta\xi \tag{3.36}$$

$$a_{i,j} = a_{i+1,j} + a_{i-1,j} + a_{i,j+1} + a_{i,j-1} \tag{3.37}$$

$$b_{i,j} = (\rho v_\xi{}^*)_{i+\frac{1}{2},j} \Delta\eta - (\rho v_\xi{}^*)_{i-\frac{1}{2},j} \Delta\eta + (\rho v_\eta{}^*)_{i,j+\frac{1}{2}} (h_1)_{i,j+\frac{1}{2}} \Delta\xi - (\rho v_\eta{}^*)_{i,j-\frac{1}{2}} (h_1)_{i,j-\frac{1}{2}} \Delta\xi \tag{3.38}$$

and the d's are defined as

$$d_{i+\frac{1}{2},j} = \frac{\Delta A}{a_{i+\frac{1}{2},j} \Delta\xi} \tag{3.39}$$

$$d_{i-\frac{1}{2},j} = \frac{\Delta A}{a_{i-\frac{1}{2},j} \Delta\xi} \tag{3.40}$$

$$d_{i,j+\frac{1}{2}} = \frac{\Delta A}{a_{i,j+\frac{1}{2}}\Delta\eta} \tag{3.41}$$

$$d_{i,j-\frac{1}{2}} = \frac{\Delta A}{a_{i,j-\frac{1}{2}}\Delta\eta} \tag{3.42}$$

It might be added as a clarification that the first term of the continuity equation goes to zero for the incompressible flow since the density doesn't change for such a flow. The pressure correction p' field obtained by solving the above equation is then used to update the imperfect velocity field obtained from solving the momentum equations according to Eqns. 3.24 and 3.25, which can now, with central differencing on the pressure gradients, be expressed as

$$v_{\xi_{i+\frac{1}{2},j}} = {v_\xi}^*_{i+\frac{1}{2},j} + d_{i+\frac{1}{2},j}\left({p'}_{i,j} - {p'}_{i+1,j}\right) \tag{3.43}$$

$$v_{\eta_{i,j+\frac{1}{2}}} = {v_\eta}^*_{i,j+\frac{1}{2}} + d_{i,j+\frac{1}{2}}\left({p'}_{i,j} - {p'}_{i+1,j}\right) \tag{3.44}$$

In the SIMPLER algorithm, the pressure correction equation is NOT used to update the pressure, which is the practice in SIMPLE algorithm. Instead, the pressure correction is used only to update or to correct velocities. The pressure is updated by solving the pressure equation.

3.3 Solution of the Algebraic Equations

The discretized equations derived so far are coupled and non-linear, and thus cannot be solved directly. The coefficients a's and the source terms b's are functions of the dependent variables. Such difficulties with non-linearity in the equation can be remedied by using an appropriate linearization technique such as Newton's. No linearization is used in the present analysis but instead, the coefficients and source terms are lagged by

computing them using the currently available field values. Even though the coefficients and the source terms are lagged by one iteration, when the solution converges, all the equations are satisfied implicitly.

In the present work, a "segregated" approach is used to solve the discretized equations where each of the governing equations is solved sequentially. In each time step, the simultaneous algebraic equations of the form expressed by Eqn. 3.15 for the entire grid mesh are solved by an iterative line-by-line elimination procedure. In this procedure, when a line of constant ξ is solved, the contribution from adjacent constant ξ line is added to the source term b_{v_ξ} and thus reducing the equation set to a tri-diagonal form. The resulting tri-diagonal system is then solved by the Tri-Diagonal Matrix Algorithm (TDMA). Alternate ξ and η sweeps in the computational plane are performed to improve the overall convergence history even though absolute convergence is not required in each time step. One advances to the next time step when a sufficient converged criterion is met. An under-relaxation is generally required between each TDMA update to prevent the solution from diverging.

CHAPTER 4 CIRCULAR BOUNDARY IMPLEMENTATION

In this chapter, the implementation of the circular boundary is discussed. In the present work, circular boundary condition is implemented to see the vortex shedding past a full cylinder for different Reynolds numbers. Vortex shedding is not seen in Steady Navier-Stokes formulation. In the present work, the unsteady behavior of the flow past a cylinder is the focus and hence Crank Nicolson and Fully Implicit were implemented for time integration. However, as earlier suggested, the vortex shedding is not seen with just a half cylinder even with proper time integration, and it is essential to have a full cylinder and hence a circular boundary implementation. A brief description is given below on how circular boundary condition is implemented.

4.1 Introduction

A diagram for cyclic boundary is presented in fig 4.1 . The domain extends from cell $ib1$ to $ie1$ with cell ib overlapping with cell $ie1$ and cell ie overlapping with cell $ib1$. Therefore, throughout all the geometry calculations, all geometry parameters needs to be copied from $ib1$ to ie and from $ie1$ to ib.

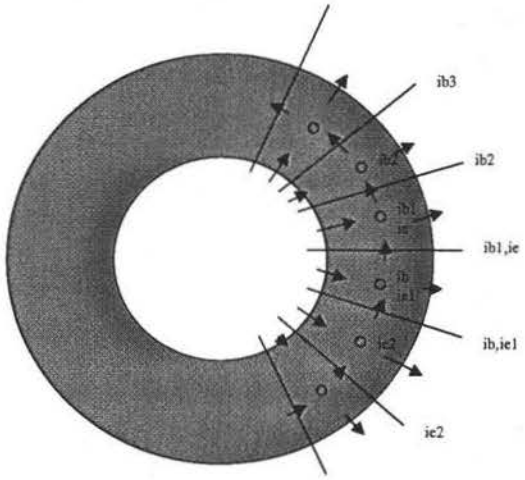

Figure 4.1 Cell diagram with a cyclic boundary in x-direction

4.2 Boundary Condition

For a cyclic boundary, the determination of the inlet and the outlet boundaries is slightly more complicated than non-cyclic boundary. Velocities at the cyclic boundary need to be calculated and therefore, the cyclic boundary can neither be an inlet nor an outlet. In summary, a boundary cannot be an inlet or outlet if it is:

- viscous wall
- inviscid wall
- cyclic boundary

If the inlet velocity is specified in the global Cartesian coordinates, the velocity needs to be decomposed in the general orthogonal system before the inlet and outlet boundaries can be specified. For this case, a boundary can serve both as an inlet and an outlet.

4.3 Solver

Below is the description of a comparison of the SOLVER for cyclic and non-cyclic boundaries for SIMPLER algorithm in general.

The SIMPLER algorithm for a cyclic boundary is as follows:

- The fluxes are calculated using the velocity from the previous iteration. If the boundary is not cyclic, then the staggered cells at the boundary are composed of one and a half cells. If it is cyclic, regular staggered cells are used.
- The coefficients and the source terms (without the Δp term) of the momentum equations are calculated.
- The unsteady terms are calculated and the sources and coefficients are modified using the weighting factor.
- The relaxations are added.
- The du, dv (area/aij) terms are calculated. If not cyclic, the du terms at the boundary are set to zero. If cyclic, the du terms have to be calculated at the boundary.
- The coefficients of the pressure equation are calculated. If not cyclic, the pressure coefficients at the boundary are set to zero. If cyclic, they are calculated regularly.
- The source of pressure coefficients is calculated. If cyclic, the boundary fluxes are copied from the corresponding cells.
- Pressure is now solved.
- If cyclic, the boundary pressures are copied from the corresponding cells.
- The pressure is added to the momentum source (bu,bv).
- The velocities are solved for (u,v).
- The source terms of the pressure correction equation is calculated (bpp).
- The pressure correction is solved for (pp).
- If cyclic, the pressure correction from the corresponding cells are copied.
- Mass convergence is calculated.

- The velocities are corrected using the pressure correction.

It should be noted that when solving for the momentum equations with cyclic boundary, there is one additional cell that needs to be solved. For example, if the X-boundary is cyclic, then the u velicity needs to be solved from index $ib1$ to $ie1$, instead of $ib2$ to $ie1$ for non-cyclic boundary.

CHAPTER 5 RESULTS

The objective of the present work is to study the flow over a full cylinder for a wide range of Reynolds numbers. Since the present work involves studying both Fully Implicit and Crank Nicolson, the results will be presented in two main headings: Fully Implicit and Crank Nicolson. After studying the case of a full cylinder, four cases of ellipse will be studied to gain a thorough knowledge about the unsteady behavior of bluff bodies. Two of those ellipse cases will be of aspect ratio less than one, and two of them will have aspect ratio more than one.

5.1 Circular Cylinder

Figs. 5.1 and 5.2 show one of the grids that was used for the calculation of circular cylinder. The grid was uniform in the circumfirencial direction and stretched near the wall in the radial direction (see Fig. 5.2) so that it can capture the boundary layer properly.

Flow past a circular cylinder is essentially unsteady in nature. By unsteady, one means that after a while, the flow starts to oscillate and vortex shedding can be observed. Both the schemes, Fully Implicit and Crank Nicolson, capture this unsteady effect very well, as will be shown later.

Fig. 5.3 and Fig. 5.4 show the comparison of the present results, *i.e*, Fully Implicit and Crank Nicolson with the existing results obtained from Schlichting [40]. For comparison, C_d and Strouhal number were compared with the extisting results for different

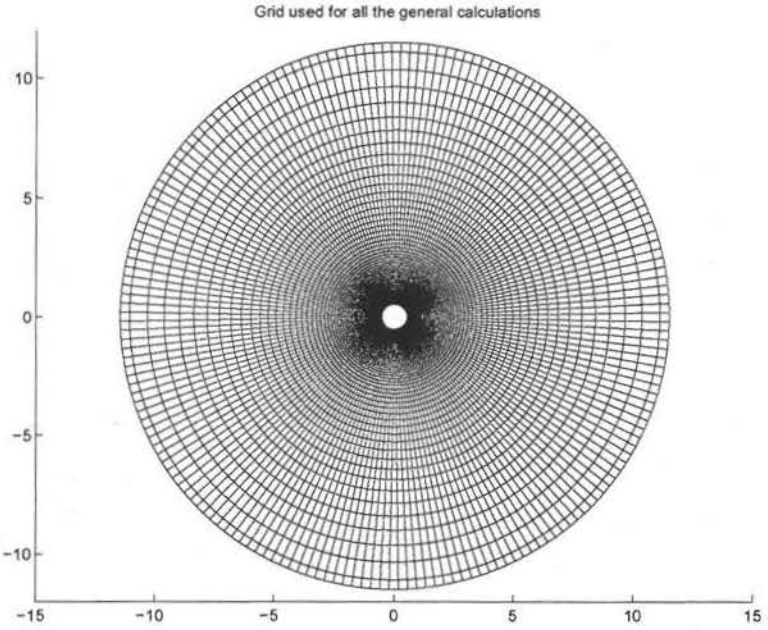

Figure 5.1 186x101 grid

Reynolds number and they agree well. C_d was calculated using the expression

$$C_d = \frac{D}{\frac{1}{2}\rho V^2} \tag{5.1}$$

where D is drag per unit length of the cylinder and it comprises of two components, namely, Pressure drag and Skin friction drag. The Reynolds number is given by

$$Re = \frac{\rho V d}{\mu} \tag{5.2}$$

where d is the diameter of the cylinder, V is the freestream velocity, ρ is density and μ is the viscosity of the fluid. The Strouhal number is dependent on the frequency at which the vortex shedding takes place in an unsteady flow such as the present case. It is expressed as

$$S = \frac{nd}{V} \tag{5.3}$$

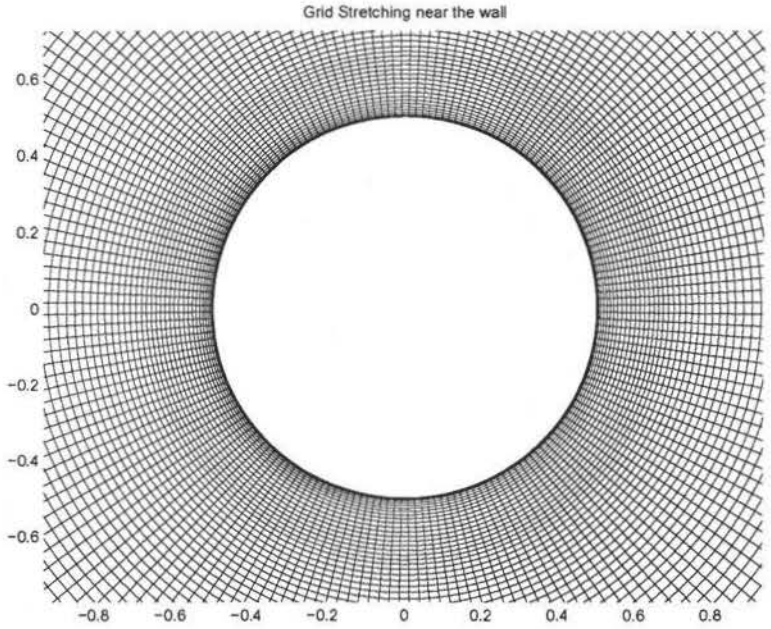

Figure 5.2 Stretching of the grid in the radial direction near the wall

where S is the Strouhal number, n is the frequency of the shedding, d is the diameter of the cylinder and V is the freestream velocity.

To ensure that the solution is grid independent, three different grids were used to study the nature of the results. All three of the grids were circumfirencially uniform grids and radially stretched at the wall as shown in Figs. 5.1 and 5.2. The three grids used had the same radial widths but different circumfirencial widths. Three grids used were 186x101, 370x101 and 738x101, and hence the circumfirencial width was half and one-fourth times the original, respectively. The 186x101 grid was shown before. Figs. 5.5 and 5.6 show the other two grids that were used.

Pressure drag was plotted with respect to time for each case, and the result is shown in Fig. 5.7. As it could be seen, the mean pressure drag value approached an assymptotic value. The difference was negligible for the 370x101 and 738x101 grid systems. Hence, for all comparisons, the 370x101 grid was used. However, the 186x101 grid was also able to capture the unsteady effects of the flow, and since it took much less time, it was

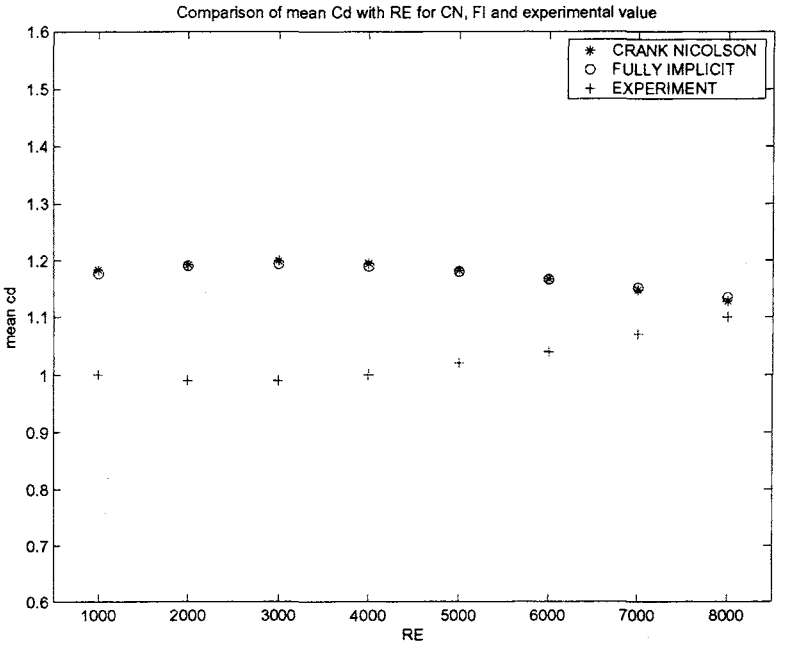

Figure 5.3 Comparison of cd values for different Reynolds numbers

preferred to the 370x101 grid while a particular cycle was studied.

Now the time history of C_d using Fully Implicit and Crank Nicolson will be shown for different Reynolds numbers. The Reynolds numbers that were considered were 1000 to 8000 with an increment of 1000. All the other flow parameters were kept constant other than the flow velocity. Flow velocity was varied from $5m/s$ to $40m/s$. It was observed that as the flow velocity was increased, the time period of the oscillations decreased, and hence the frequency increased. However, the Strouhal number remained constant at a value close to 0.18, which matched the experimental one. For both the schemes, the time increment, *i.e*, dt, was chosen to be 0.001s.

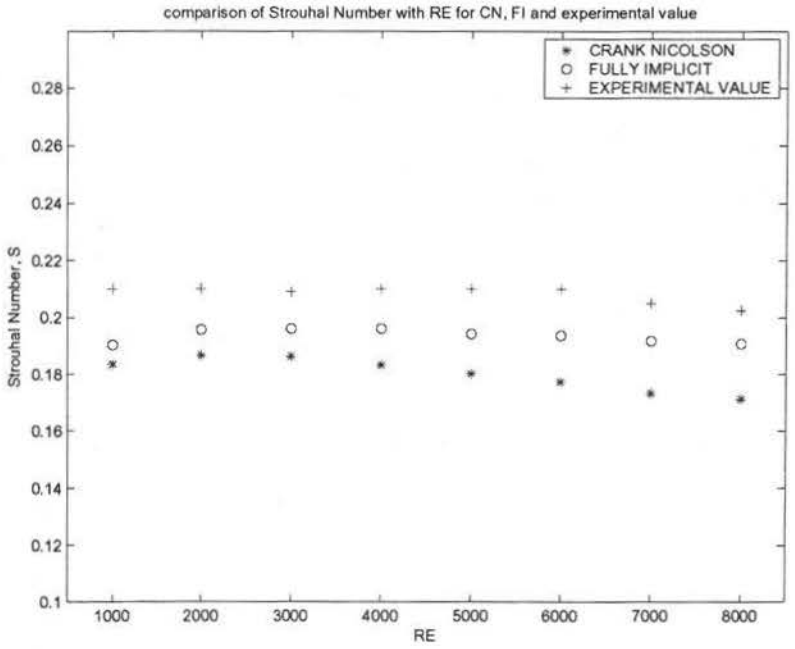

Figure 5.4 Comparison of strouhal number for different Reynolds numbers

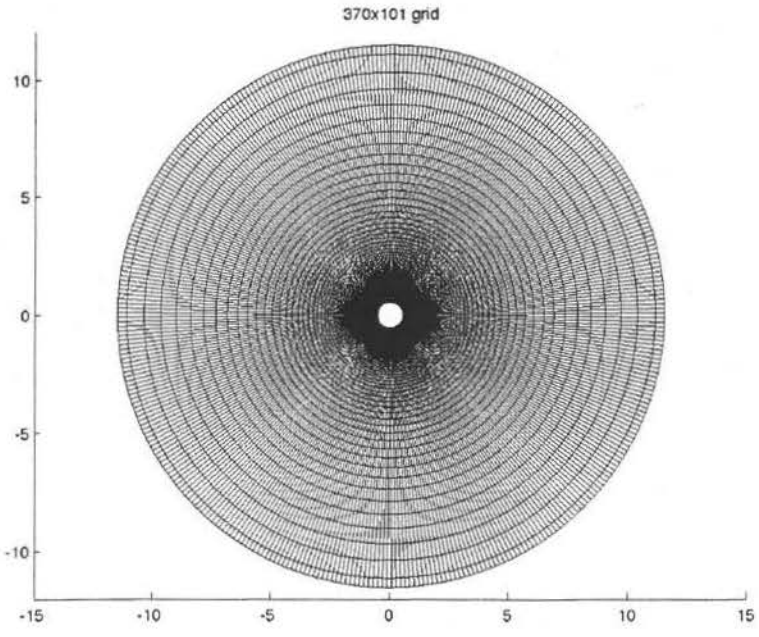

Figure 5.5 370x101 grid

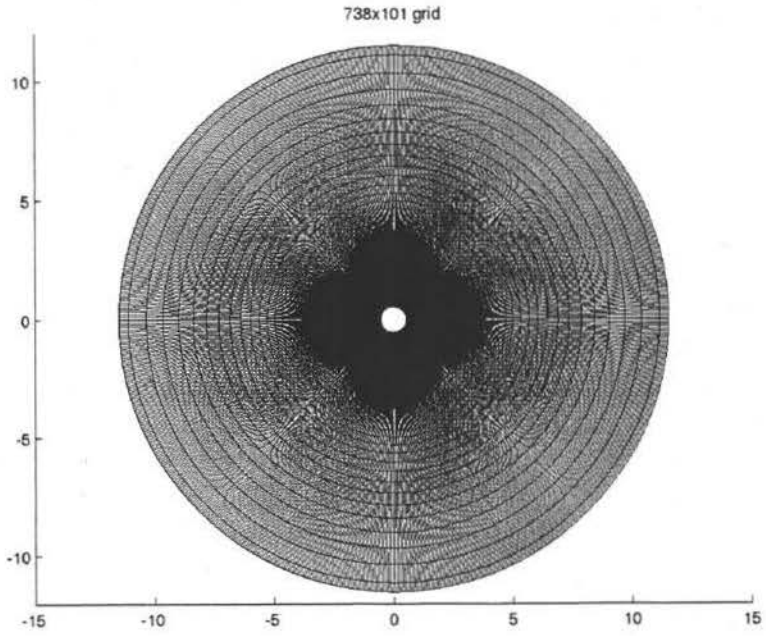

Figure 5.6 738x101 grid

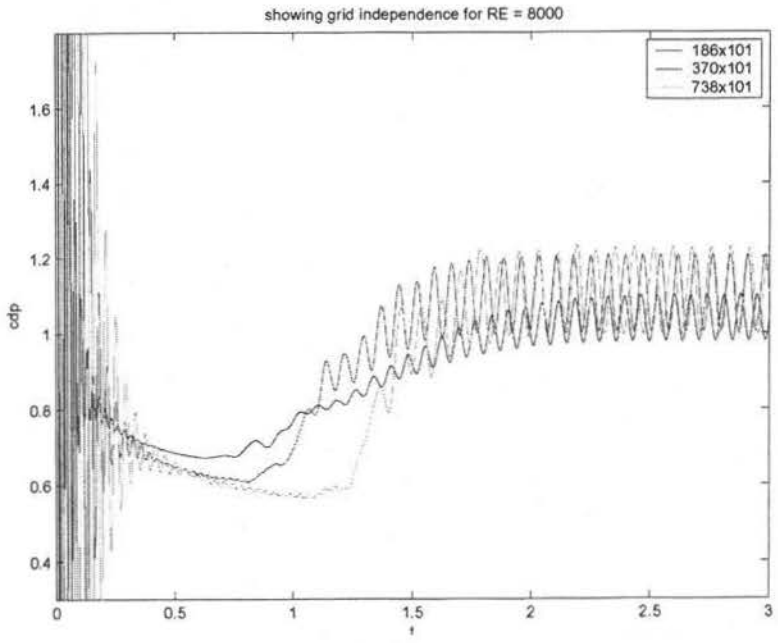

Figure 5.7 Showing grid independence for Re = 8000

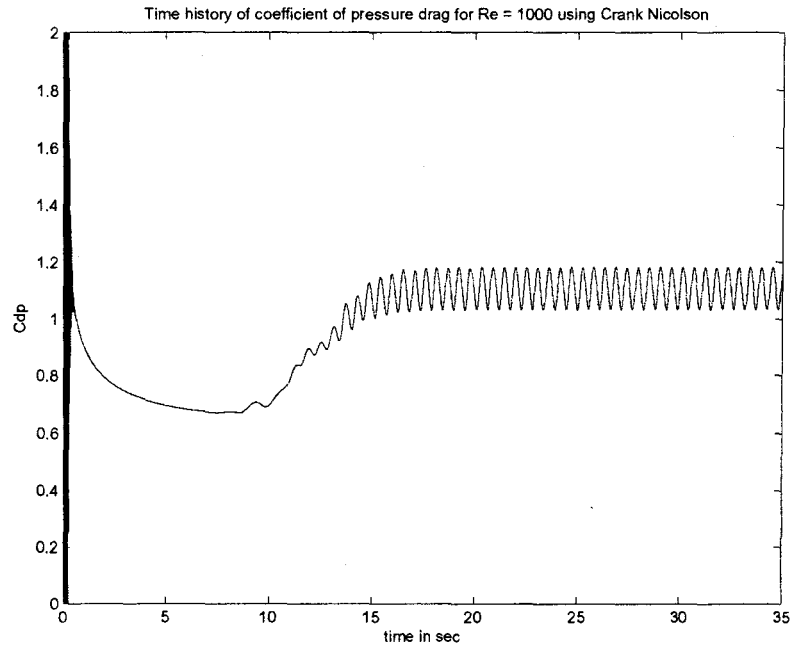

Figure 5.8 Time history of pressure drag using Crank Nicolson for Re = 1000

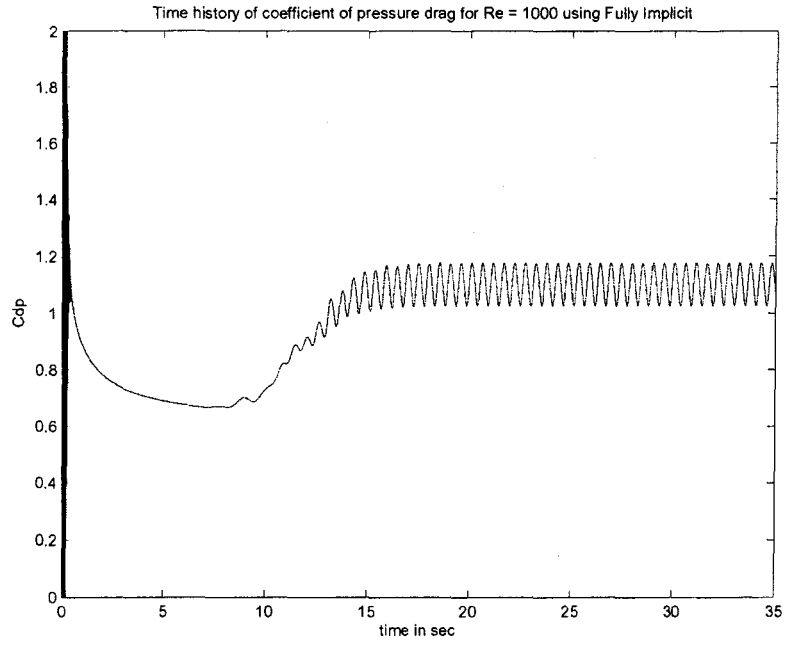

Figure 5.9 Time history of pressure drag using Fully Implicit for Re = 1000

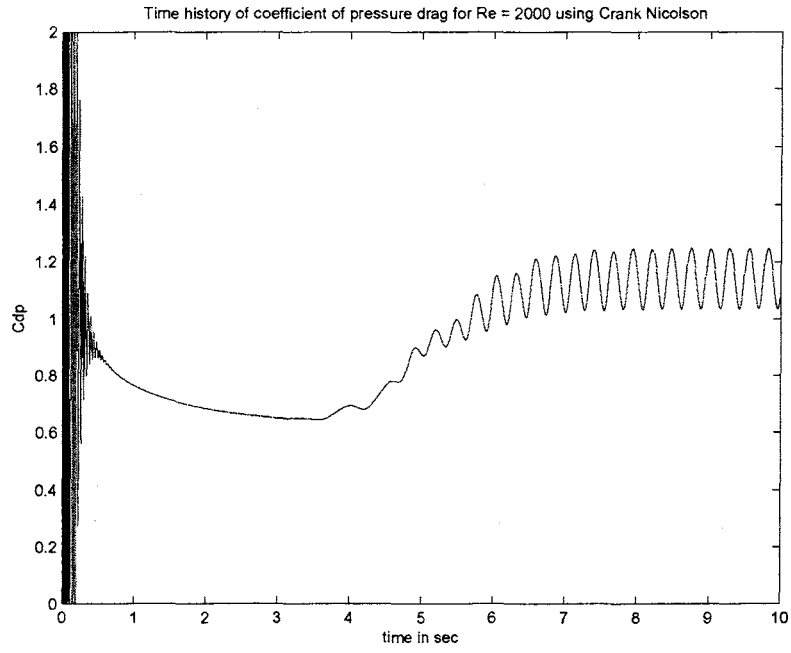

Figure 5.10 Time history of pressure drag using Crank Nicolson for Re = 2000

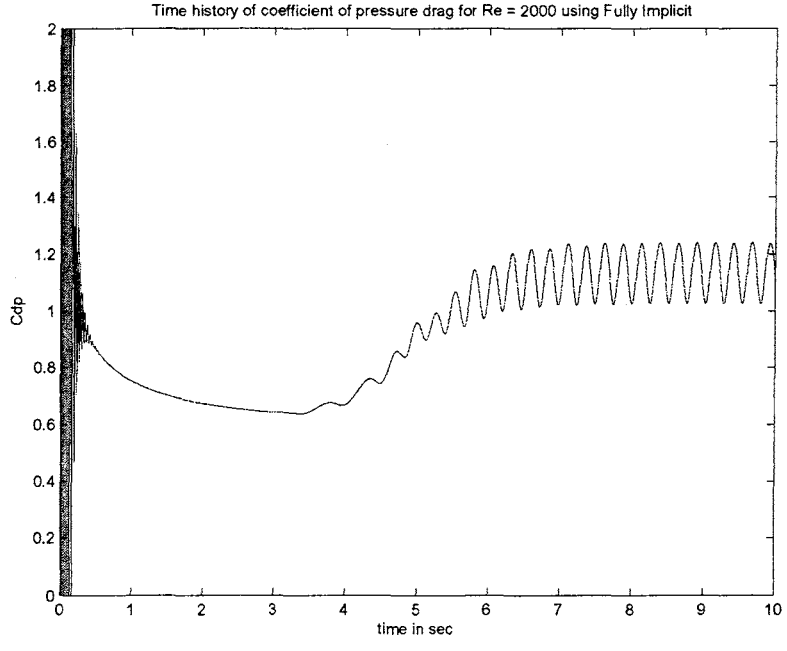

Figure 5.11 Time history of pressure drag using Fully Implicit for Re = 2000

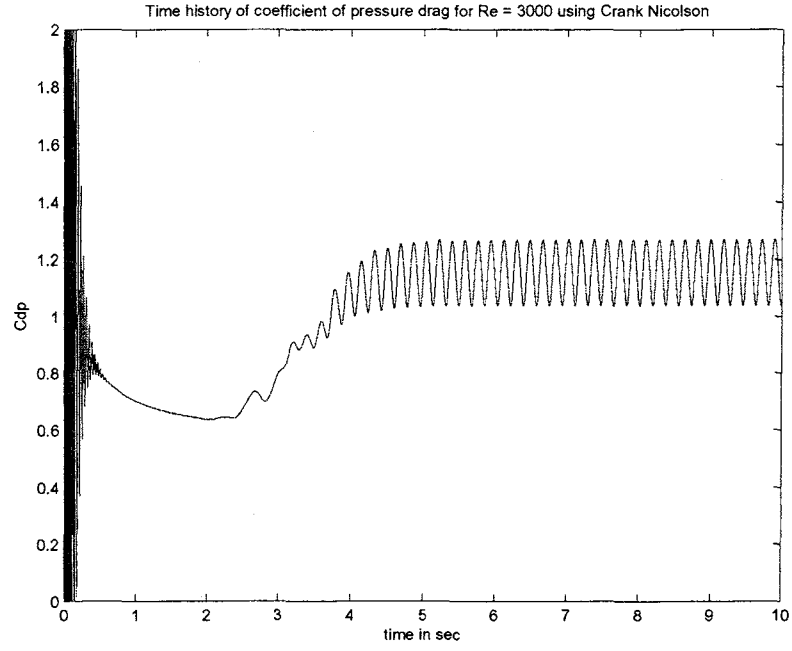

Figure 5.12 Time history of pressure drag using Crank Nicolson for Re = 3000

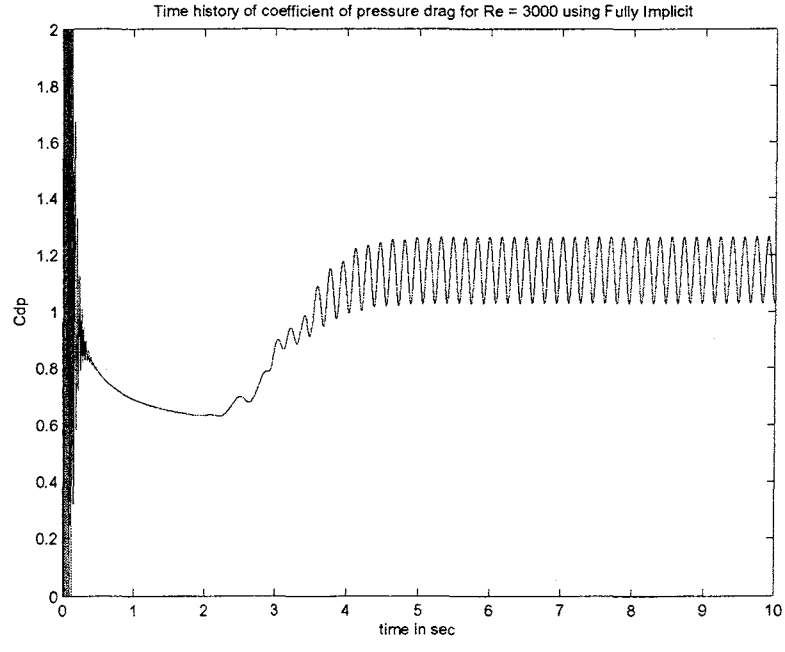

Figure 5.13 Time history of pressure drag using Fully Implicit for Re = 3000

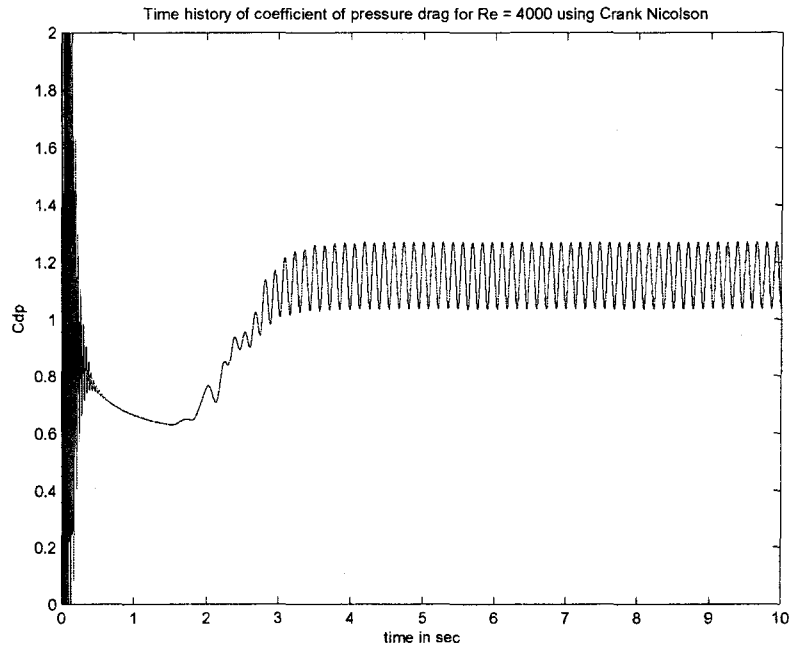

Figure 5.14 Time history of pressure drag using Crank Nicolson for Re = 4000

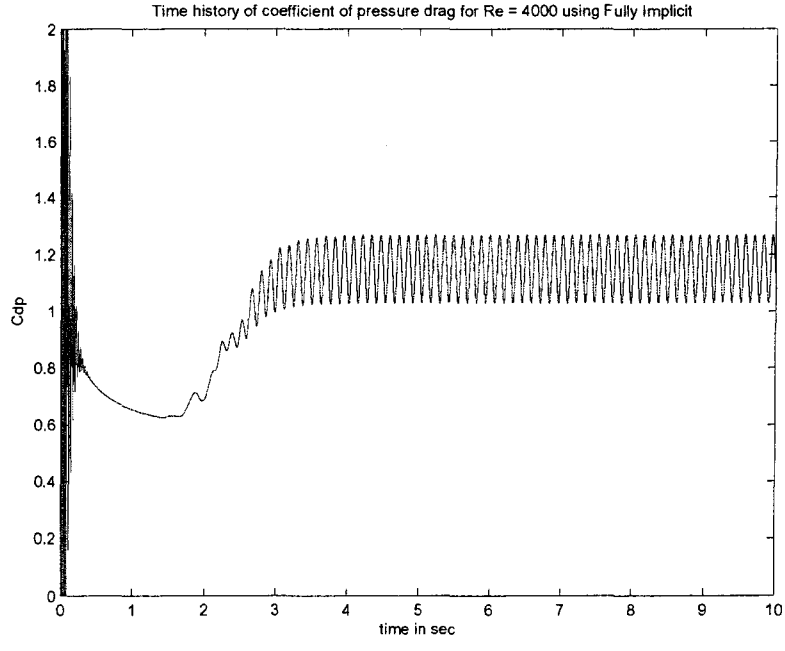

Figure 5.15 Time history of pressure drag using Fully Implicit for Re = 4000

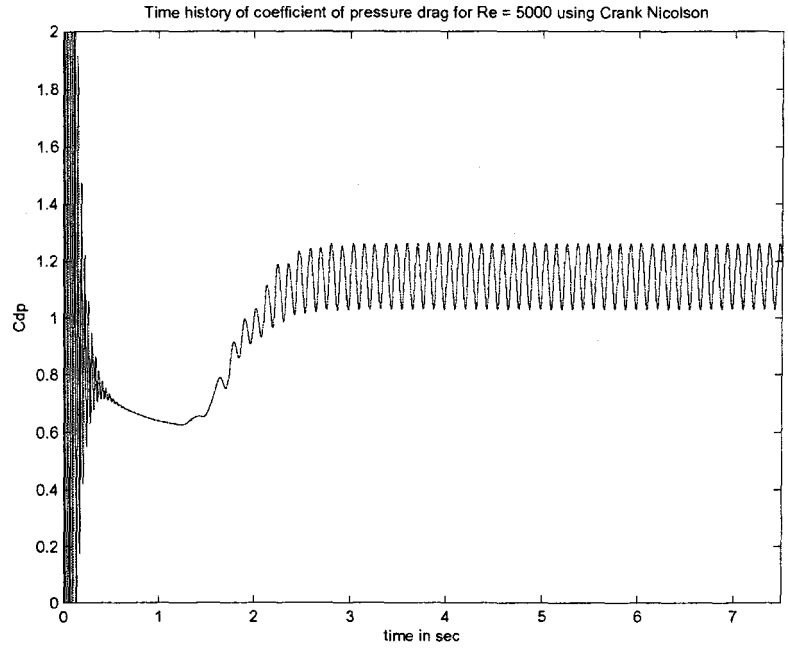

Figure 5.16 Time history of pressure drag using Crank Nicolson for Re = 5000

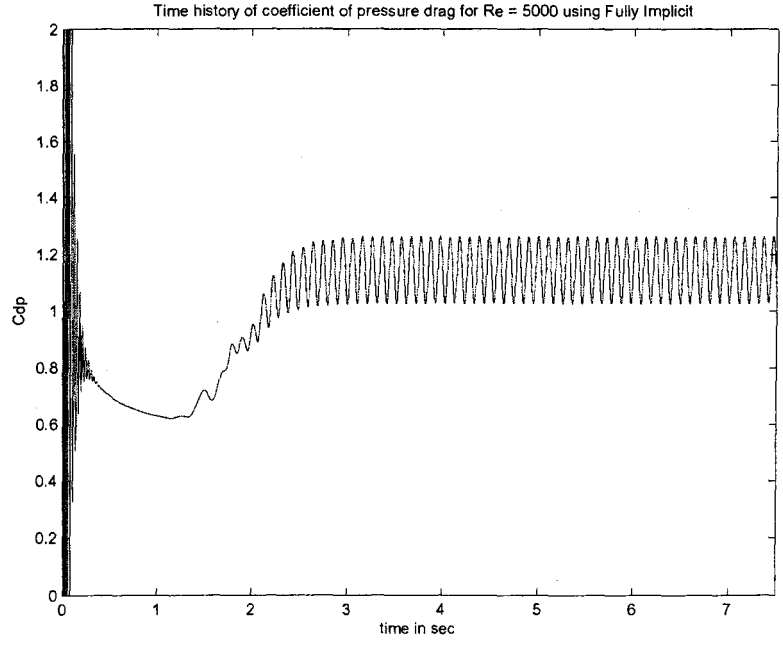

Figure 5.17 Time history of pressure drag using Fully Implicit for Re = 5000

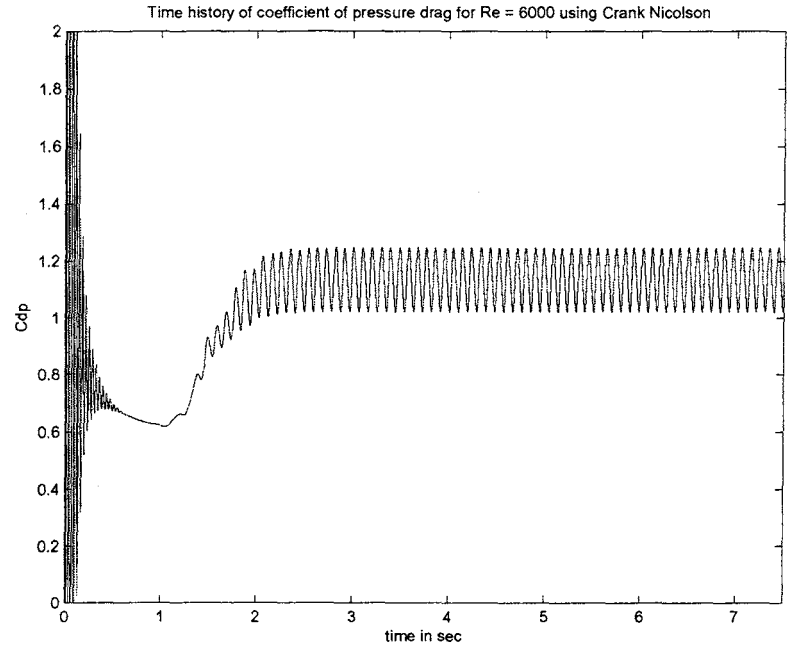

Figure 5.18 Time history of pressure drag using Crank Nicolson for Re = 6000

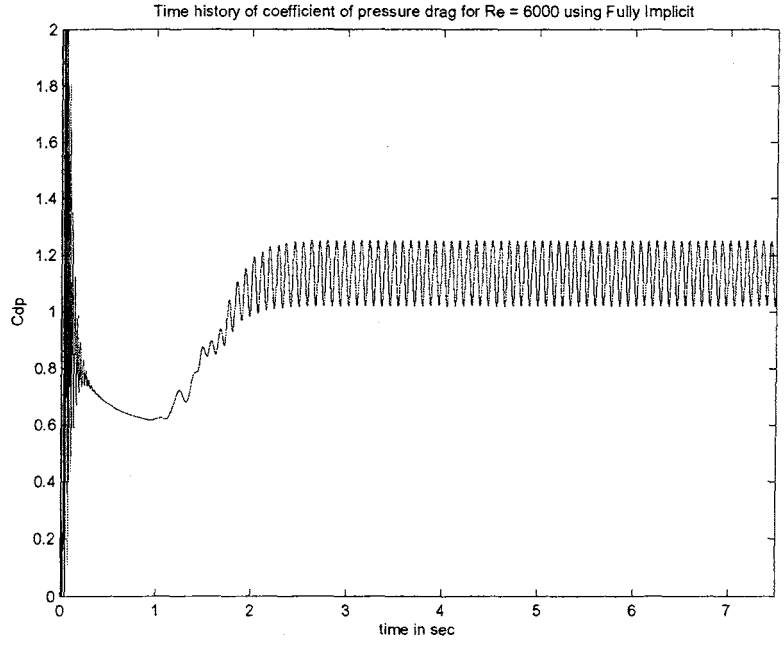

Figure 5.19 Time history of pressure drag using Fully Implicit for Re = 6000

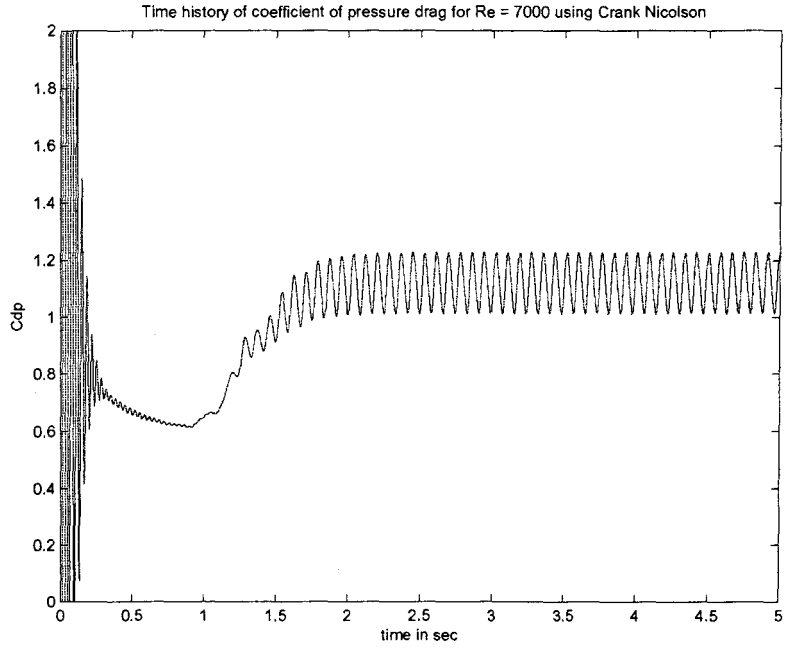

Figure 5.20 Time history of pressure drag using Crank Nicolson for Re = 7000

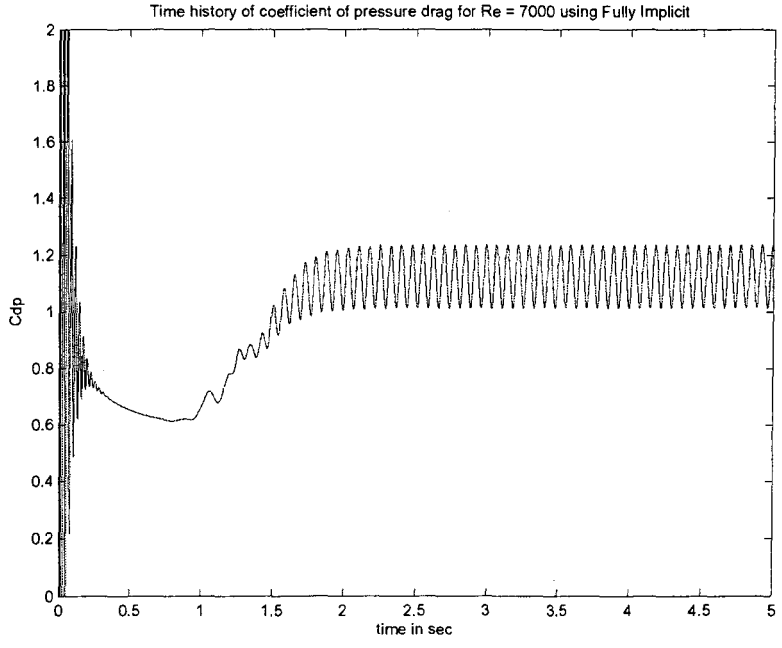

Figure 5.21 Time history of pressure drag using Fully Implicit for Re = 7000

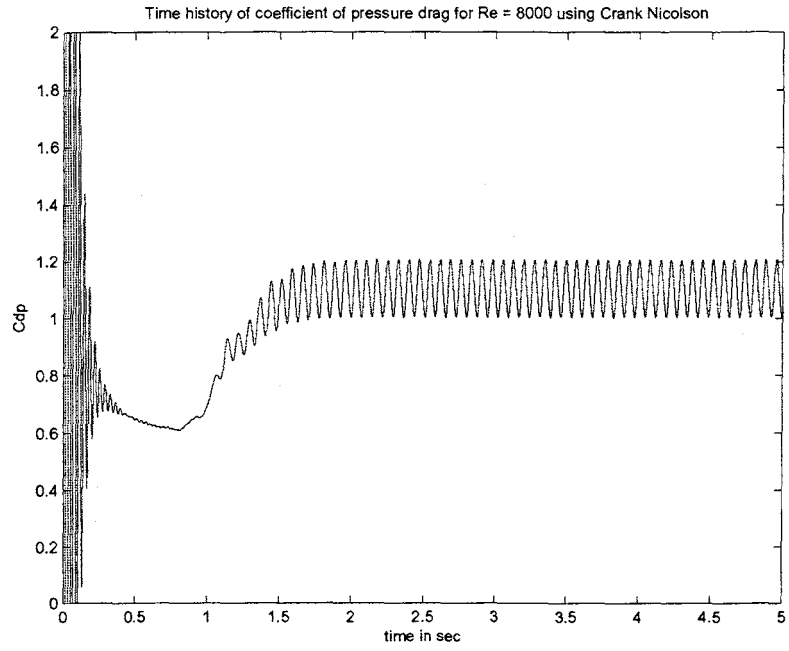

Figure 5.22 Time history of pressure drag using Crank Nicolson for Re = 8000

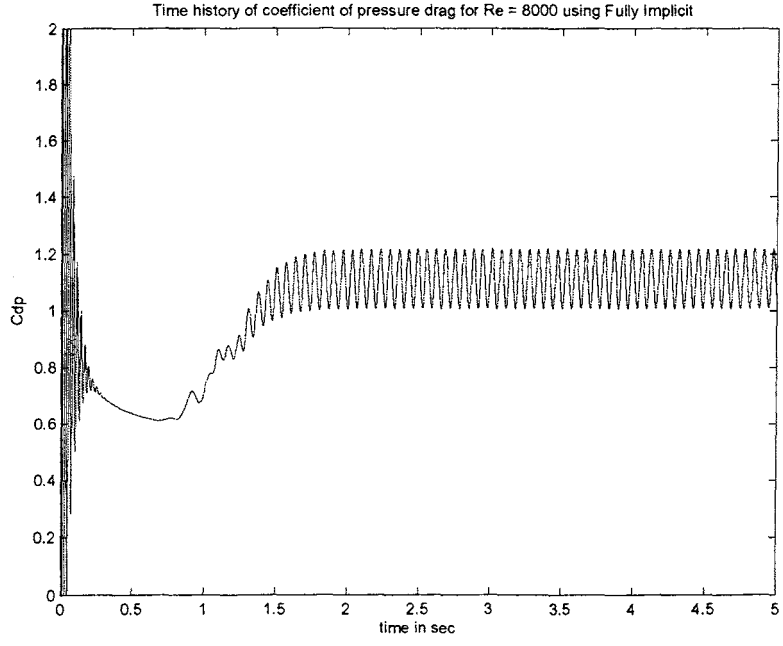

Figure 5.23 Time history of pressure drag using Fully Implicit for Re = 8000

The mean C_d value remained almost the same for both the schemes. A little difference in the Strouhal number was observed for the two different schemes. The unsteady effects were clearly seen in the time histories of C_d' presented. Now a particular case will be taken and studied in detail. For that, the case with Reynolds number 5000 was chosen. A full cycle is thoroughly looked at by plotting coefficient of pressure and coefficient of skin friction at nine significant stations. To see the vortex shedding, the streamline contours were also plotted for those nine stations. The results will be shown in two subsections, *i.e*, Crank Nicolson and Fully Implicit.

5.1.1 Crank Nicolson Results

For Crank Nicolson, the cycle that was chosen was such that it was from top vortex shedding to top vortex shedding with the bottom vortex shedding in the midway (Fig. 5.24).

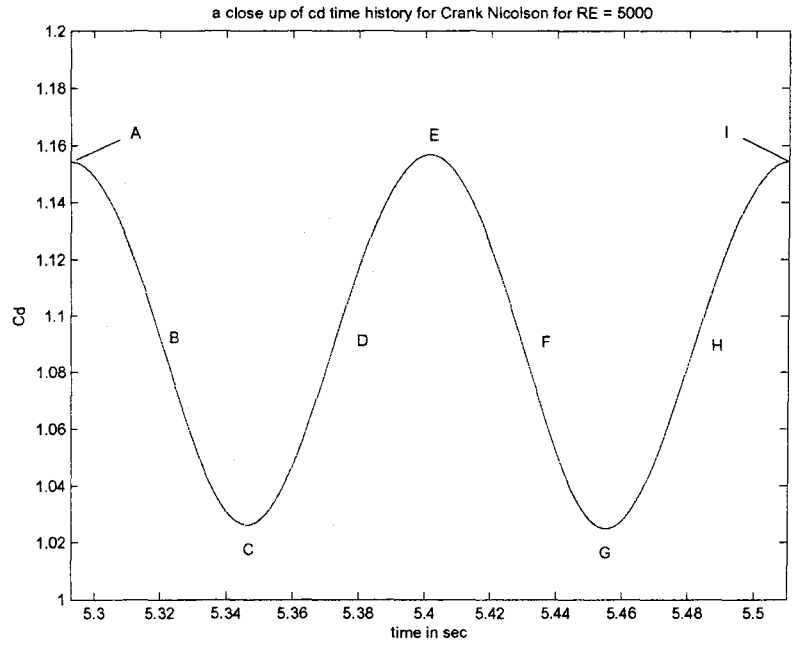

Figure 5.24 A closeup look at a top shed to top shed cycle using Crank Nicolson

Figs. 5.25 through 5.33 show the skin friction coefficient obtained by Crank Nicolson at the nine stations shown in Fig. 5.24. It could be observed that the C_f value becomes negative even at the top surface of the cylinder, which means that in those places flow was recirculating. Figs. 5.34 through 5.42 show the coefficients of pressure at those nine stations.

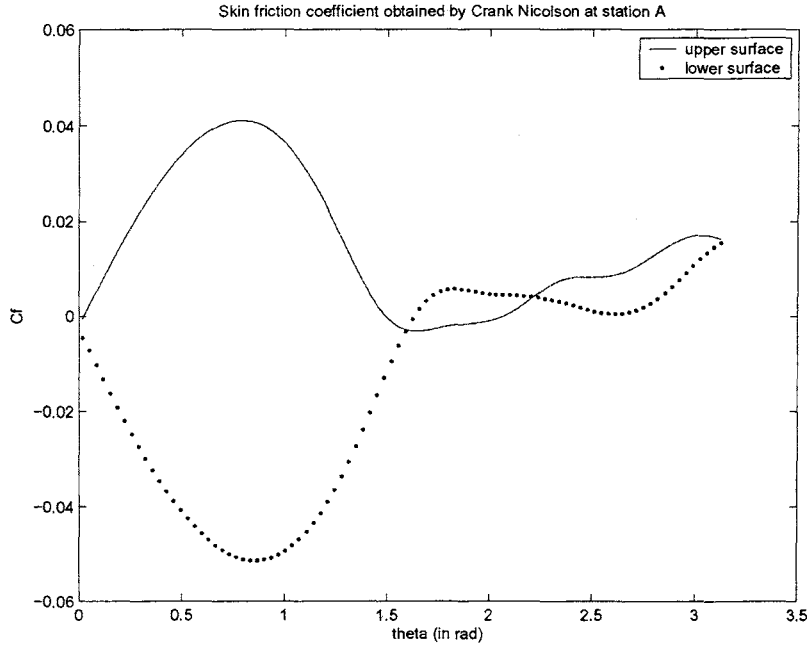

Figure 5.25 Skin friction coefficient obtained by Crank Nicolson at t = 5.293s (Station A, top shed)

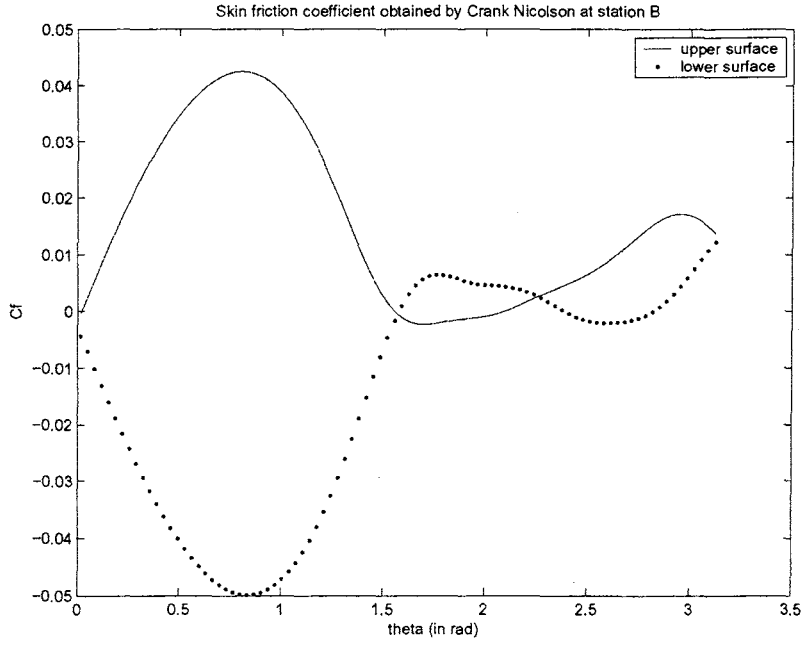

Figure 5.26 Skin friction coefficient obtained by Crank Nicolson at t = 5.320s (Station B, growth of bottom vortex)

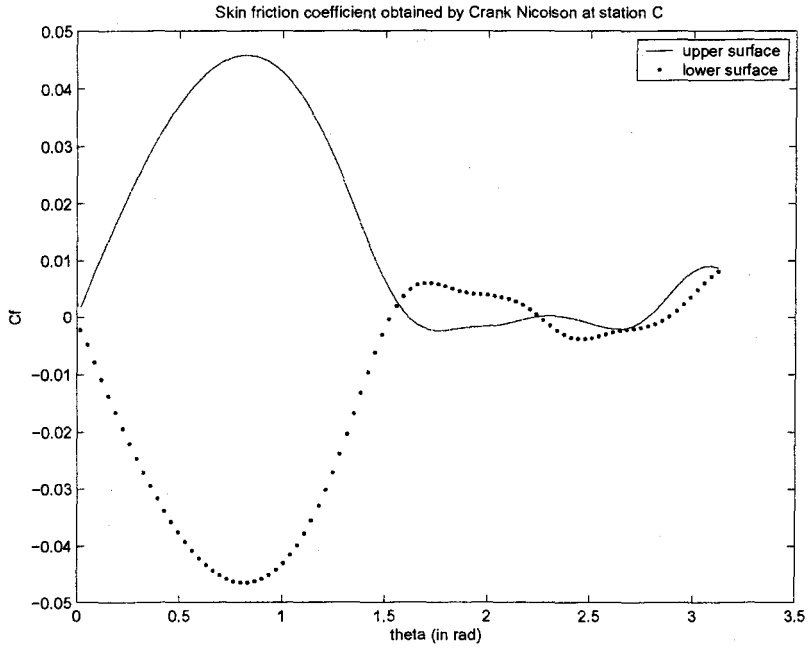

Figure 5.27 Skin friction coefficient obtained by Crank Nicolson at t = 5.346s (Station C, first minimum drag point)

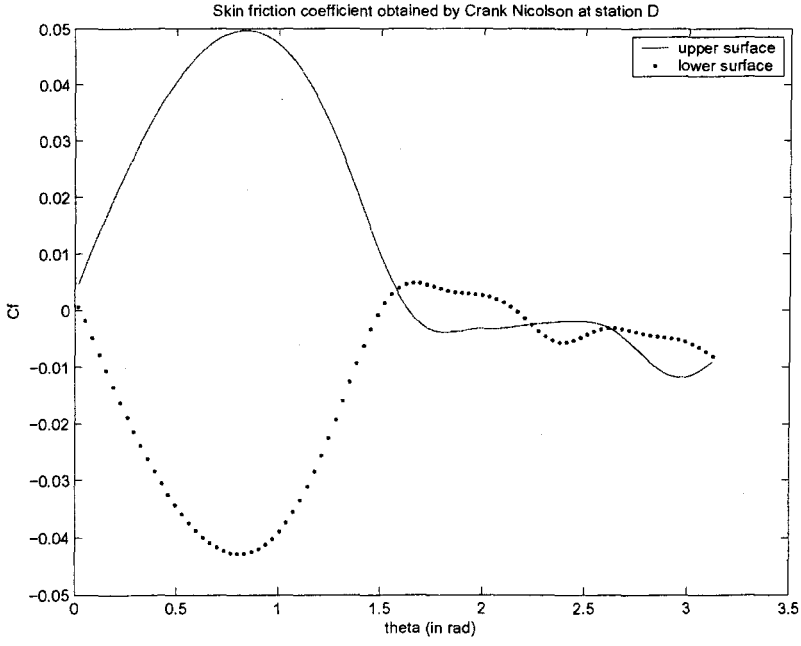

Figure 5.28 Skin friction coefficient obtained by Crank Nicolson at t = 5.373s (Station D, growth of bottom vortex)

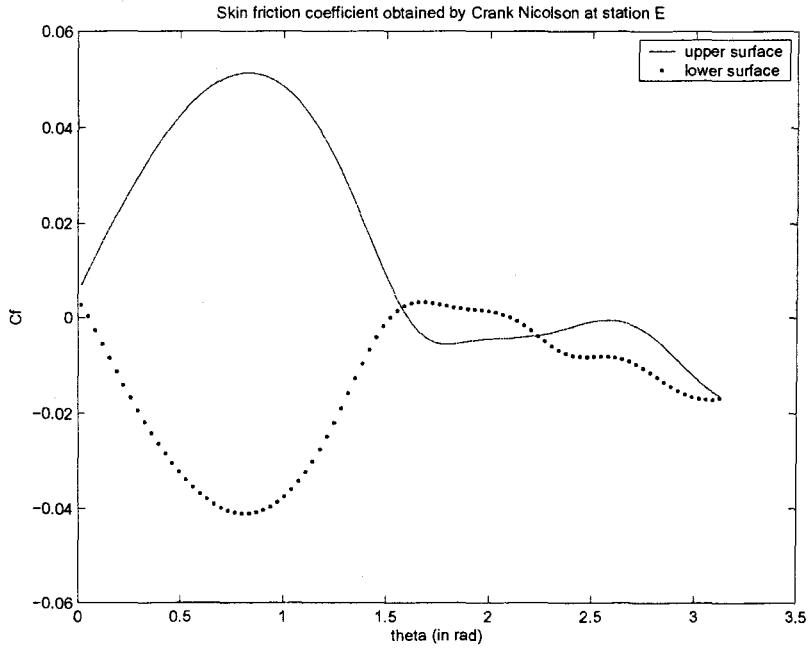

Figure 5.29 Skin friction coefficient obtained by Crank Nicolson at t = 5.401s (Station E, bottom shed)

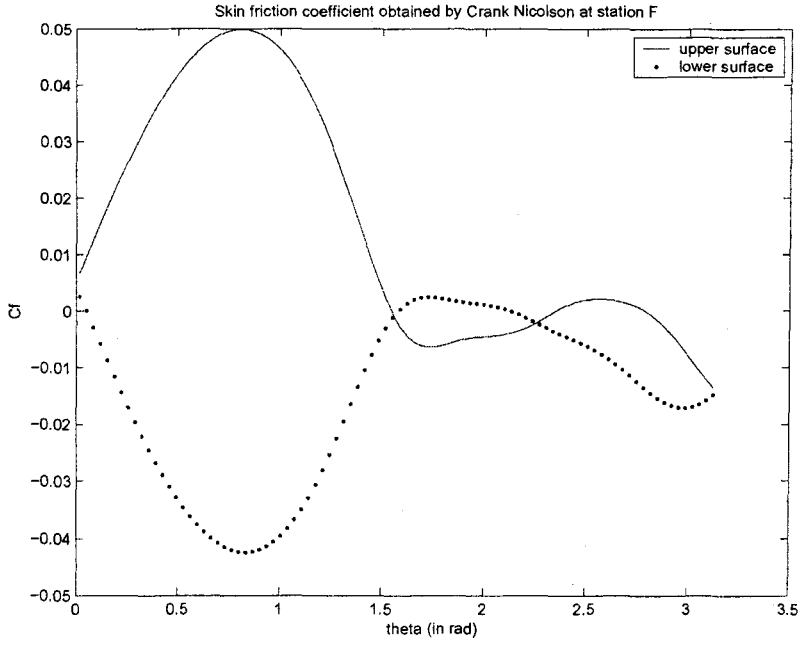

Figure 5.30 Skin friction coefficient obtained by Crank Nicolson at t = 5.428s (Station F, growth of top vortex)

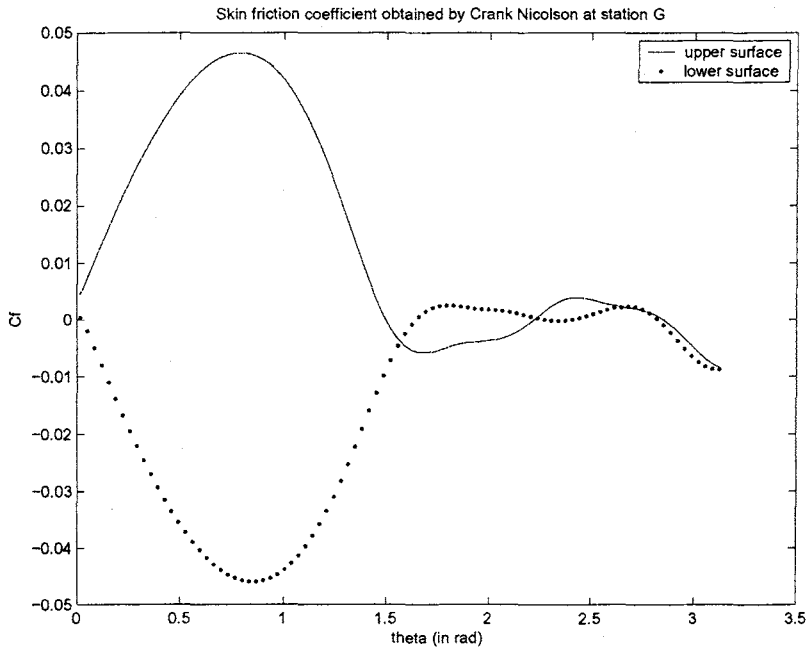

Figure 5.31 Skin friction coefficient obtained by Crank Nicolson at t = 5.455s (Station G, second minimum drag point)

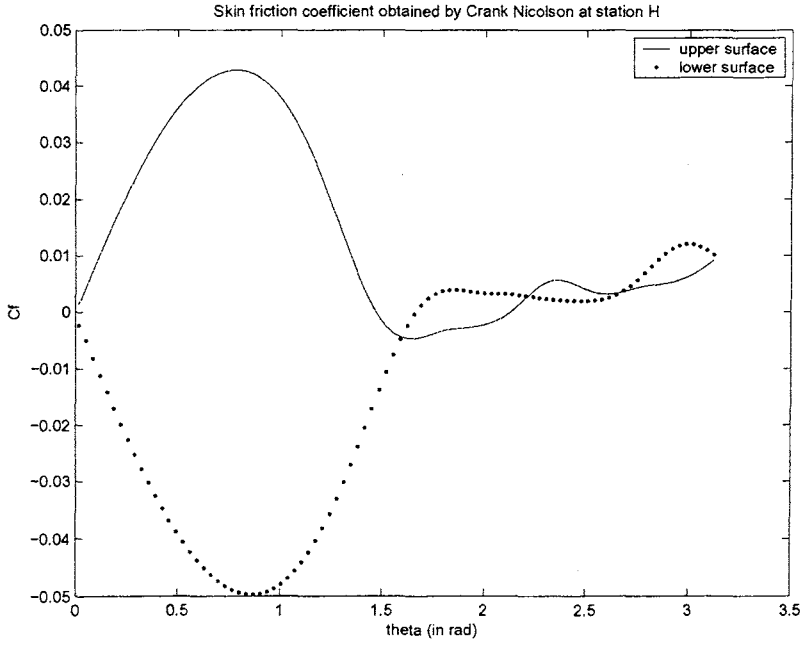

Figure 5.32 Skin friction coefficient obtained by Crank Nicolson at t = 5.482s (Station H, growth of top vortex)

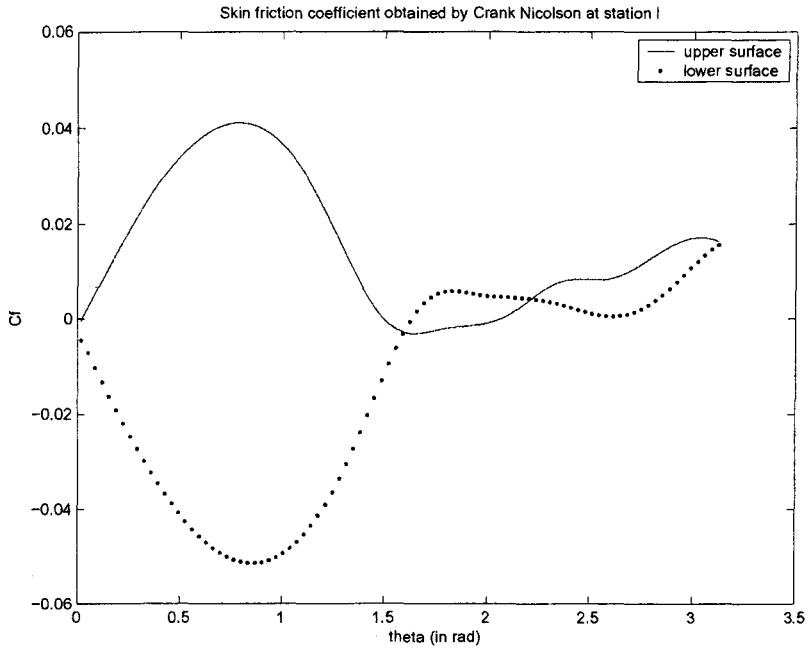

Figure 5.33 Skin friction coefficient obtained by Crank Nicolson at t = 5.510s (Station I, top shed)

If the nine plots for coefficient of skin friction (Figs. 5.25 through 5.33) are observed closely, they reveal an interesting fact. For the top shed, the maximum absolute C_f value for the upper surface is about 0.04 and for the lower surface, it is about 0.05. For the bottom shed, the maximum absolute C_f value for the upper surface becomes 0.05 and that for the lower surface becomes 0.04. Along with that, the other plots at different times of the cycle shows that for a particular cycle, the behavior of top half and the bottom half of the cylinder is symmetric.

Next, the coefficient of pressure (C_p) will be plotted at these nine stations.

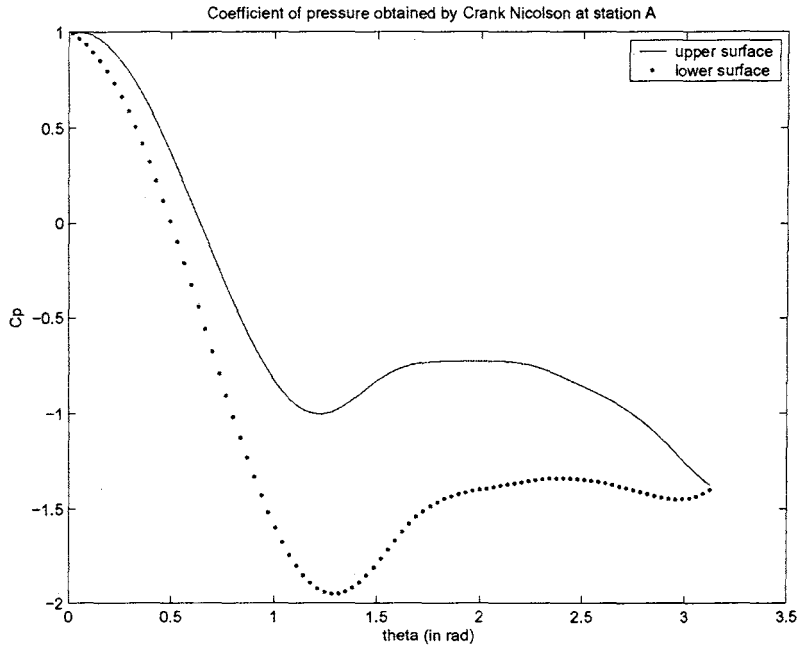

Figure 5.34 Coefficient of pressure obtained by Crank Nicolson at t = 5.293s (Station A, top shed)

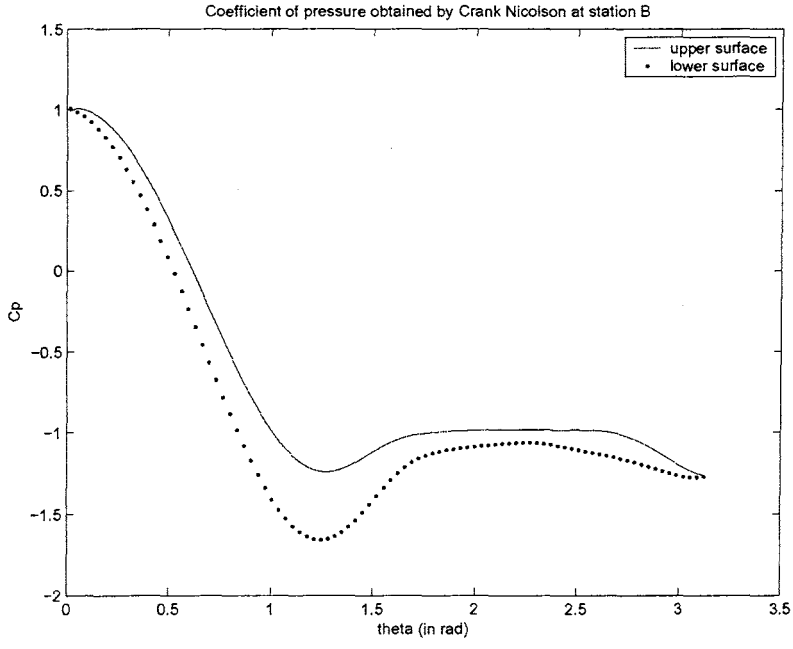

Figure 5.35 Coefficient of pressure obtained by Crank Nicolson at t = 5.320s (Station B, growth of bottom vortex)

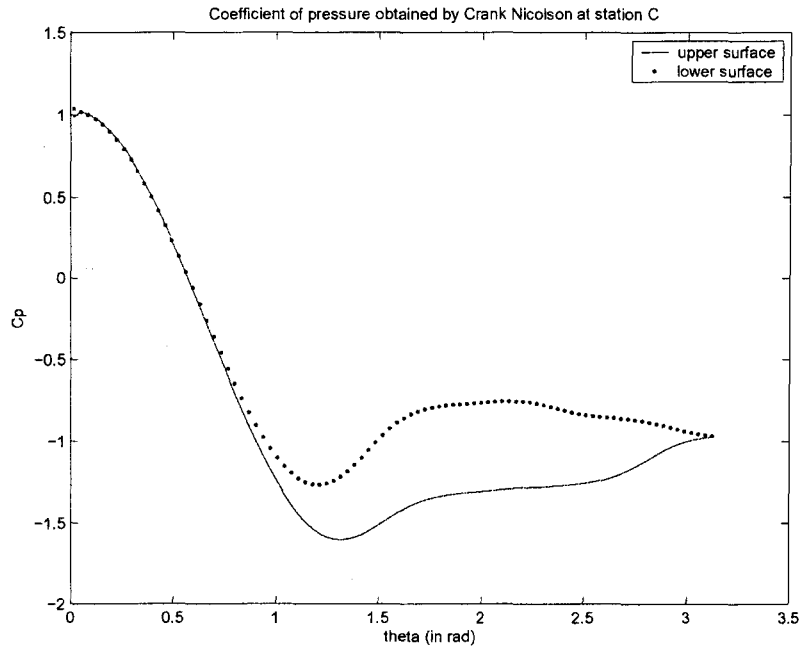

Figure 5.36 Coefficient of pressure obtained by Crank Nicolson at t = 5.346s (Station C, first minimum drag point)

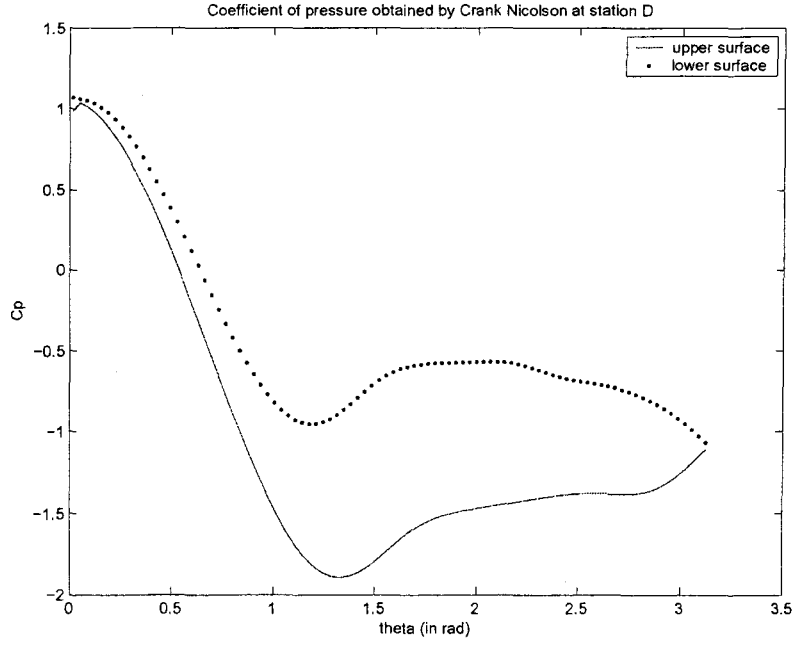

Figure 5.37 Coefficient of pressure obtained by Crank Nicolson at t = 5.373s (Station D, growth of bottom vortex)

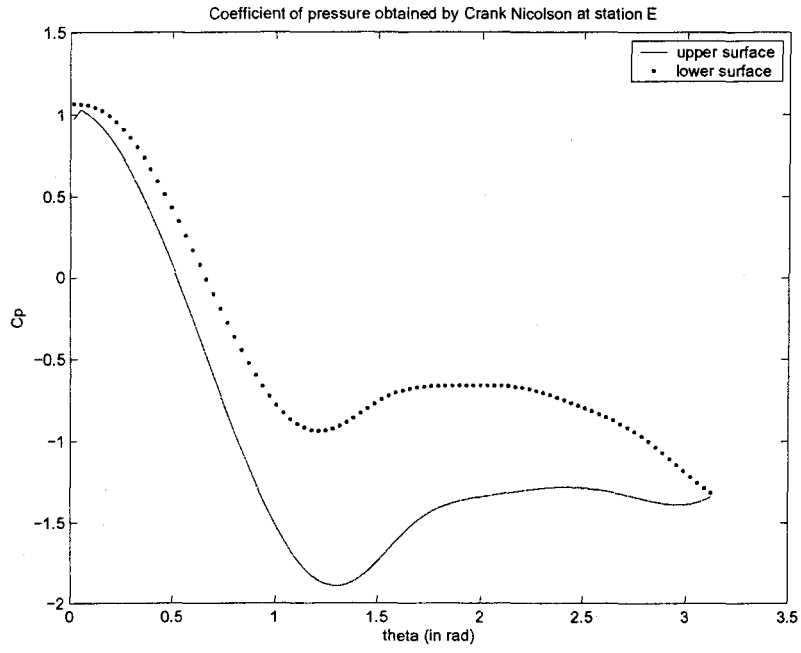

Figure 5.38 Coefficient of pressure obtained by Crank Nicolson at t = 5.401s (Station E, bottom shed)

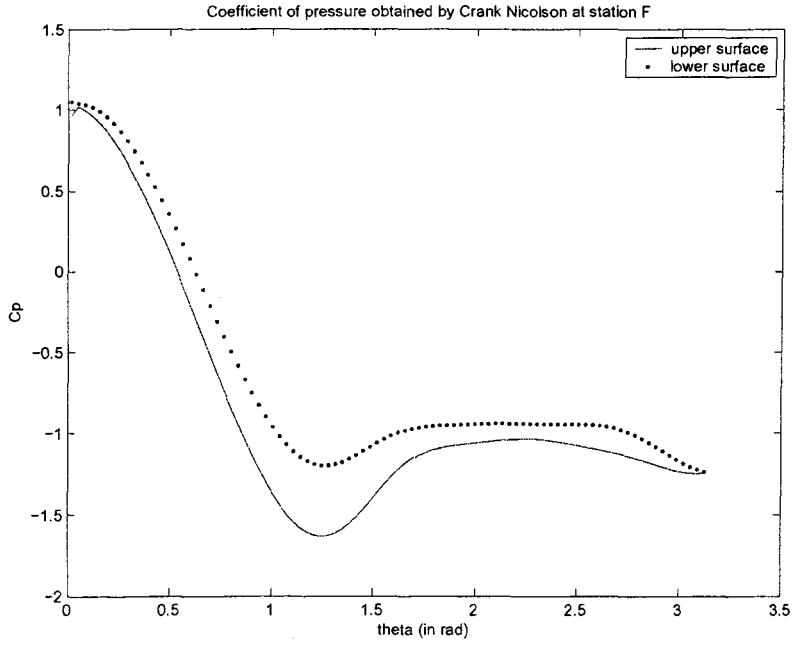

Figure 5.39 Coefficient of pressure obtained by Crank Nicolson at t = 5.428s (Station F, growth of top vortex)

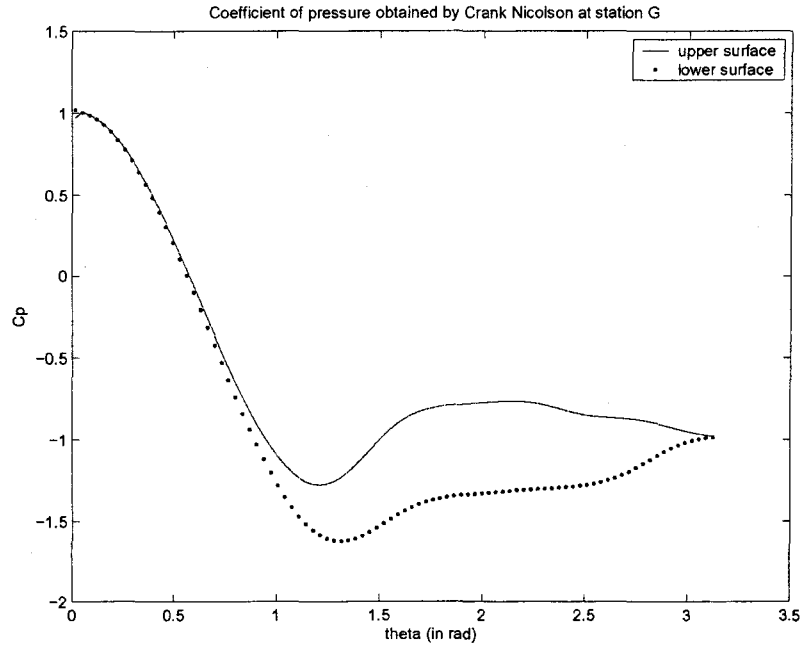

Figure 5.40 Coefficient of pressure obtained by Crank Nicolson at t = 5.455s (Station G,second minimum drag point)

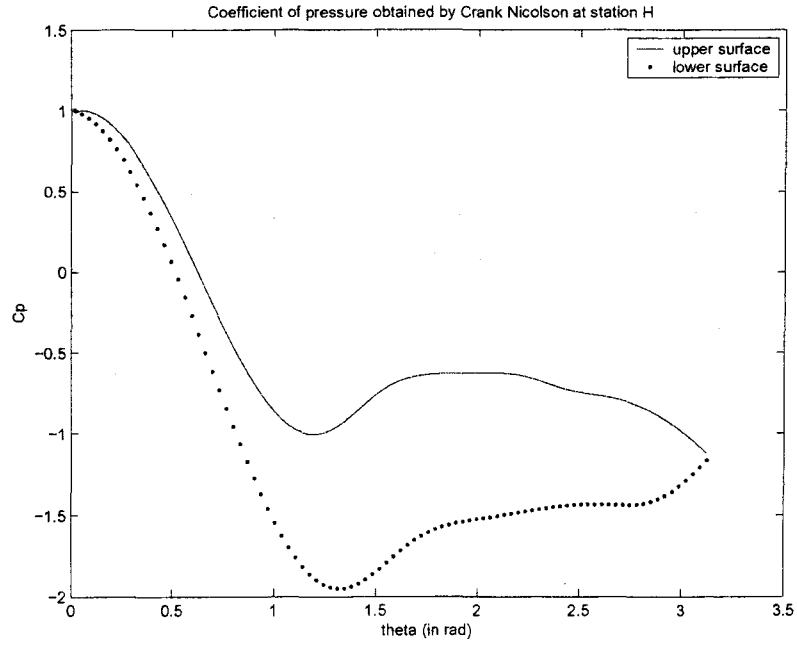

Figure 5.41 Coefficient of pressure obtained by Crank Nicolson at t = 5.482s (Station H, growth of top vortex)

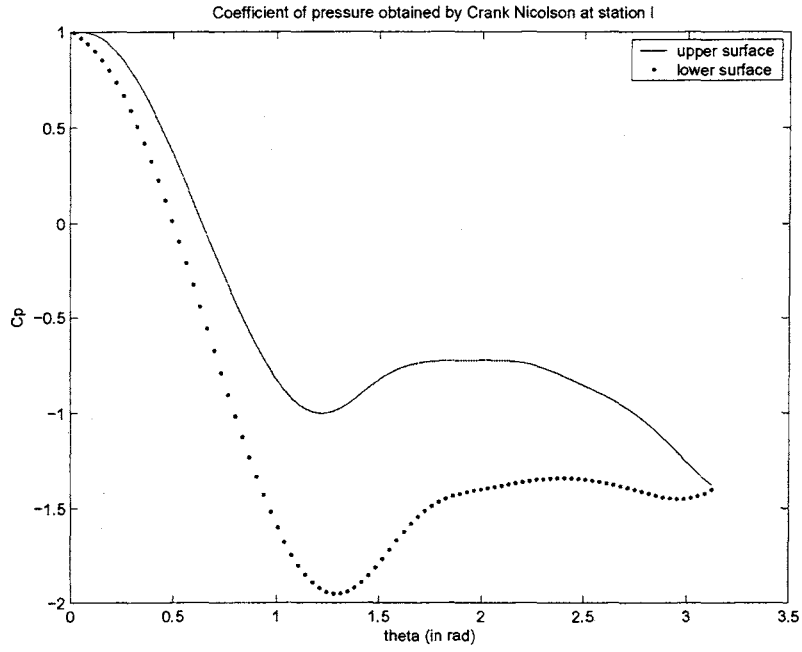

Figure 5.42 Coefficient of pressure obtained by Crank Nicolson at t = 5.510s (Station I, top shed)

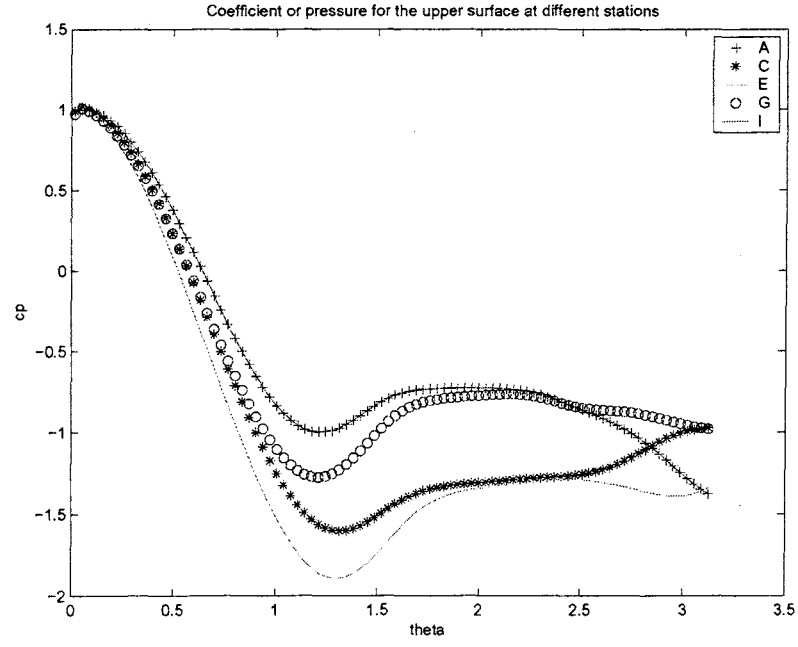

Figure 5.43 Coefficient of pressure at the upper surface of the cylinder at five stations

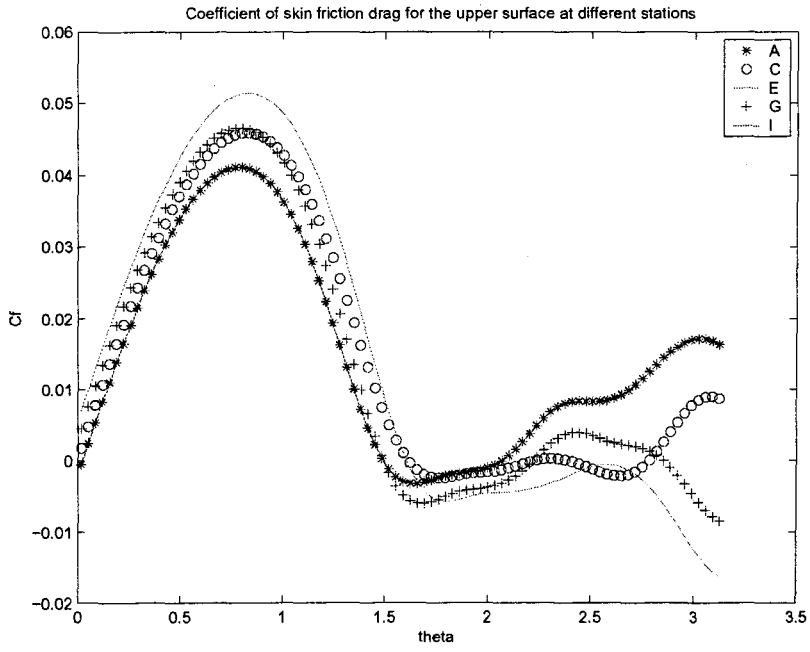

Figure 5.44 Coefficient of skin friction at the upper surface of the cylinder at five stations

It could be clearly seen that in the left part of the cylinder the C_p and C_f values did not change a whole lot. On the other hand, for the right side of the cylinder, it fluctuated a lot. That can be attributed to the fact that, in the right side of the cylinder, the flow is actually recirculatory in nature and hence unsteady effects were more visible there. The plots of C_p for lower and upper surfaces offer important observations. In a particular cycle, they actually interchange their relative positions. Again, this interchanging takes place predominantly in the right part of the cylinder. Figs. 5.45 through 5.53 show the streamline contours at different times.

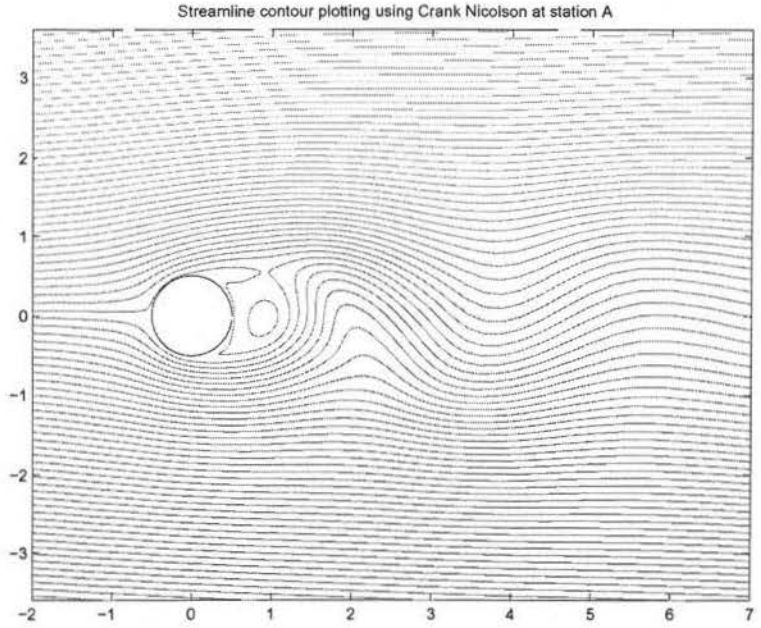

Figure 5.45 Streamline contours obtained by Crank Nicolson at t = 5.293s (Station A, top shed)

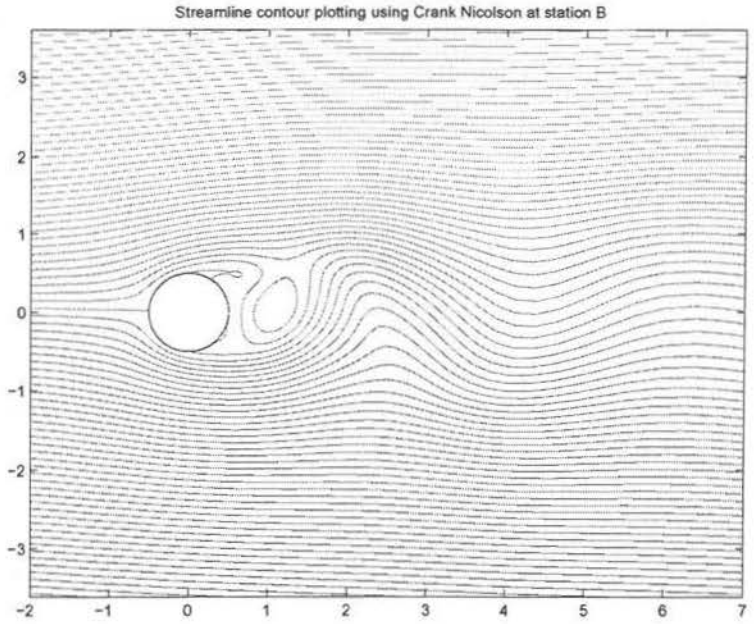

Figure 5.46 Streamline contours obtained by Crank Nicolson at t = 5.320s (Station B, growth of bottom vortex)

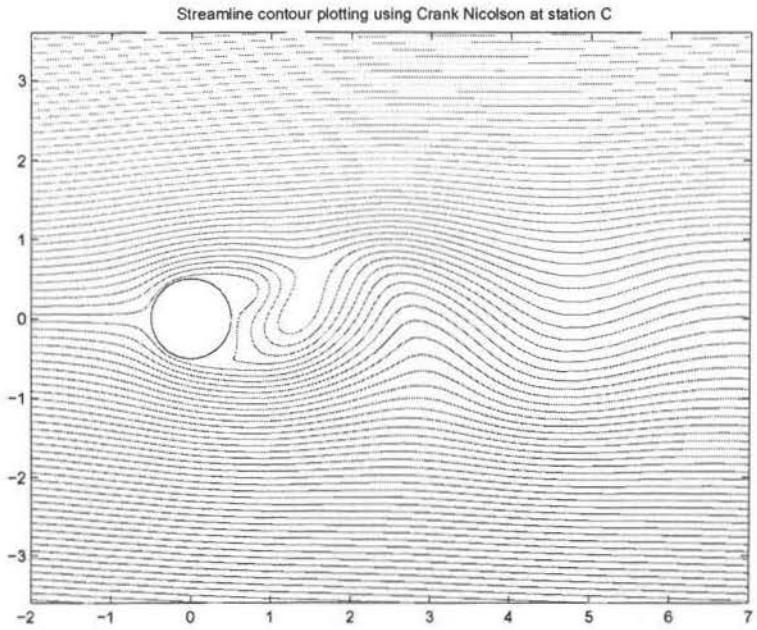

Figure 5.47 Streamline contours obtained by Crank Nicolson at t = 5.346s (Station C, first minimum drag point)

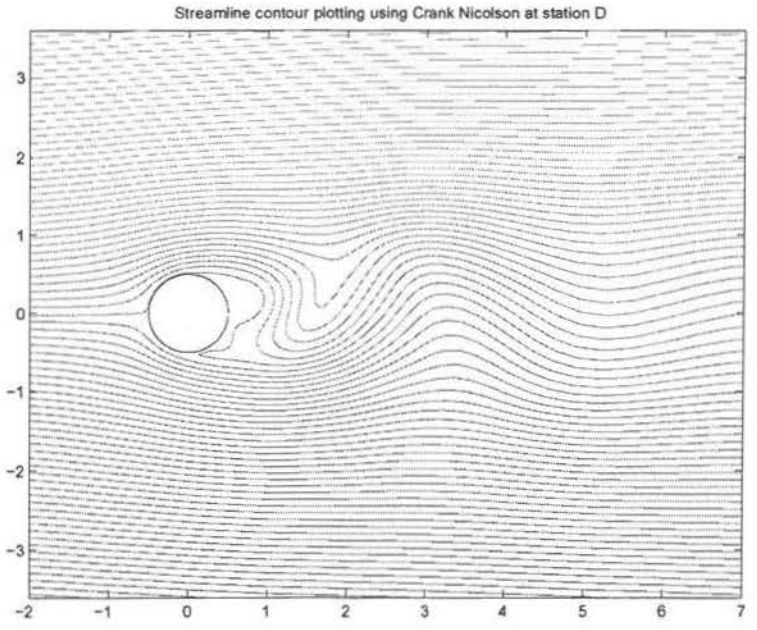

Figure 5.48 Streamline contours obtained by Crank Nicolson at t = 5.373s (Station D, growth of bottom vortex)

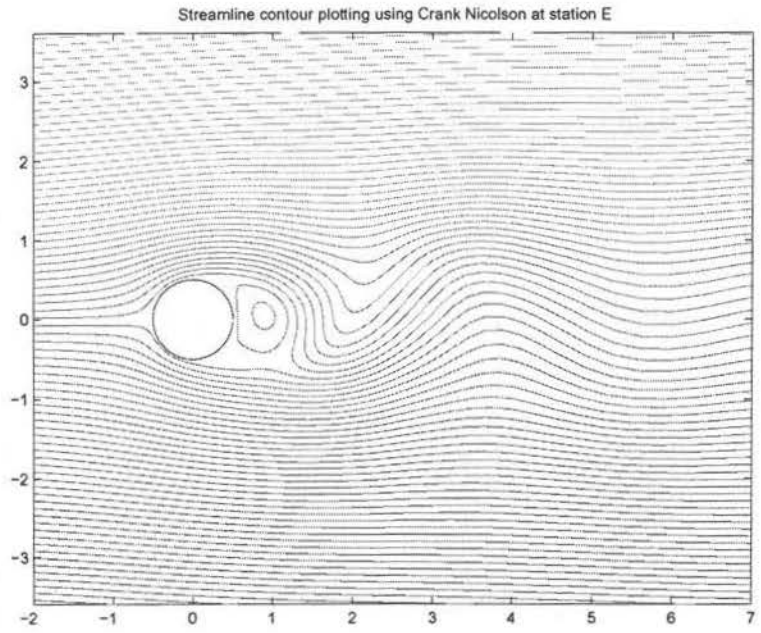

Figure 5.49 Streamline contours obtained by Crank Nicolson at t = 5.401s (Station E, bottom shed)

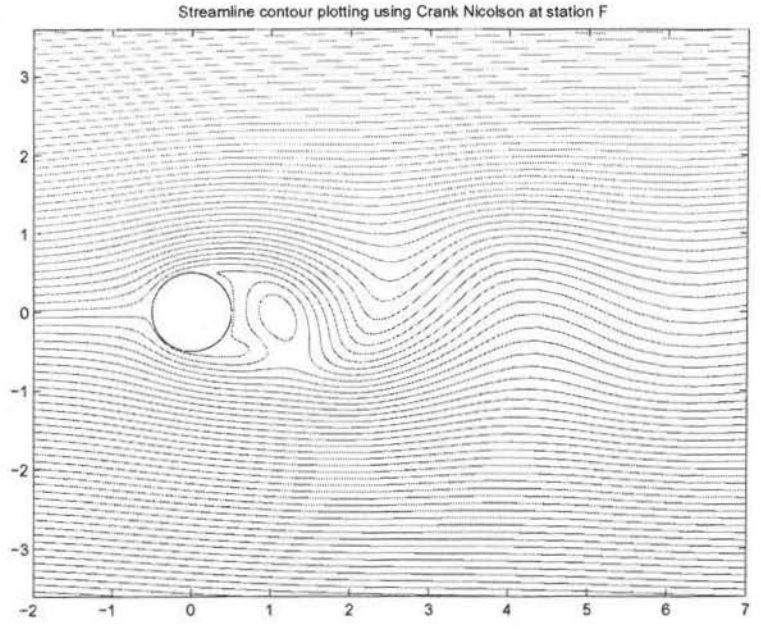

Figure 5.50 Streamline contours obtained by Crank Nicolson at t = 5.428s (Station F, growth of top vortex)

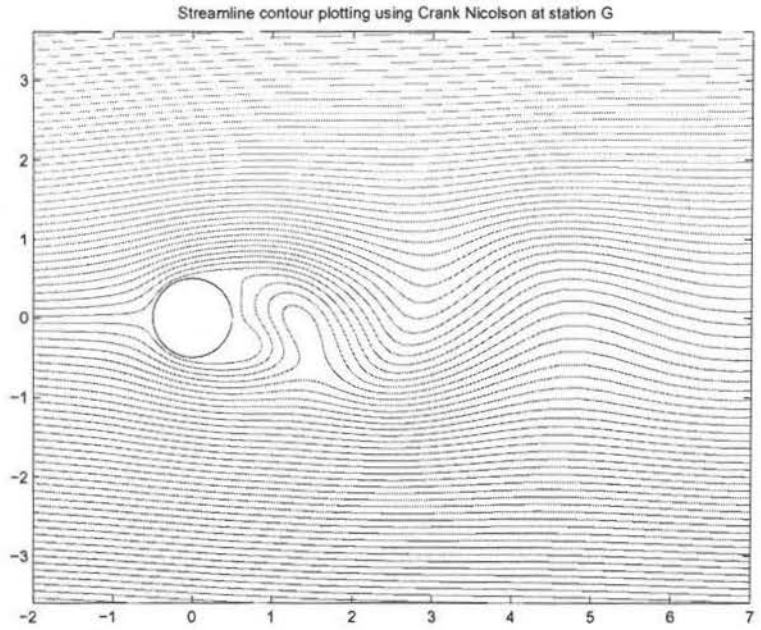

Figure 5.51 Streamline contours obtained by Crank Nicolson at t = 5.455s(Station G, second minimum drag point)

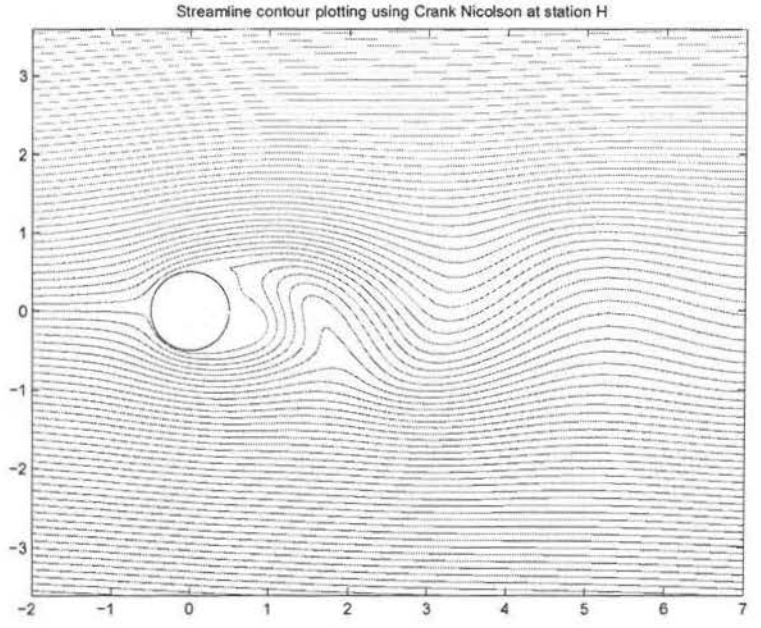

Figure 5.52 Streamline contours obtained by Crank Nicolson at t = 5.482s (Station H, growth of top vortex)

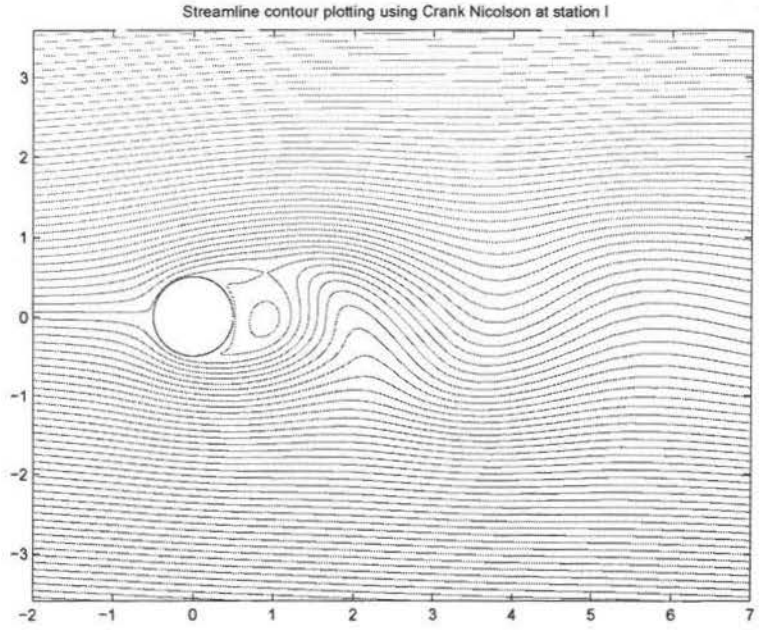

Figure 5.53 Streamline contours obtained by Crank Nicolson at t = 5.510s (Station I, top shed)

The top vortex shedding could be seen in Fig. 5.45. Then Figs.5.46 through 5.48 show the growth of bottom vortex. Fig. 5.47 is the first minimum drag point. Fig. 5.49 shows the bottom vortex shedding. Figs. 5.50 through 5.52 show the growth of the top vortex again, Fig. 5.47 being the second minimum drag point of that cycle. The cycle ends at Fig. 5.53, which shows top vortex shedding once again. The streamline contours serves the purpose of a visualization of a vortex shedding cycle as described above.

5.1.2 Fully Implicit Results

For Fully Implicit, the cycle chosen was such that it was from bottom vortex shedding to bottom vortex shedding capturing the top vortex shed in the process (Fig. 5.54).

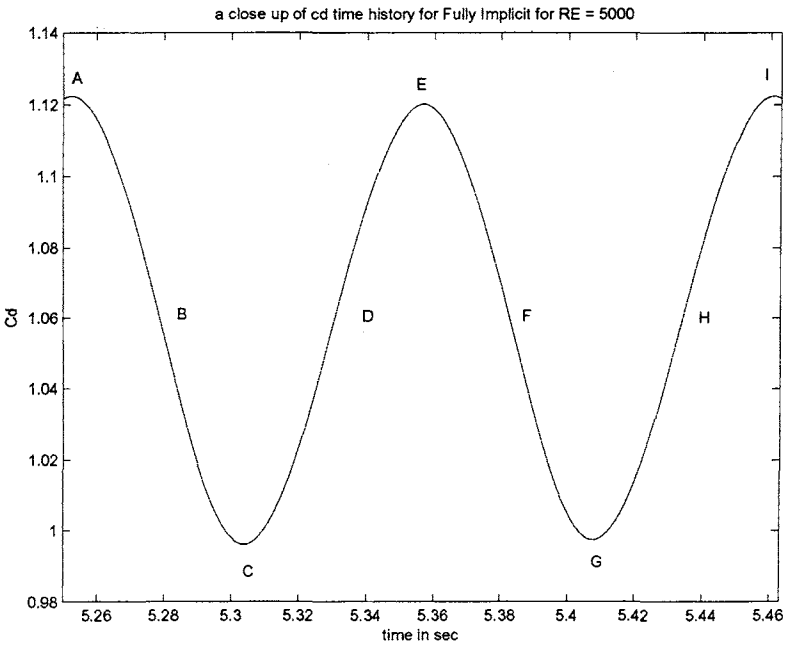

Figure 5.54 A closeup look at a bottom shed to bottom shed cycle using Fully Implicit

Fully Implicit results did not differ much from the Crank Nicolson results, and hence similar observations can be made. Since the results did not differ much, C_f, C_p and streamline contours will be shown at five stations, *i.e* A, C, E, G and I. Figs. 5.55 through 5.59 show the skin friction coefficient at five stations of a cycle. Figs. 5.60 through 5.64 show the coefficient of pressure plots. Figs. 5.65 through 5.69 show the streamline contours.

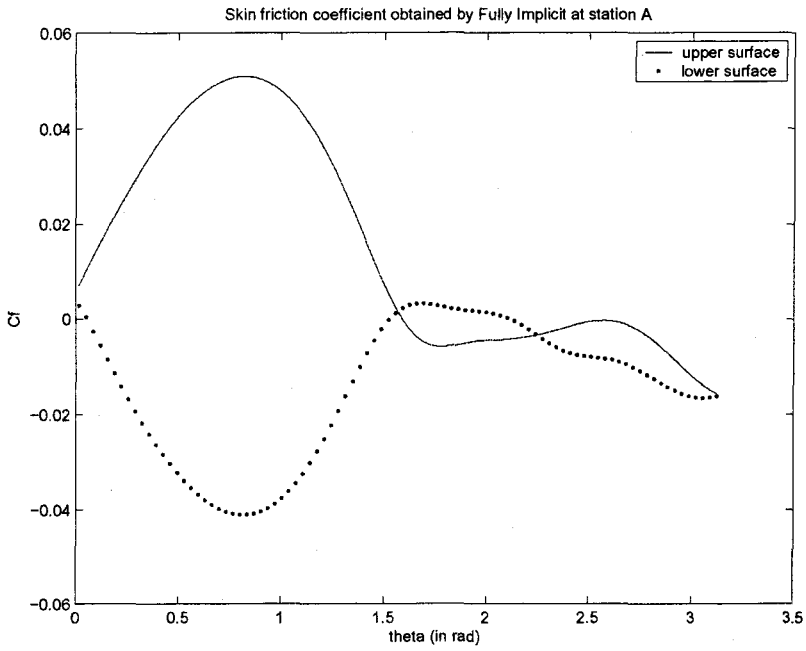

Figure 5.55 Skin friction coefficient obtained by Fully Implicit at t = 5.252s (Station A, bottom shed)

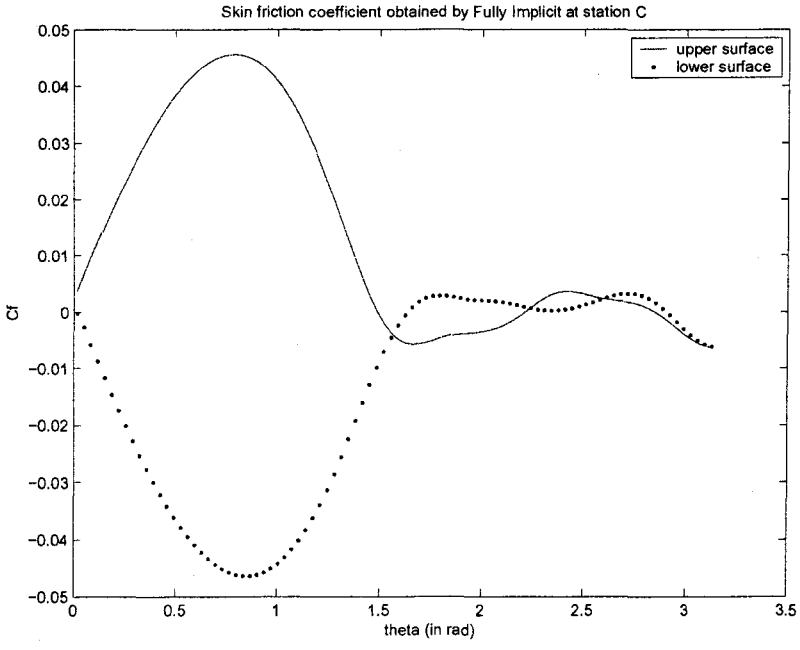

Figure 5.56 Skin friction coefficient obtained by Fully Implicit at t = 5.304s (Station C, first minimum drag point)

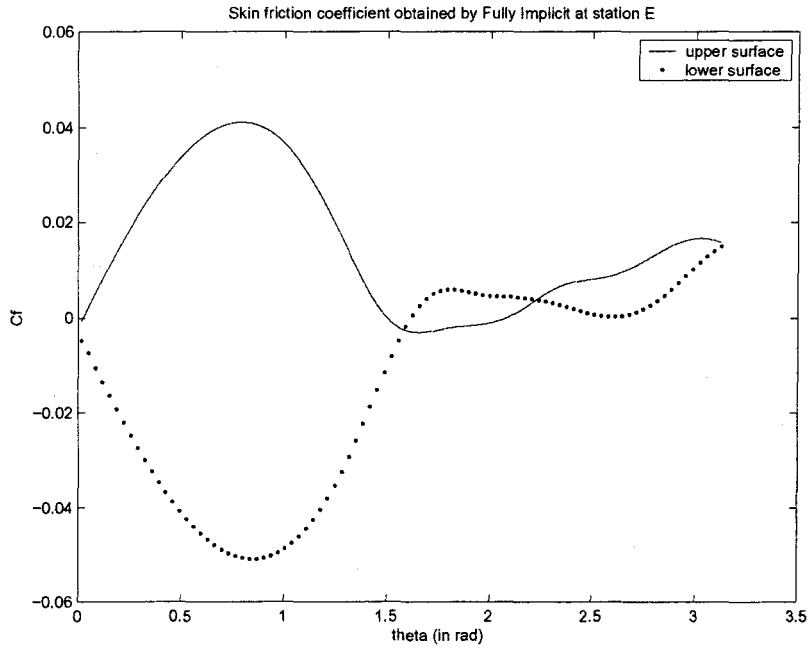

Figure 5.57 Skin friction coefficient obtained by Fully Implicit at t = 5.357s (Station E, top shed)

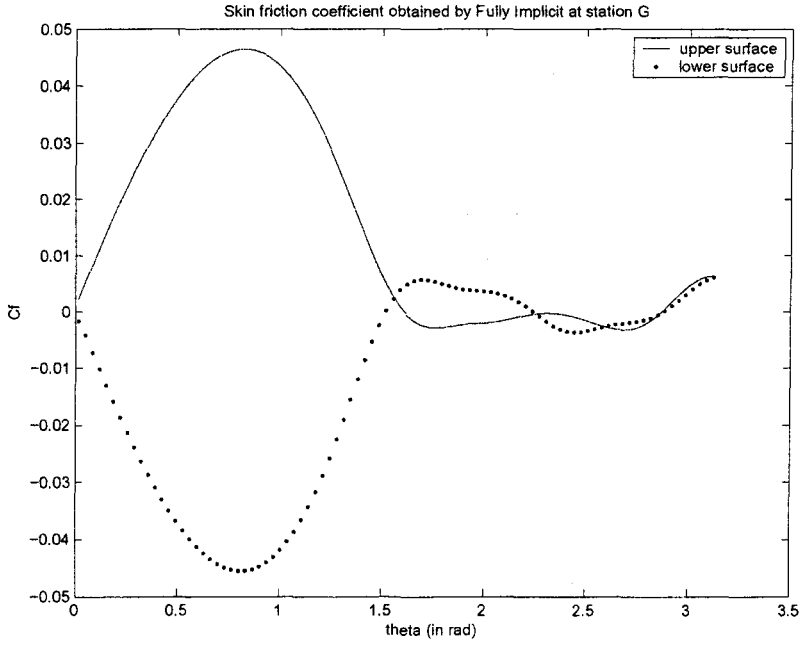

Figure 5.58 Skin friction coefficient obtained by Fully Implicit at t = 5.408s (Station G, second minimum drag point)

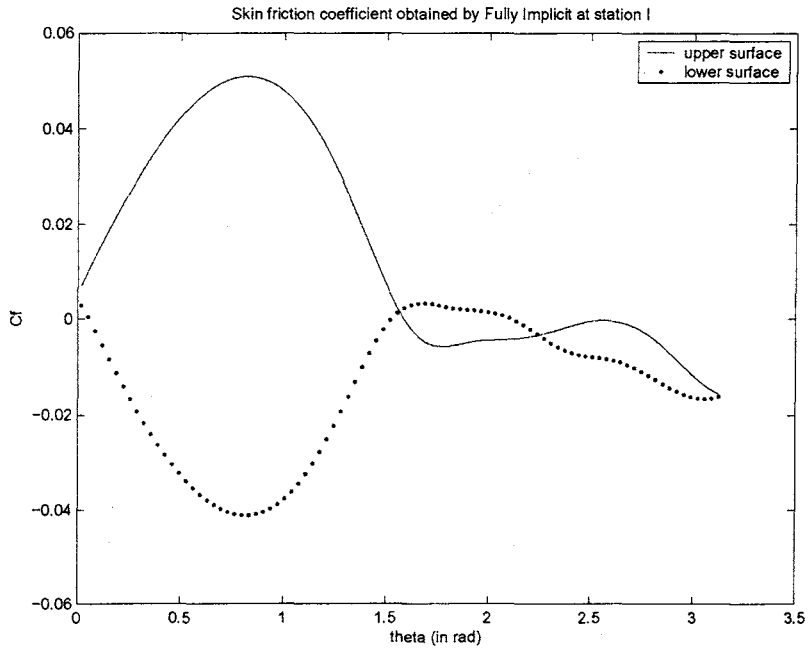

Figure 5.59 Skin friction coefficient obtained by Fully Implicit at t = 5.461s (Station I, bottom shed)

If the C_f values for the two different schmes are now compared, it could be seen that there is really not much of a difference in the two schemes. The overlapping of the two curves still holds true at the right side of the cylinder and the absolute value still interchanges for the two surfaces. The upper surface C_f value becomes negative for all the cases. However, at the bottom shed, the C_f value for the upper surface reaches the lowest. Next, the C_p values will be plotted at five different stations.

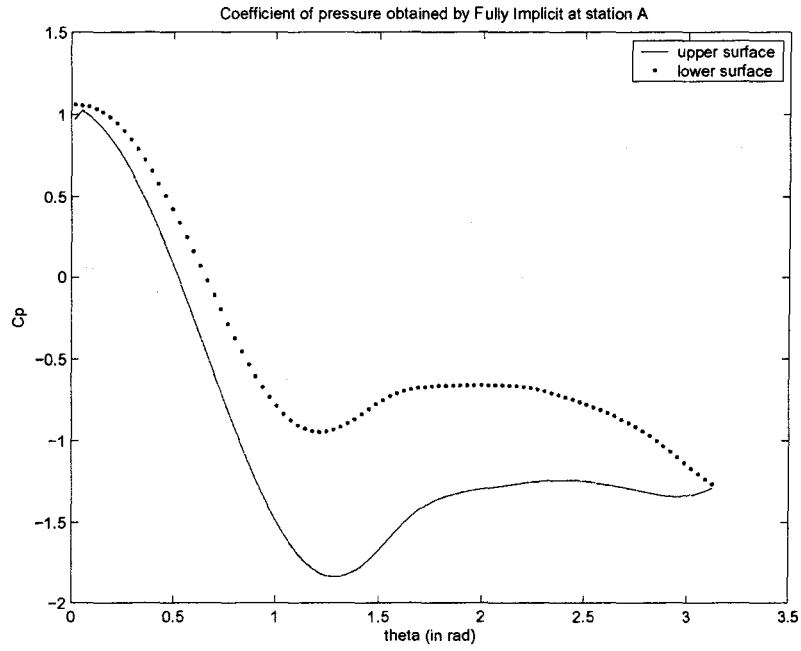

Figure 5.60 Coefficient of pressure obtained by Fully Implicit at t = 5.252s (Station A, bottom shed)

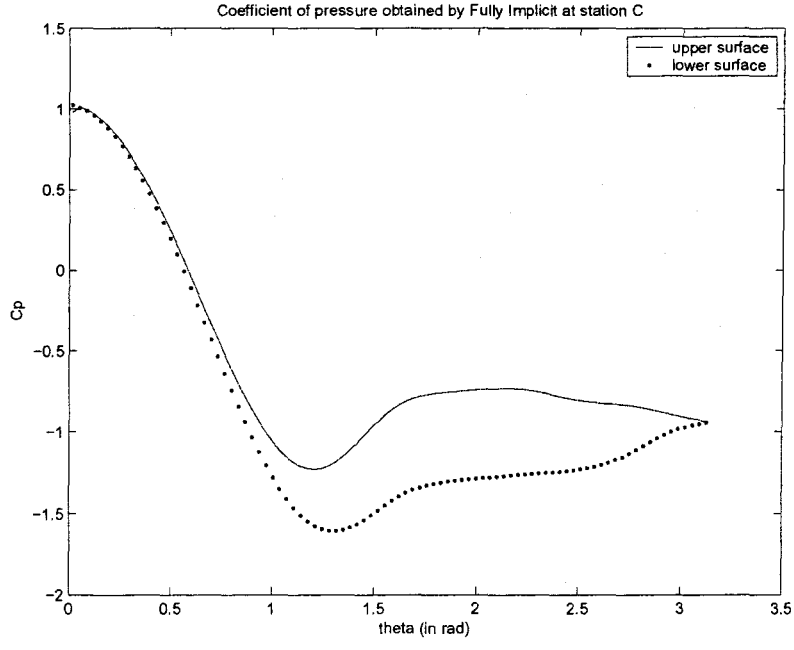

Figure 5.61 Coefficient of pressure obtained by Fully Implicit at t = 5.304s (Station C, first minimum drag point)

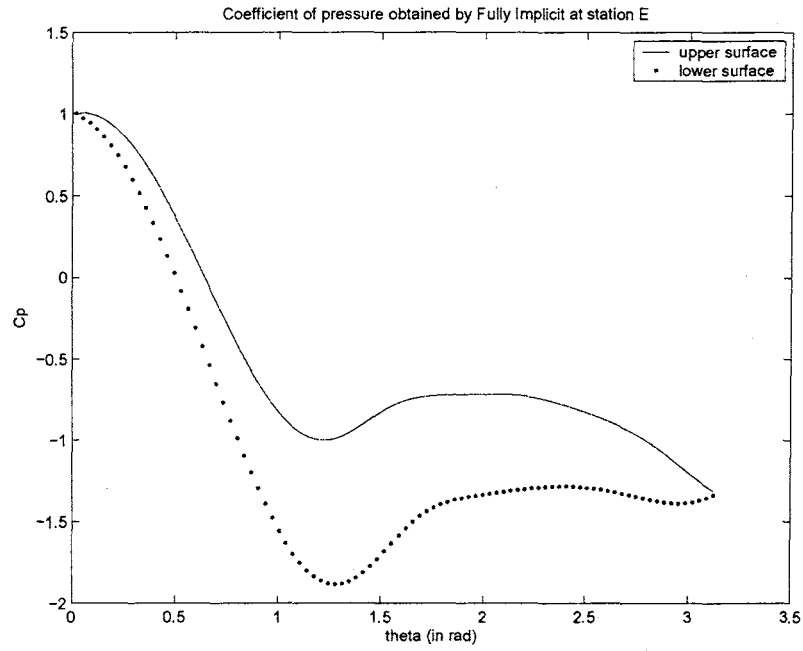

Figure 5.62 Coefficient of pressure obtained by Fully Implicit at t = 5.357s (Station E, top shed)

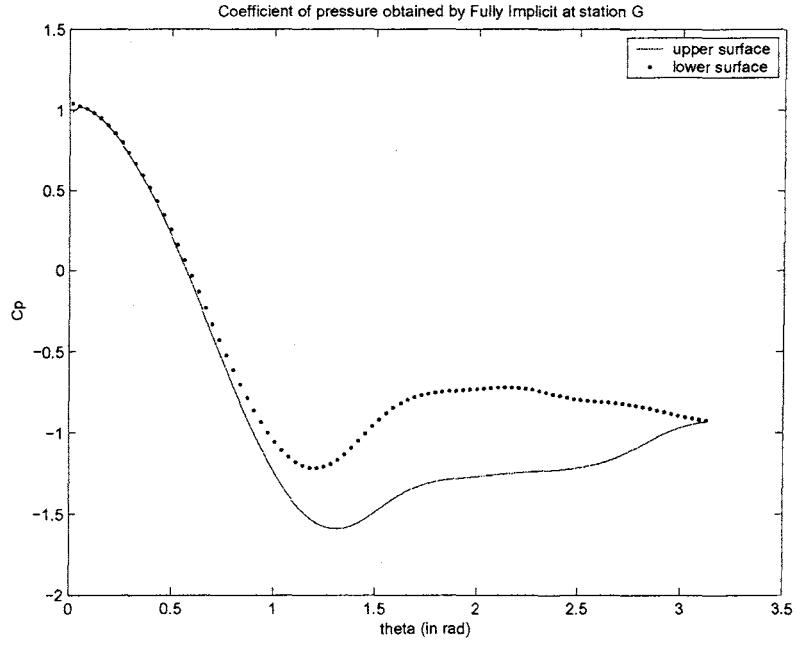

Figure 5.63 Coefficient of pressure obtained by Fully Implicit at t = 5.408s (Station G, second minimum drag point)

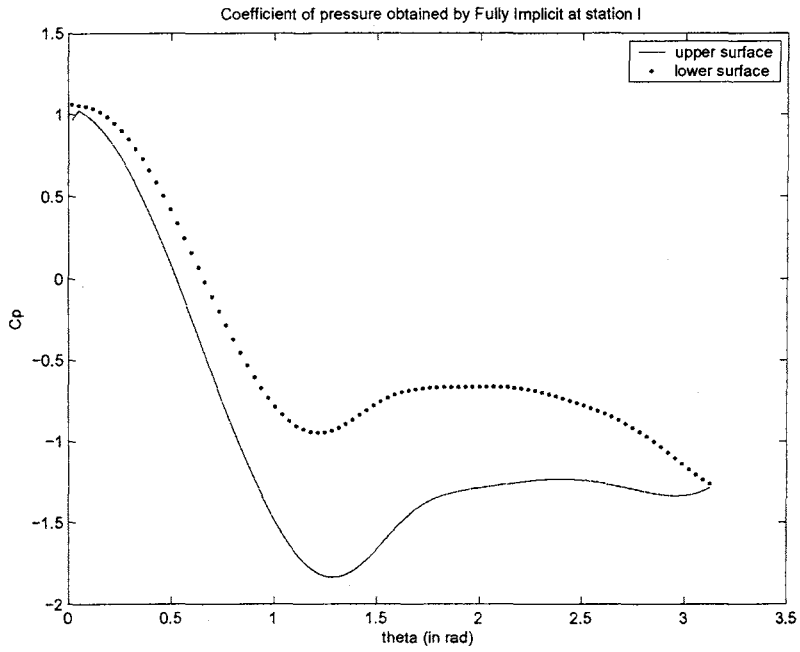

Figure 5.64 Coefficient of pressure obtained by Fully Implicit at t = 5.461s (Station I, bottom shed)

If the C_p plots are compared for the two schemes, the values are not much different. The lowest C_p value, however, for Crank Nicolson is a little less compared to the Fully Implicit. The other observations that were made for the Crank Nicolson still hold good for Fully Implicit. Next, the streamline contours will be plotted for the same cycle.

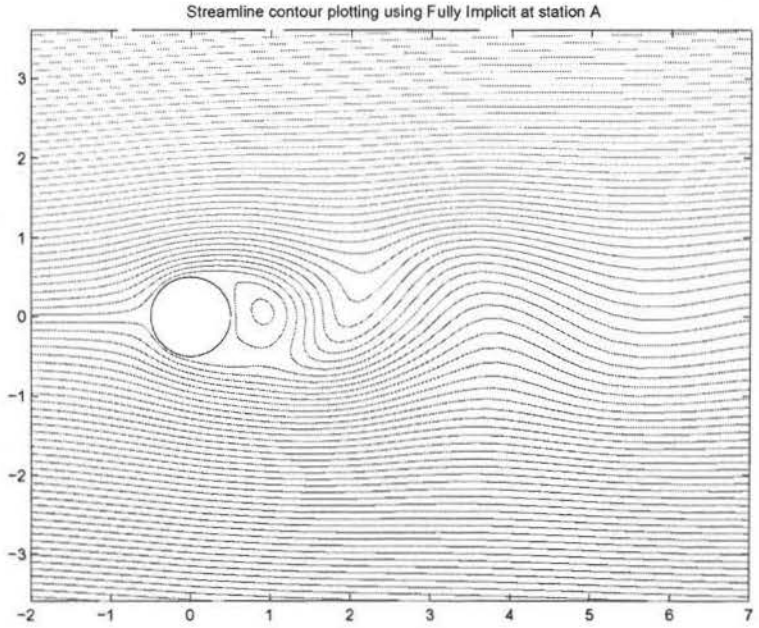

Figure 5.65 Streamline contours obtained by Fully Implicit at t = 5.252s (Station A, bottom shed)

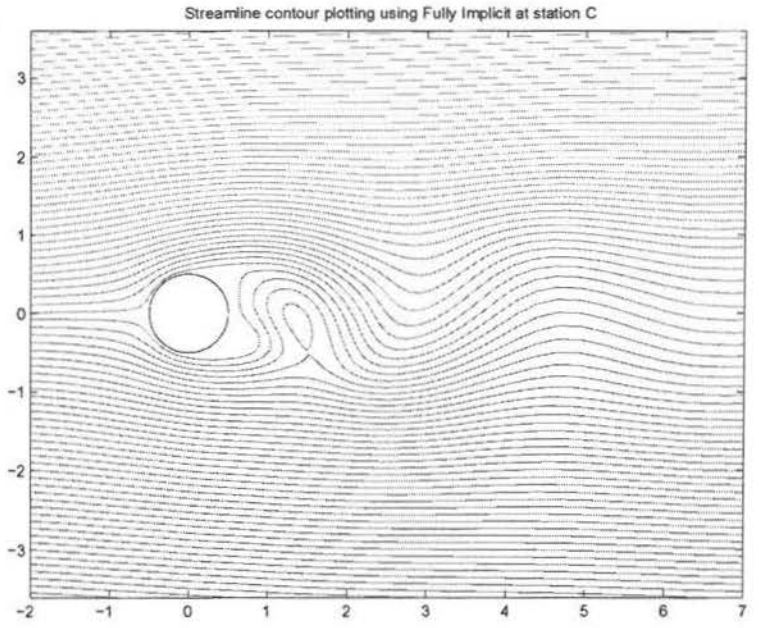

Figure 5.66 Streamline contours obtained by Fully Implicit at t = 5.304s (Station C, first minimum drag point)

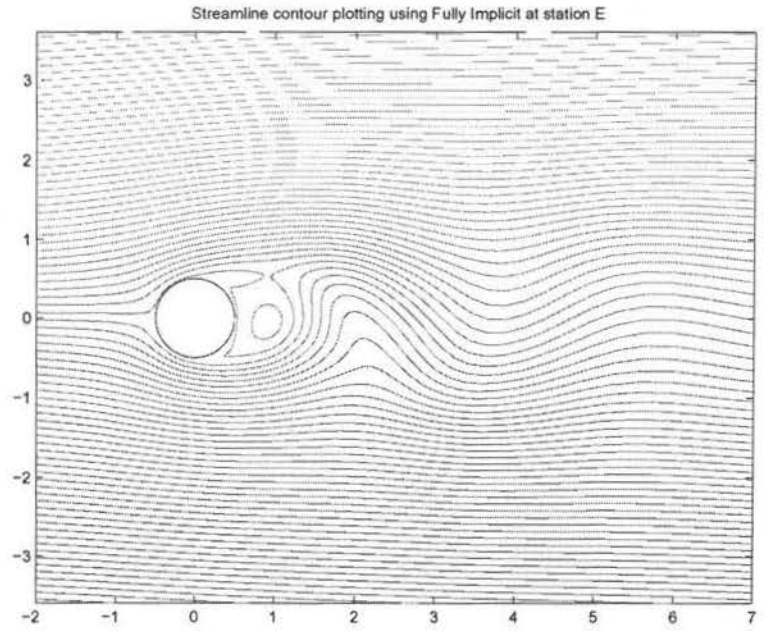

Figure 5.67 Streamline contours obtained by Fully Implicit at t = 5.357s (Station E, top shed)

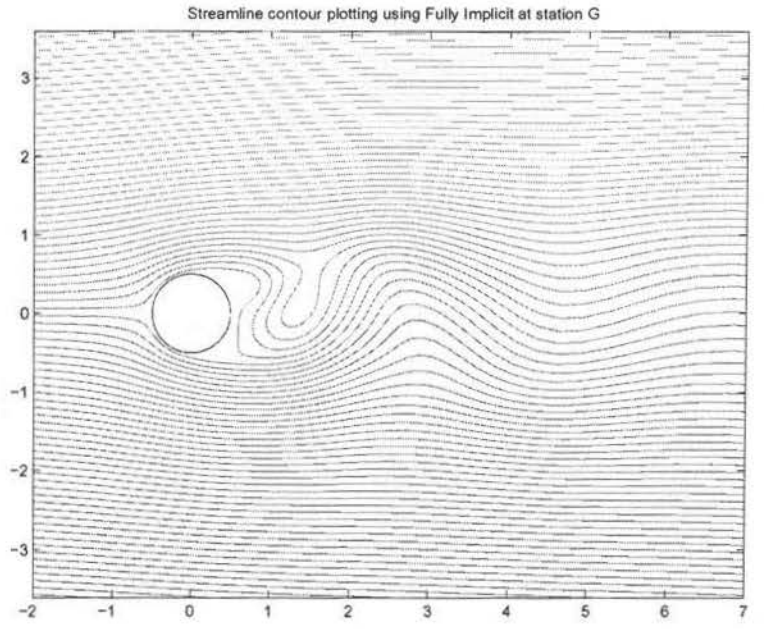

Figure 5.68 Streamline contours obtained by Fully Implicit at t = 5.408s (Station G, second minimum drag point)

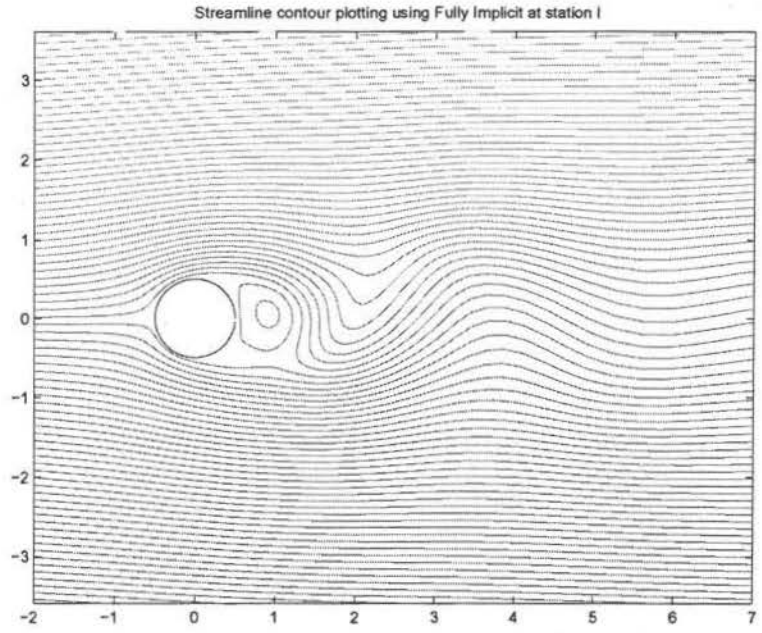

Figure 5.69 Streamline contours obtained by Fully Implicit at t = 5.461s (Station I, bottom shed)

It was observed before that C_f and C_p values show signs of symmetry in the behavior of the flow. It is easily visualized in the streamline contours. If Figs. 5.66 and 5.68 are looked at closely, they clearly show the symmetric nature of the flow. Similarly, the symmetry could be observed for Figs. 5.65 and 5.67. The symmetric nature of the flow comes due to the fact that the cylinder is a symmetric body.

5.2 Elliptic Cylinder

In this section, a few cases of ellipse of different aspect ratios will be considered. Of course, circular cylinder case is of aspect ratio 1.00. Reynolds number 4000 is considered, and the change in the drag coefficient value is studied as the aspect ratio is changed. Also, as done in the previous case of the circular cylinder, a thorough study of how coefficient of pressure and coefficient of skin friction varies is shown for nine significant times of a particular cycle for the case of $Re = 4000$ and aspect ratio 1.25. Also, to visualize the shedding, streamline contours are plotted. Fig. 5.73 shows how the coefficient of drag value varies for different aspect ratios. It should be mentioned here that for all the cases, the Reynolds numbers were calculated based on the larger of the two semi axes.

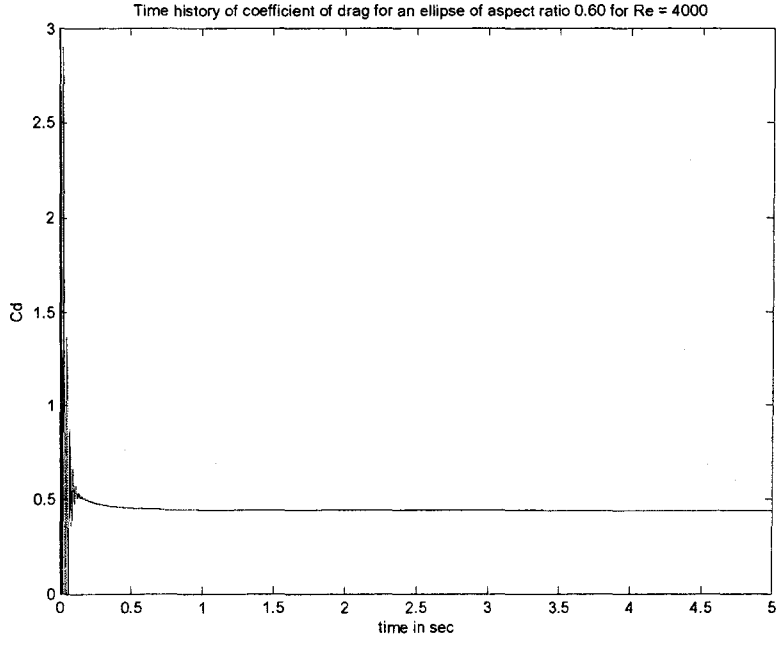

Figure 5.70 Time history of coefficient of drag for an ellipse of aspect ratio 0.60 and Re = 4000

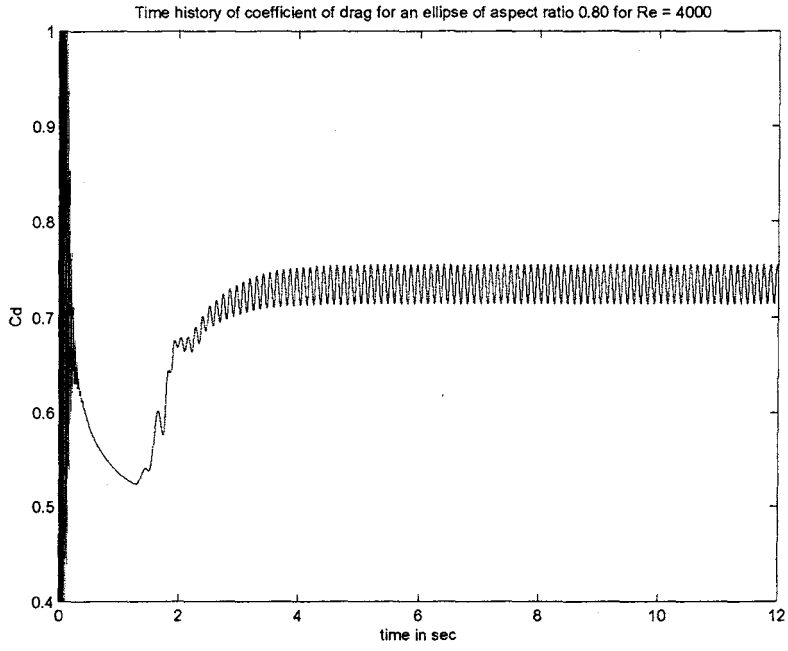

Figure 5.71 Time history of coefficient of drag for an ellipse of aspect ratio 0.80 and Re = 4000

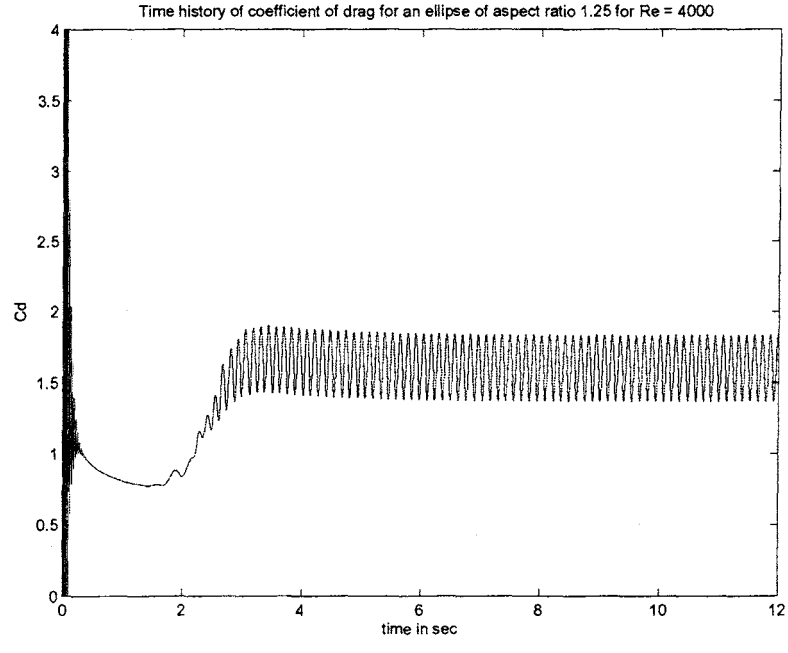

Figure 5.72 Time history of coefficient of drag for an ellipse of aspect ratio 1.25 and Re = 4000

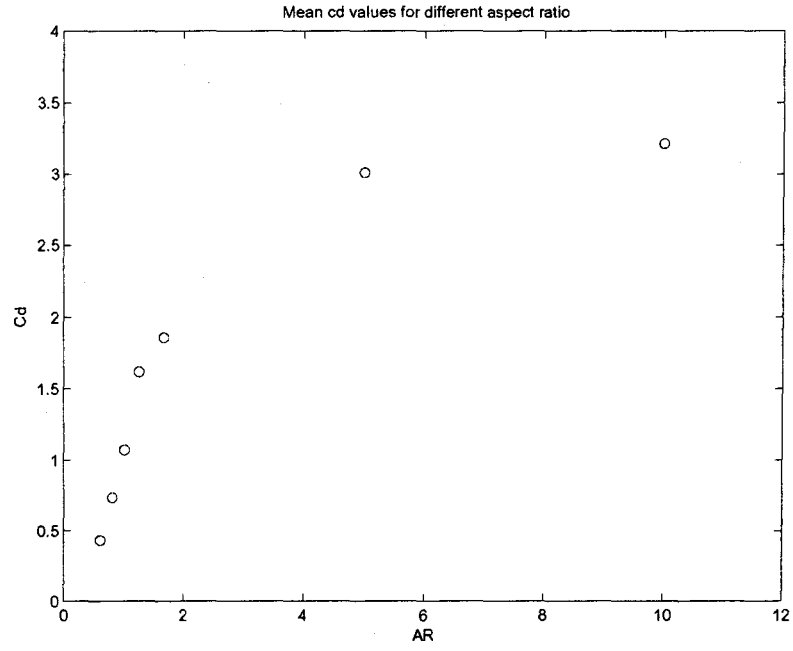

Figure 5.73 A study of mean cd values for different aspect ratio for Re = 4000

Fig. 5.71 suggests that there are oscillations in an ellipse with aspect ratios less than 1.00 as well. When the aspect ratio is decreased, the oscillation subsides, as shown in Fig. 5.70. Still some oscillations were found in the case of the aspect ratio 0.60. However, the oscillations were extremely small for any importance.

Figs. 5.75 through 5.83 show the skin friction coefficient at nine stations of a cycle. Figs. 5.84 through 5.92 show the coefficient of pressure plots. Figs. 5.93 through 5.101 show the streamline contours. It should be noted here that for finding the mean C_d's for different aspect ratios, the 370X101 grid was used. However, the 186X101 grid was preferred to show the variations of C_p, C_f and streamline contours with time.

C_d value increased with the aspect ratio, as suggested by Fig. 5.73. That can be attributed to the fact that as the aspect ratio increases, the body becomes more and more "bluff body natured" and hence the drag increases.

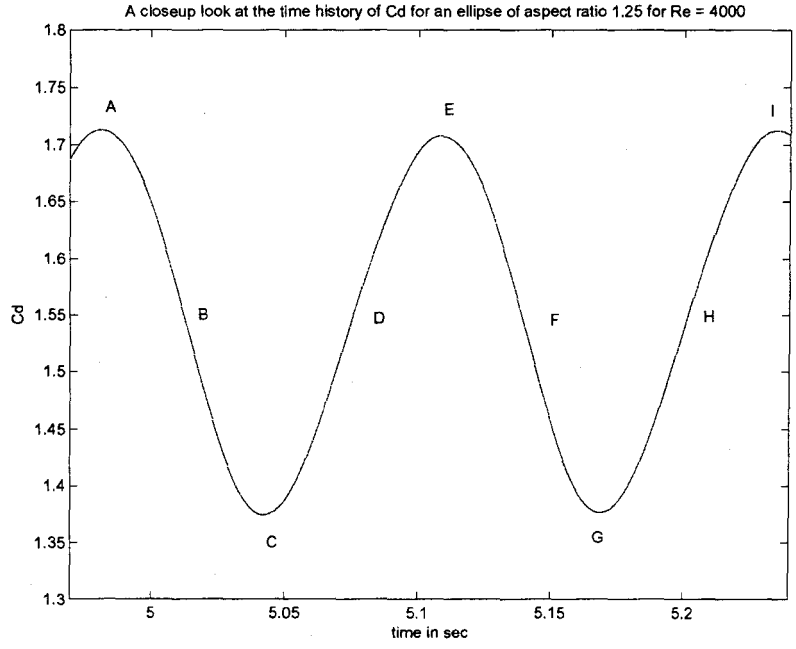

Figure 5.74 Closeup of a cycle of the time history of coefficient of drag for an ellipse of aspect ratio 1.25 and Re = 4000

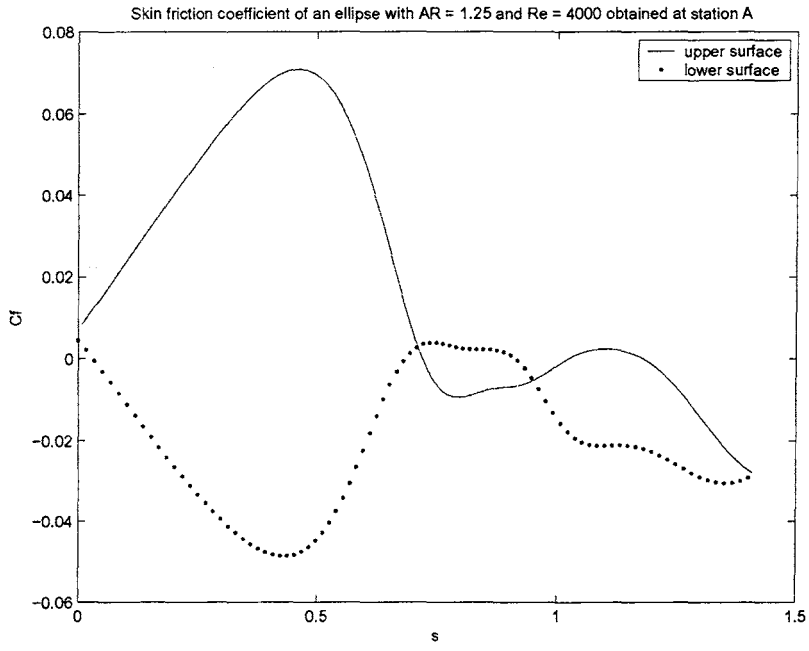

Figure 5.75 Skin friction coefficient for upper and lower surface for an ellipse of AR = 1.25 at t = 4.981s (Station A, bottom shed)

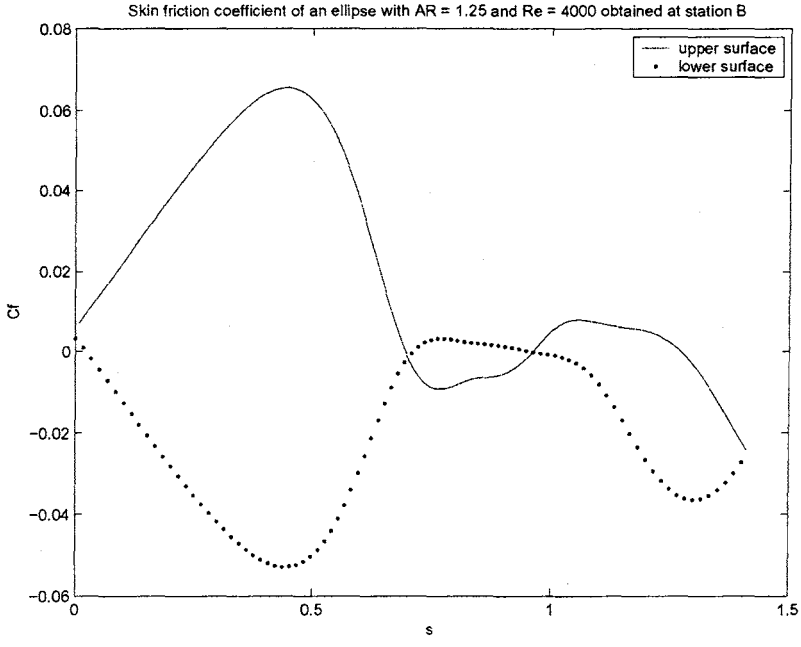

Figure 5.76 Skin friction coefficient for upper and lower surface for an ellipse of AR = 1.25 at t = 5.012s (Station B, growth of top vortex)

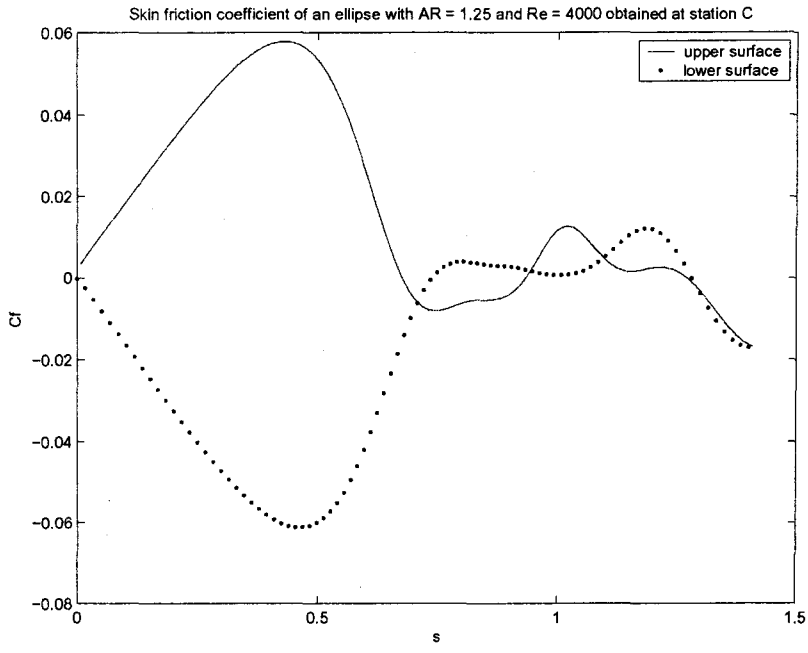

Figure 5.77 Skin friction coefficient for upper and lower surface for an ellipse of AR = 1.25 at t = 5.042s (Station C, first minimum drag point)

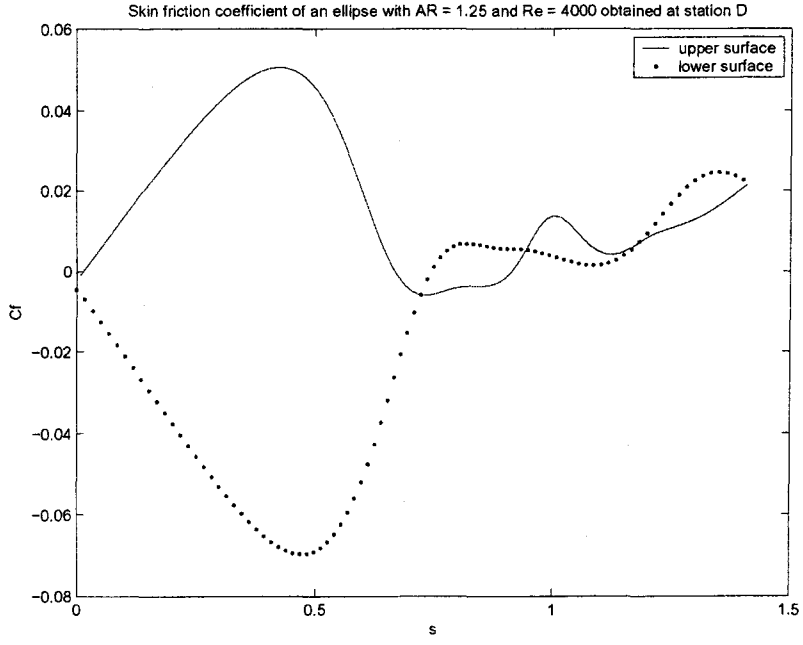

Figure 5.78 Skin friction coefficient for upper and lower surface for an ellipse of AR = 1.25 at t = 5.075s (Station D, growth of top vortex)

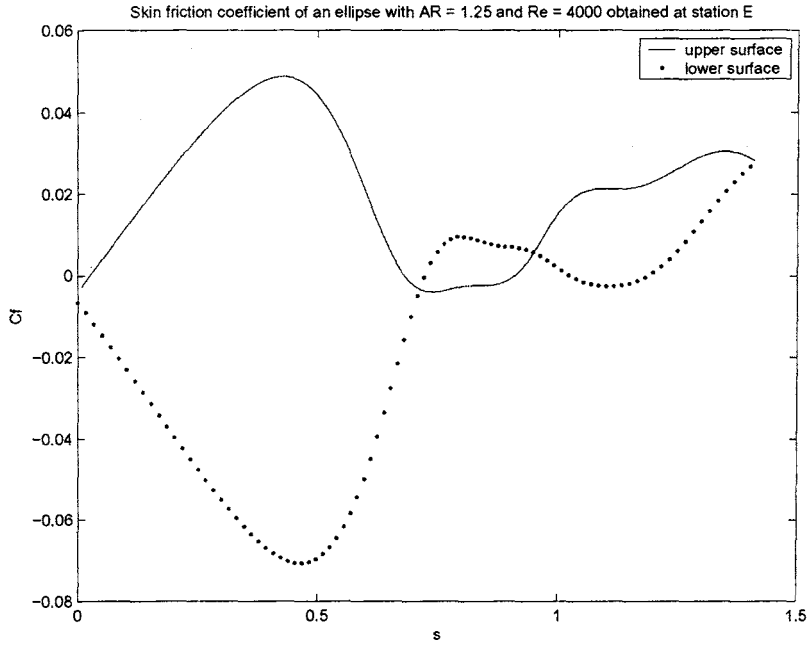

Figure 5.79 Skin friction coefficient for upper and lower surface for an ellipse of AR = 1.25 at t = 5.108s (Station E, top shed)

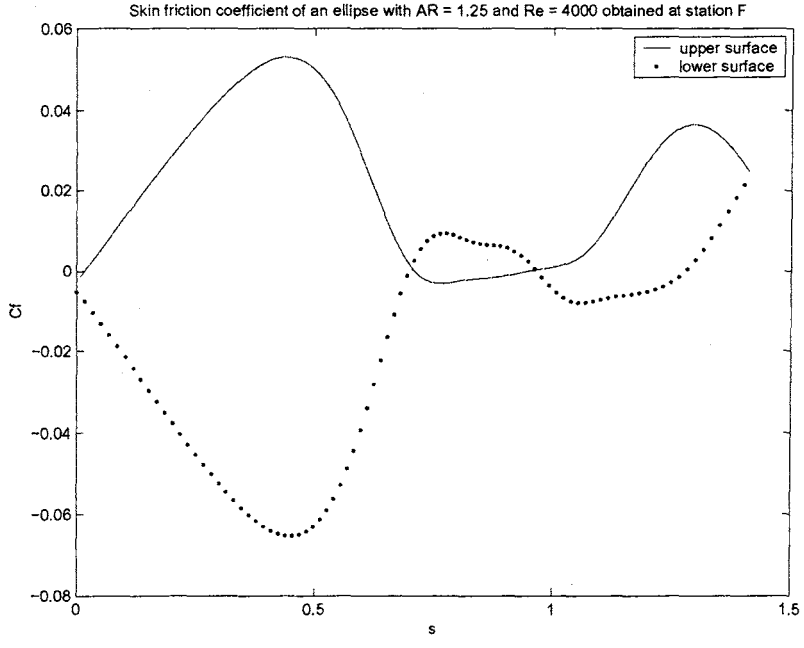

Figure 5.80 Skin friction coefficient for upper and lower surface for an ellipse of AR = 1.25 at t = 5.139s (Station F, growth of bottom vortex)

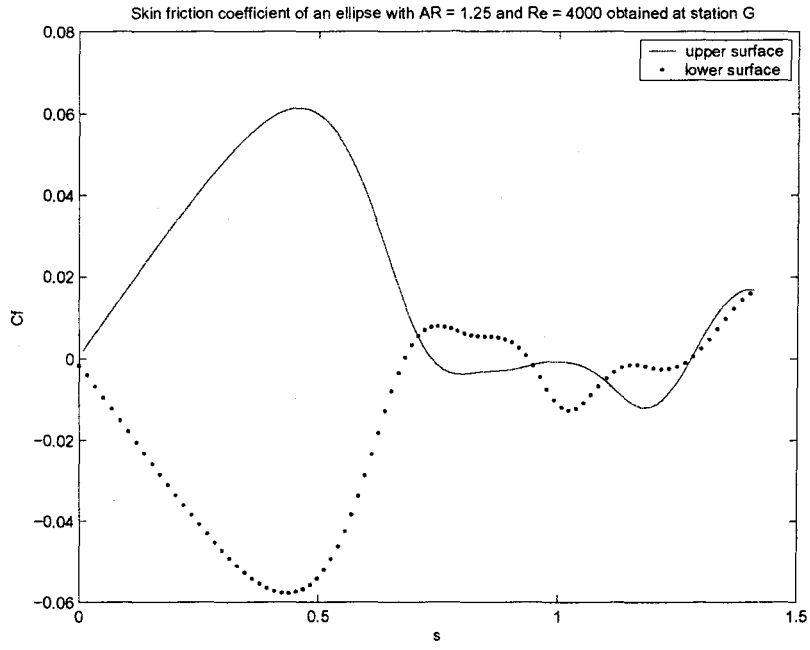

Figure 5.81 Skin friction coefficient for upper and lower surface for an ellipse of AR = 1.25 at t = 5.169s (Station G, second minimum drag point)

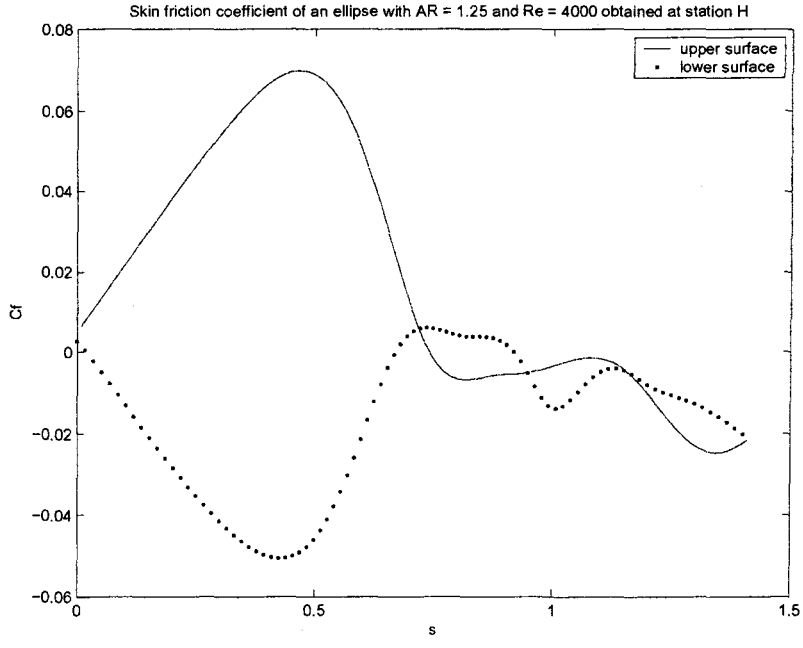

Figure 5.82 Skin friction coefficient for upper and lower surface for an ellipse of AR = 1.25 at t = 5.202s (Station H, growth of bottom vortex)

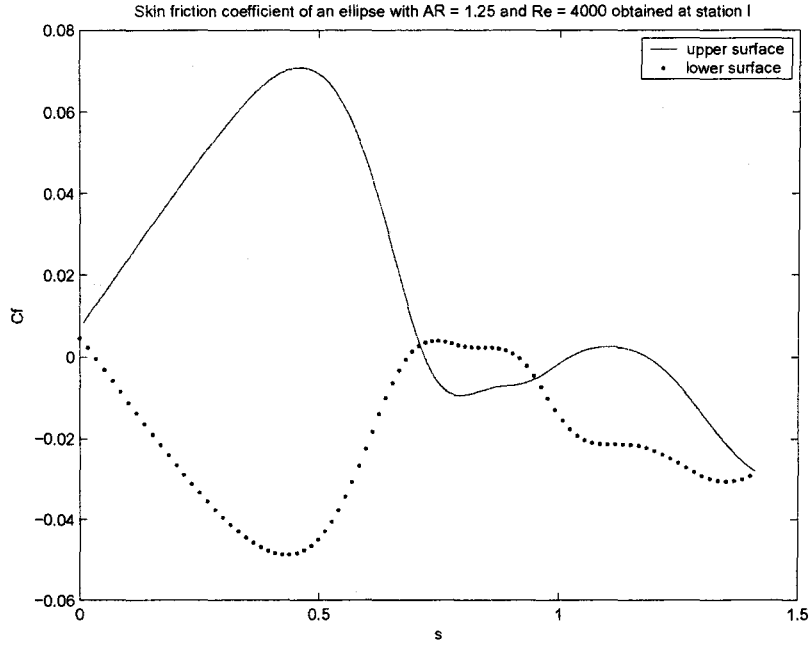

Figure 5.83 Skin friction coefficient for upper and lower surface for an ellipse of AR = 1.25 at t = 5.235s (Station I, bottom shed)

The above nine C_f plots show that for an ellipse with aspect ratio higher than one, the overlapping of the top and bottom surface curves are much more compared to that of a circular cylinder. The highest value for the top surface C_f reaches much more than 0.06. When compared to the highest value of the circular cylinder case, it never reaches 0.06. Also, it could be seen that the variations were much more pronounced in the right half of C_f curves compared to the left half. All the overlappings took place in the right half. That is due to the fact that the right half is basically the recirculating zone and the flow is more or less smooth in the left half of the ellipse. The C_p variation with time in a bottom shed to bottom shed cycle as will be shown next.

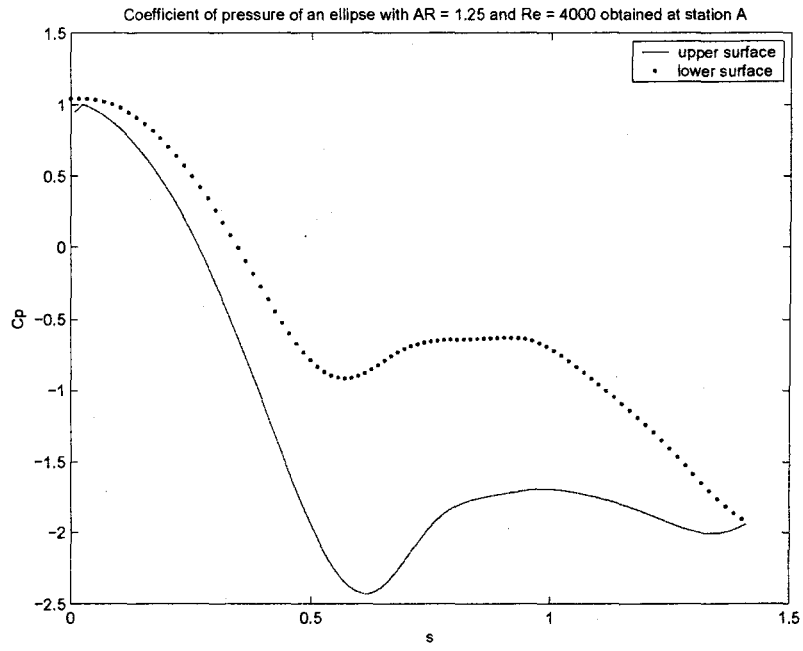

Figure 5.84 Coefficient of pressure for upper and lower surface for an ellipse of AR = 1.25 at t = 4.981s (Station A, bottom shed)

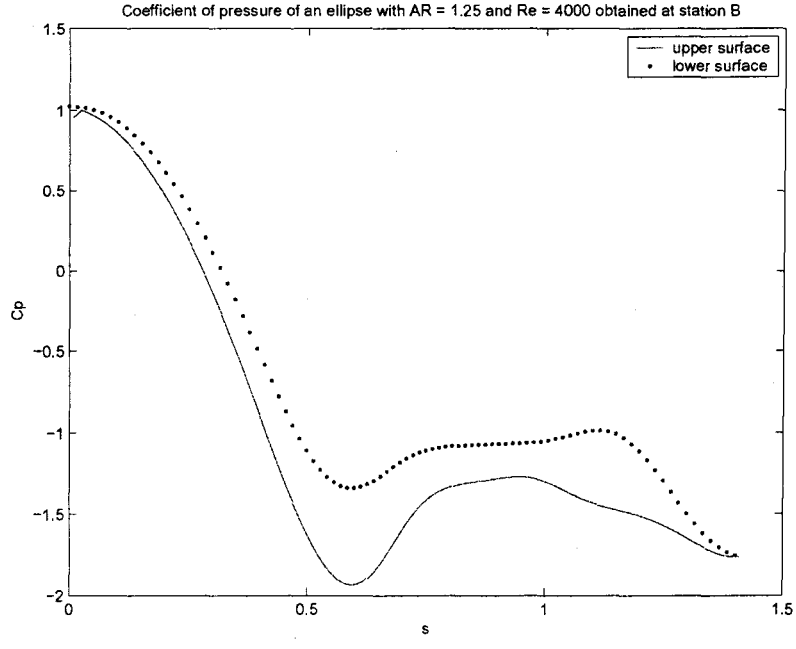

Figure 5.85 Coefficient of pressure for upper and lower surface for an ellipse of AR = 1.25 at t = 5.012s (Station B, growth of top vortex)

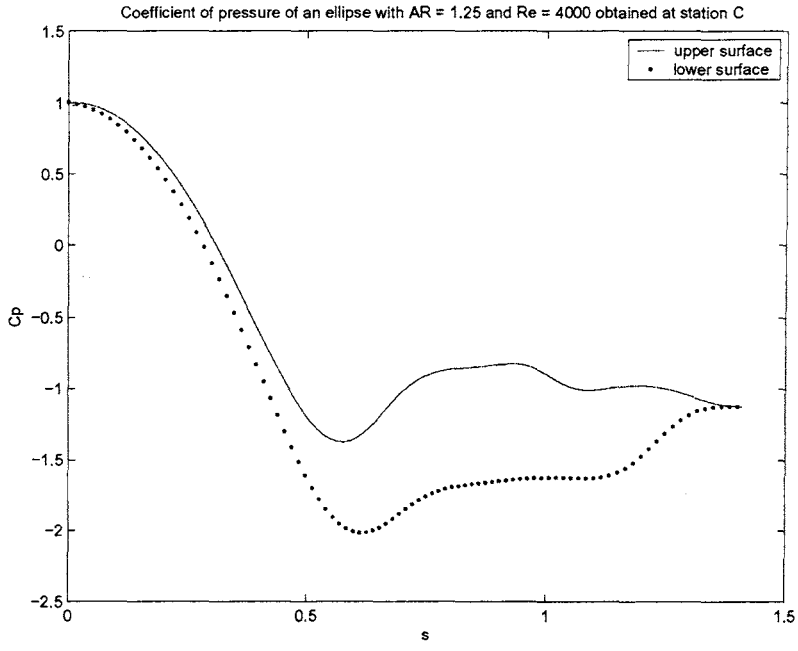

Figure 5.86 Coefficient of pressure for upper and lower surface for an ellipse of AR = 1.25 at t = 5.042s (Station C, first minimum drag point)

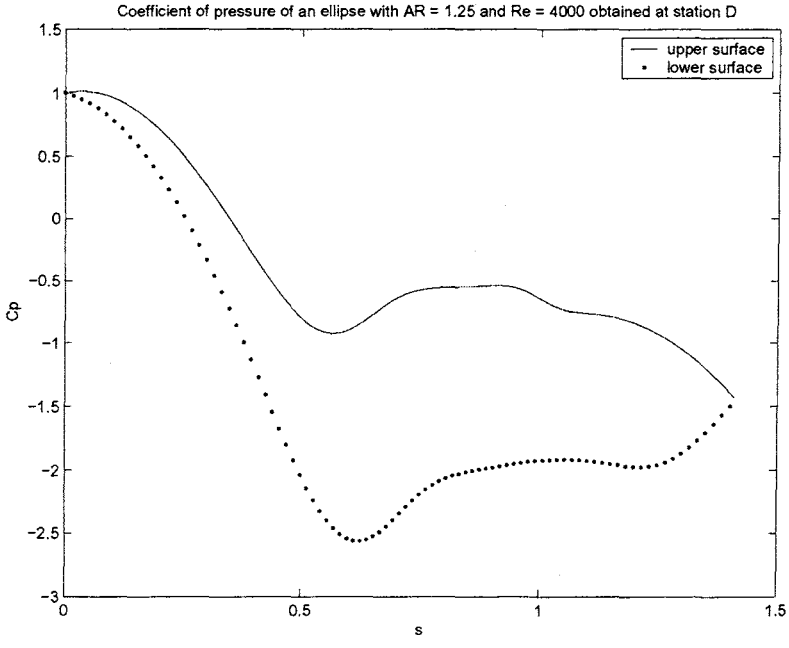

Figure 5.87 Coefficient of pressure for upper and lower surface for an ellipse of AR = 1.25 at t = 5.075s (Station D, growth of top vortex)

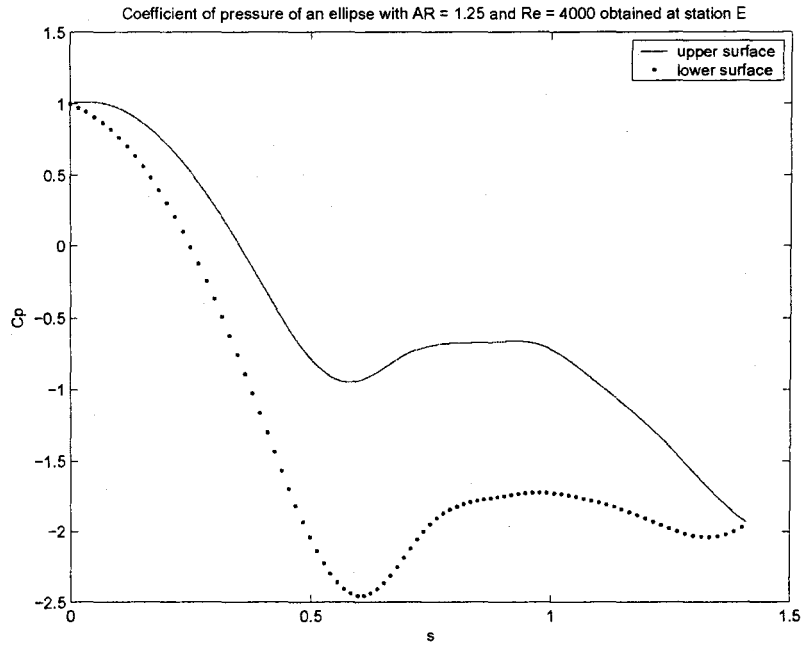

Figure 5.88 Coefficient of pressure for upper and lower surface for an ellipse of AR = 1.25 at t = 5.108s (Station E, top shed)

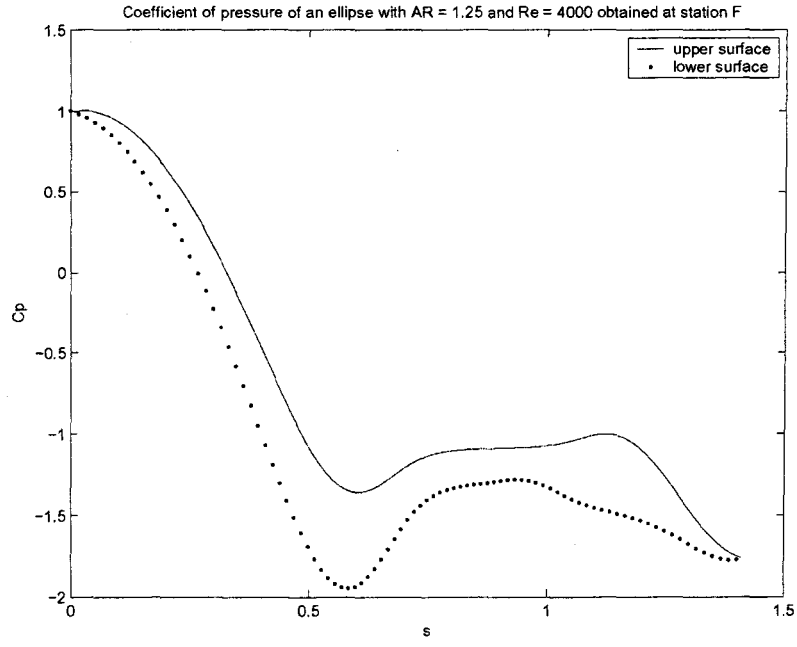

Figure 5.89 Coefficient of pressure for upper and lower surface for an ellipse of AR = 1.25 at t = 5.139s (Station F, growth of bottom vortex)

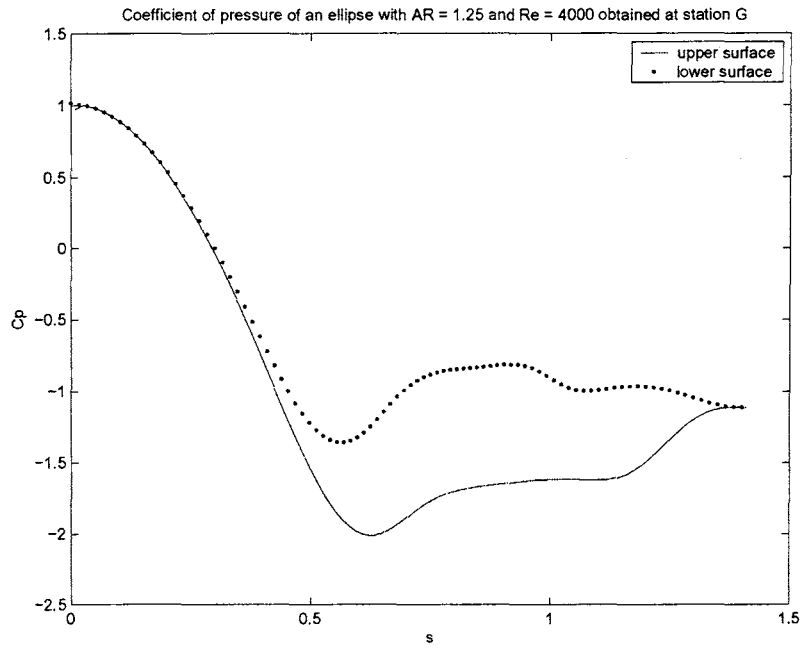

Figure 5.90 Coefficient of pressure for upper and lower surface for an ellipse of AR = 1.25 at t = 5.169s (Station G, second minimum drag point)

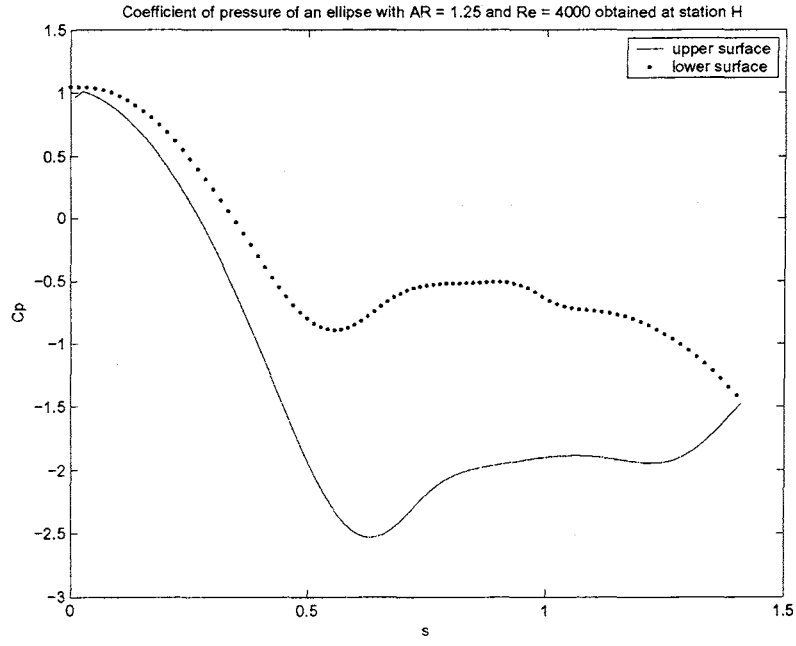

Figure 5.91 Coefficient of pressure for upper and lower surface for an ellipse of AR = 1.25 at t = 5.202s (Station H, growth of bottom vortex)

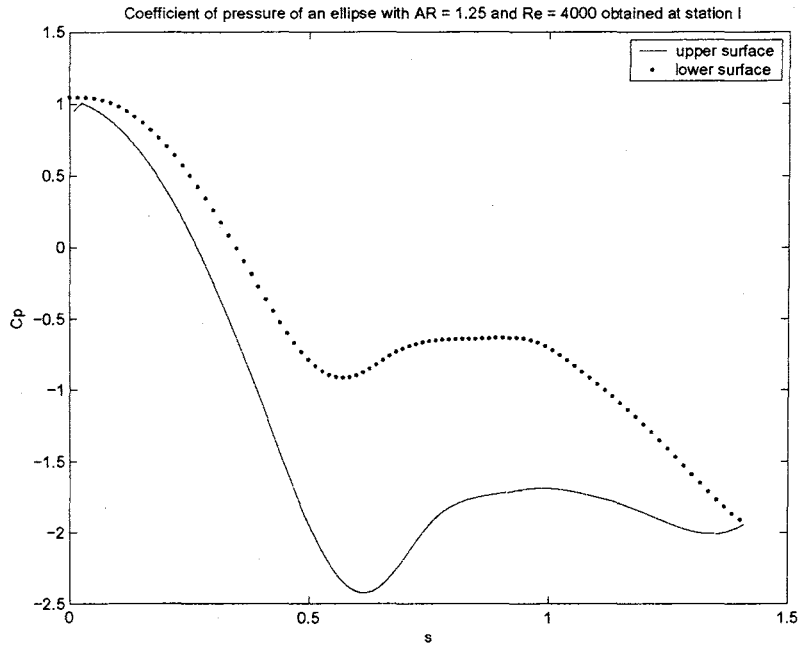

Figure 5.92 Coefficient of pressure for upper and lower surface for an ellipse of AR = 1.25 at t = 5.235s (Station I, bottom shed)

Looking at the C_p plots for the ellipse of aspect ratio 1.25 and the circular cylinder, it could be observed that the the ellipse had a much lower minimum C_p value compared to the circular cylinder. For the ellipse, the lowest C_p value was very close to -2.5, whereas for the circular cylinder, it did not go beyond -1.95. It can be safely concluded that as the aspect ratio increases, the lowest C_p value decreases. Also, at the bottom shed and the top shed, the difference between the two surfaces for the ellipse clearly was much more compared to the circular cylinder case. Again, it could be observed that the variations with time in the right half was much more than the left half for the reason already explained before.

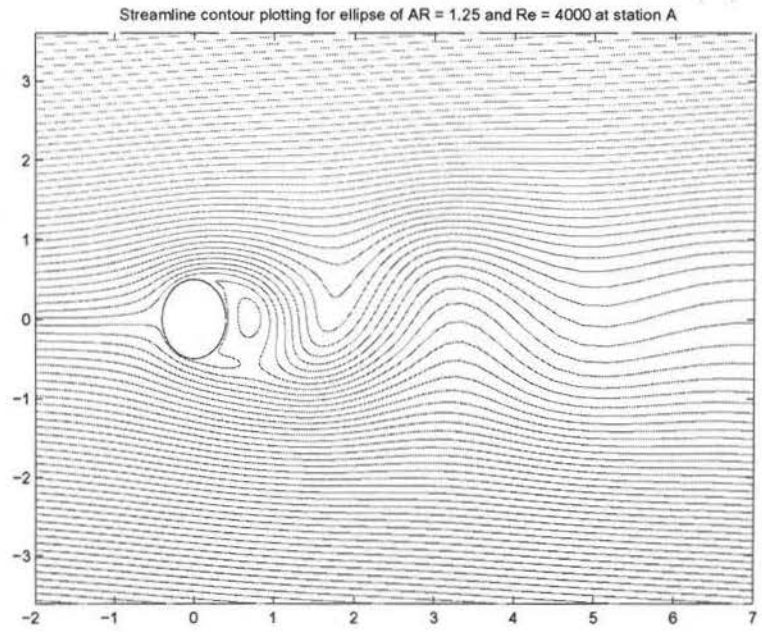

Figure 5.93 Streamline contour plotting for an ellipse of AR = 1.25 at t = 4.981s (Station A, bottom shed)

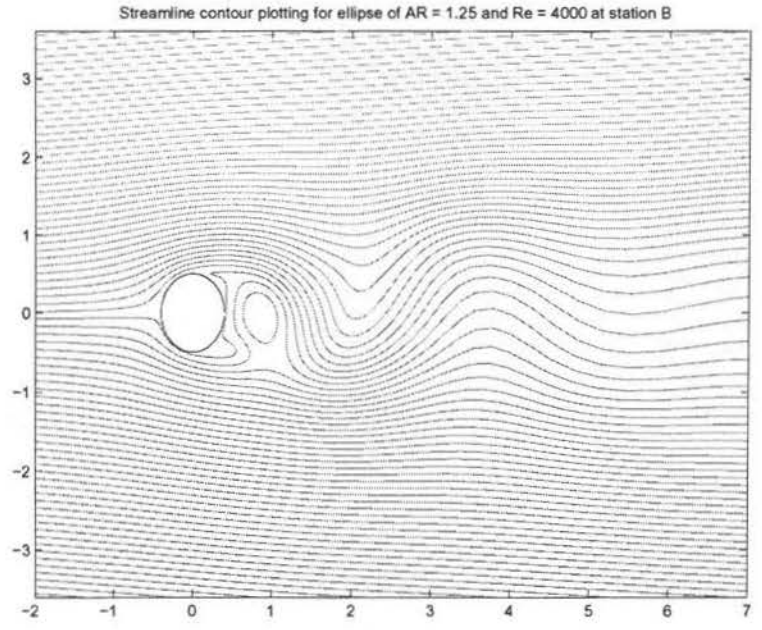

Figure 5.94 Streamline contour plotting for an ellipse of AR = 1.25 at t = 5.012s (Station B, growth of top vortex)

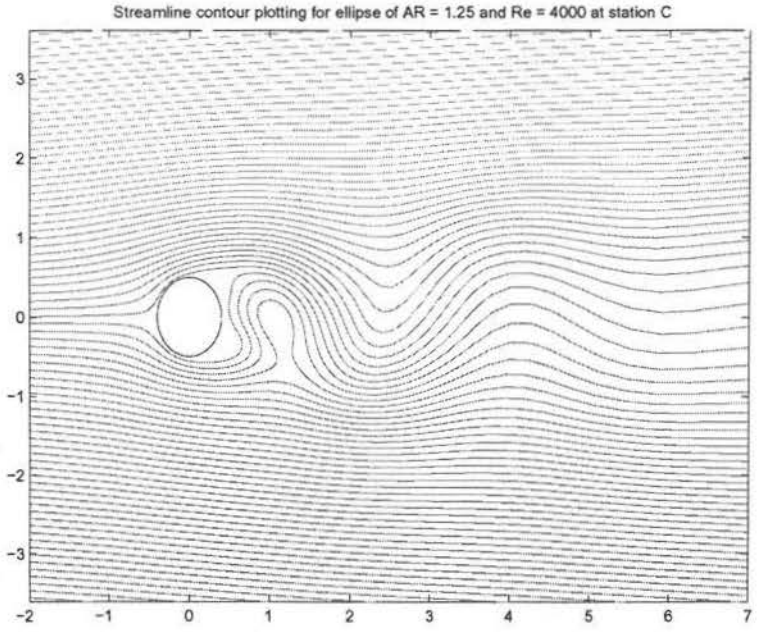

Figure 5.95 Streamline contour plotting for an ellipse of AR = 1.25 at t = 5.042s (Station C, first minimum drag point)

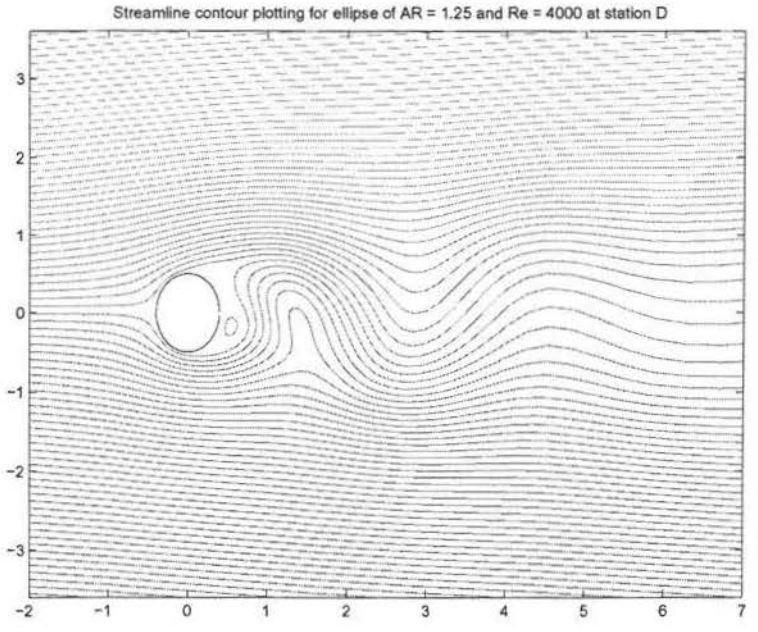

Figure 5.96 Streamline contour plotting for an ellipse of AR = 1.25 at t = 5.075s (Station D, growth of top vortex)

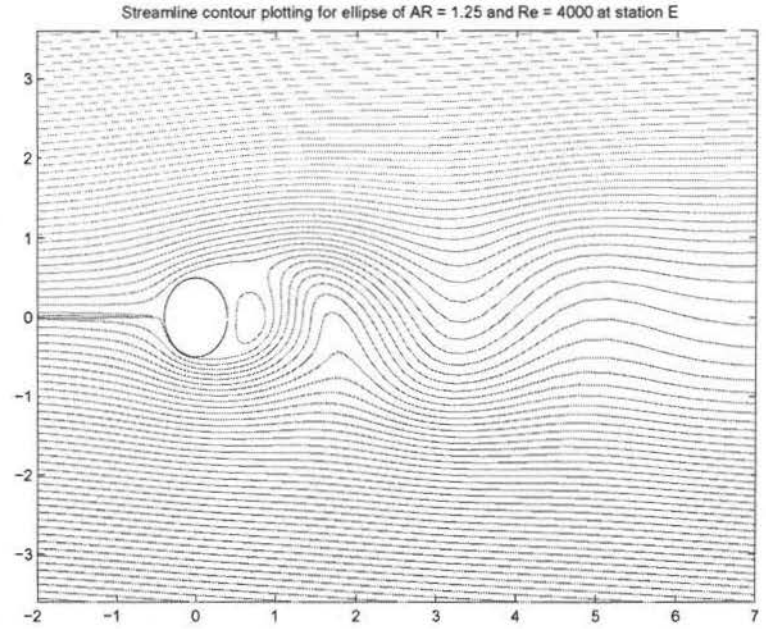

Figure 5.97 Streamline contour plotting for an ellipse of AR = 1.25 at t = 5.108s (Station E, top shed)

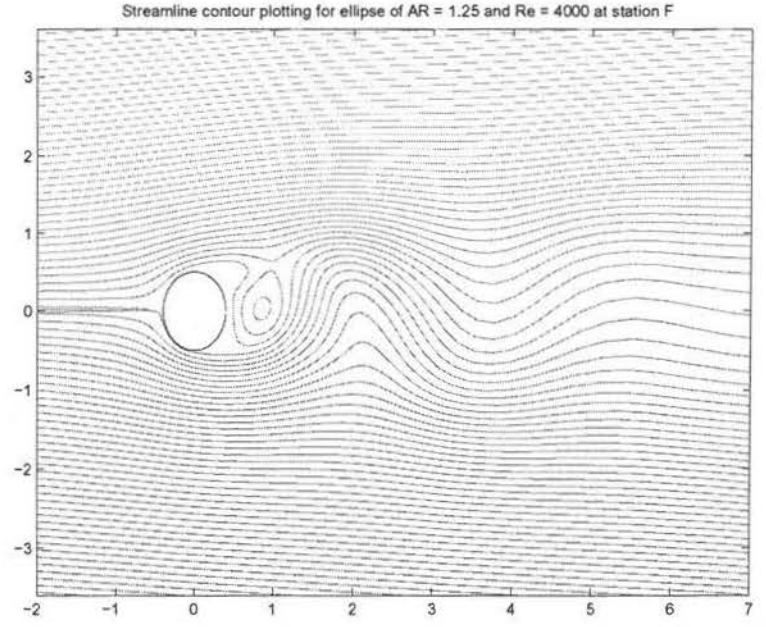

Figure 5.98 Streamline contour plotting for an ellipse of AR = 1.25 at t = 5.139s (Station F, growth of bottom vortex)

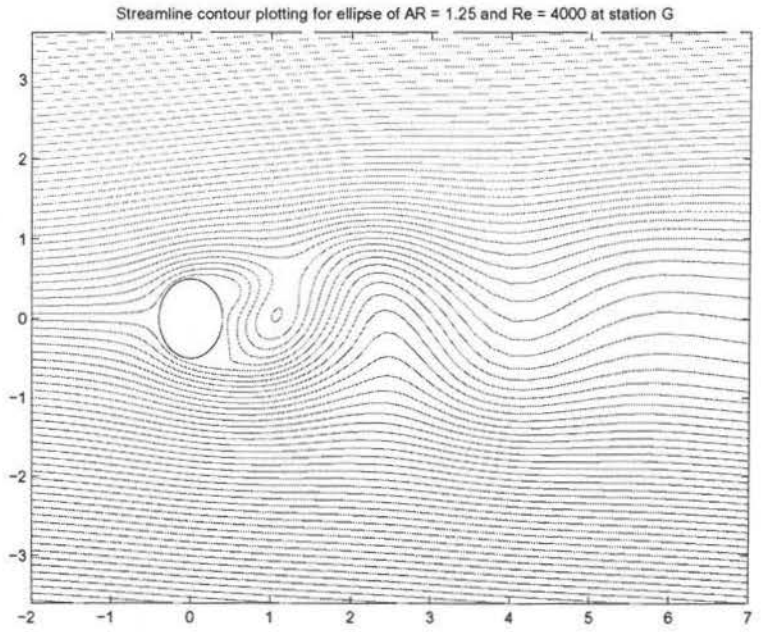

Figure 5.99 Streamline contour plotting for an ellipse of AR = 1.25 at t = 5.169s (Station G, second minimum drag point)

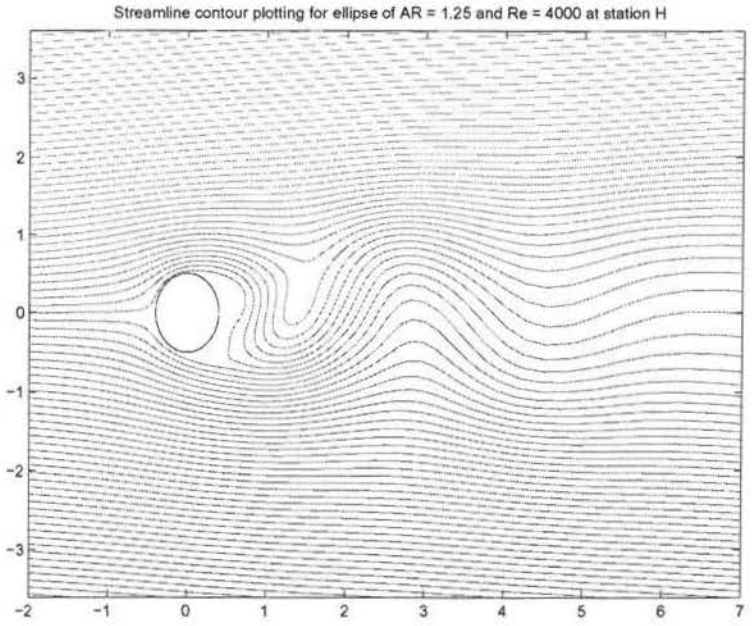

Figure 5.100 Streamline contour plotting for an ellipse of AR = 1.25 at t = 5.202s (Station H, growth of bottom vortex)

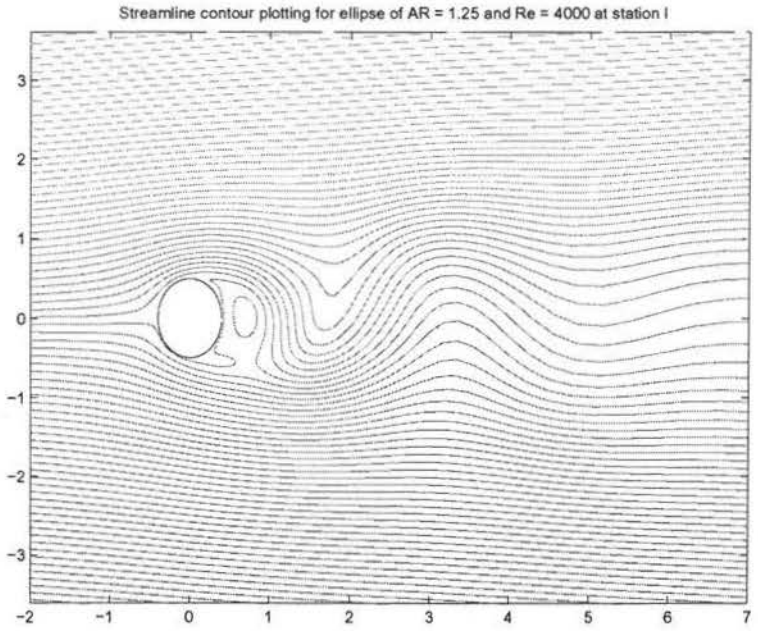

Figure 5.101 Streamline contour plotting for an ellipse of AR = 1.25 at t = 5.235s (Station I, bottom shed)

From the streamline contours, the cycle is clearly a bottom shed to bottom shed cycle. Fig. 5.93 shows the bottom vortex shedding. Figs. 5.94 through 5.96 show the growth of the top vortex. Fig 5.97 is the top vortex shedding. Figs. 5.98 through 5.100 is the growth of bottom vortex again and Fig. 5.101 shows bottom vortex, thus completing the cycle. Again the symmetry is observed as described in the circular cylinder case.

CHAPTER 6 CONCLUSION

As shown in the figure below, for a typical case with a half cylinder, there are no oscillations to be seen. In fact, it was seen in all the unsteady results that there were oscillations with time. So, assuming the flow to be symmetric doesn't really work. Clearly, the flow is seen to be steady for a half cylinder. Also, if one looks at the C_d value, it is .38 for the half cylinder, whereas, for the same Reynolds number, C_d value is 1.18 when a full cylinder is studied.

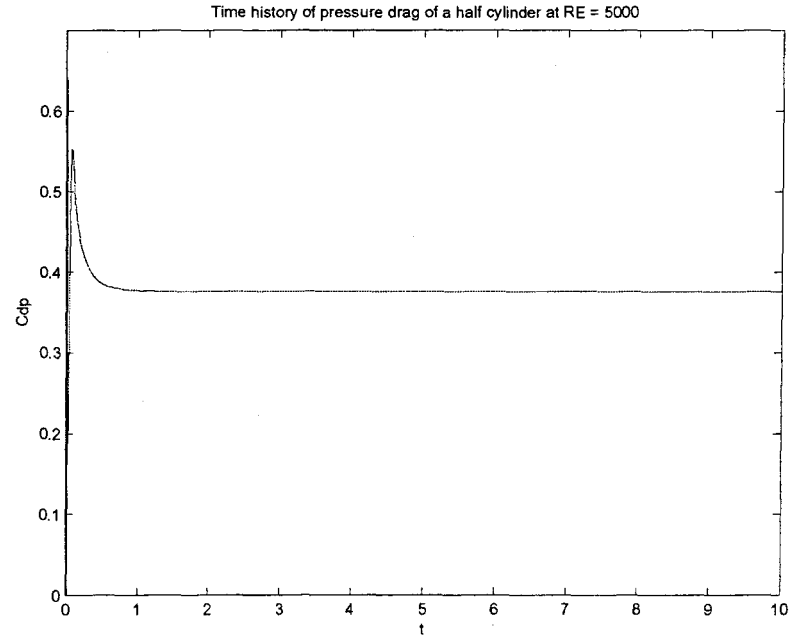

Figure 6.1 Time history of coeficient of pressure drag of a half cylinder for RE = 4000

So, clearly, the full cylinder C_d value is not twice the half cylinder value, and hence,

it could be concluded safely that the half cylinder is not at all a good approximation of the physics of the flow past a full cylinder.

In Fig. 5.3, the C_d's from Fully Implicit and Crank Nicolson were compared to the experimental value found in [40]. The values given by both the schemes were pretty close to the experimental values. However, for higher Reynolds number, clearly, the trend did not match. This could be attributed to the fact that the calculation was done with the assumption that the flow was laminar, but in actuality, for higher Reynolds number, the flow is actually turbulent and hence the trend was not quite the same. It leaves a scope for improvement in the future, and it is believed that with a proper turbulent modeling this discrepancy can be removed. The Strouhal number comparison for both the schemes is shown in Fig. 5.4.

It was observed that both C_p and C_f changed a lot at the back portion of the cylinder, which was in perfect correlation with the streamline contours, where it was clearly seen that the oscillation begins only after θ value exceeds 1.57 radians. This means the recirculating zone actually starts after that point. Before that, the flow is smooth, and the streamlines more or less adhere to the cylinder. Also, it was observed that the C_p and C_f values for the top surface and the bottom surface exchange their relative positions in a cycle, for the zero angle of attack, as in the case here. For example, the top surface C_p values at the time of top vortex shedding would be the same bottom surface C_p value at the time of bottom vortex shedding.

For the elliptic cylinders, it was observed that when the aspect ratio was lesser than 1, the oscillations with time were negligible. Also, the C_d values were very much dependent on the aspect ratio. When the aspect ratio increased, the C_d value increased. As the aspect ratio increases, the body becomes "more bluff" so to say, which essentially means that the obstruction is more and hence more recirculation and more drag. This could be seen clearly if two contour plottings are compared, one being that of a circular cylinder and the other one of the elliptic cylinder. The other interesting aspect to note

with the Fig. 5.73 is that it tends to assymptotically approach some value of C_d. This assymptotic value should be the same as the mean C_d value of a zero thickness flat plate at 90-degree incidence for the same Reynolds number.

In the future, Fully Implicit and Crank Nicolson algorithms can be extended to the compressible flow regime, and flow past an elliptic cylinder can be studied. At the wake of a bluff body, essentially the flow is incompressible in nature. With a pressure-based algorithm used in this study, it is expected that two different phenomenons for compressible and incompressible flow, namely shock capturing and vortex shedding can be simulated.

BIBLIOGRAPHY

[1] Perry, A. E., Chong, M. S. and Lim, T. T., "The Vortex-Shedding Process Behind Two-Dimensional Bluff Bodies," Journal of Fluid Mechanics, vol. 116, pp 77-90, 1982.

[2] Gosman, A.D., Pun, W.M., Runchal, A.K., Spalding, D.B. and Wolfshtein, M., " Heat and Mass Transfer in Recirculating Flow," Academic Press, New York, 1969.

[3] Soh, W.Y. and Goodrich, J.W., "Unsteady Solution of Navier-Stokes Equations," Journal of Computational Physics, vol. 79, 1988.

[4] Patankar, S.V. "Numerical Heat Transfer and Fluid Flow," Hemisphere, New York, 1980

[5] Patankar, S.V. and Spalding, D.A.,"A Calculation Procedure for Heat, Mass and Momentum Transfer in Three-Dimensional Parabolic Flows, " International Journal of Heat and Mass Transfer, vol. 15, pp 1787-1806, 1972.

[6] Chorin, A.J., "A Numerical Method for Solving Incompressible Viscous Flow Problems," Journal of Computational Physics, vol. 2, 1967.

[7] Van Doormaal, J. P., and Raithby, G. D., "Enhancements of the SIMPLE Method for Predicting Incompressible Fluid Flows," Numerical Heat Transfer, vol. 7, pp 147-163, 1984.

[8] Van Doormal, J. P. and Raithby, G. D., "An Evaluation of the Segregated Approach for Predicting Incompressible Fluid Flow," ASME Paper 85-HT-9, 1985.

[9] Thiart, G. D., "Finite Difference Scheme for the Numerical Solution of Fluid Flow and Heat Transfer Problems on NonStaggered Grids," Numerical Heat Transfer, Part B, vol. 17, pp 43-62, 1990.

[10] Shih, T. M., and Ren, A. L., "Primitive-Variable Formulations Using NonStaggered Grids," Numerical Heat Transfer, vol. 7, pp 413-428, 1984.

[11] Rhie, C.H. and Chow, W.L., "A Numerical Study of the Turbulent Flow Past an Isolated Airfoil with Trailing Edge Separation," AIAA Journal, vol. 21 pp 1525-1532, 1983.

[12] Yen, R. H. and Liu, C. H., "Enhancement of the SIMPLE Algorithm by an Additional Explicit Corrector Step," Numerical Heat Transfer, Part B, vol. 24, pp 127-141, 1993.

[13] Majumdar, S., "Role of Underrelaxation in Momentum Interpolation for Calculation of Flow with NonStaggered Grids," Numerical Heat Transfer, vol. 13, pp 125-132, 1988.

[14] Acharya, S. and Moukalled, F., "Improvements to Incompressible Flow Calculation on a Non-staggered Curvilinear Grid," Numerical Heat Transfer, Part B, vol. 15, pp 131-152, 1989.

[15] Issa, R. I., "Solution of the Implicit Discretized Fluid Flow Equations by Operator Splitting," Mechanical Engineering Rep. FS/82/15, Imperial College, London, 1982.

[16] Maliska, C. R. and Raithby, G. D., "Calculating 3-D Fluid Flows Using Non-orthogonal Grid," Procedures of Third International Conference on Numerical Methods in Laminar and Turbulent Flows, Seattle, WA, pp 656-666, 1983.

[17] Shaw, G. J. and Sivalogonathan, S., "The SIMPLE Pressure Correction Method as a Nonlinear Smoother," in S. F. Mccormick(ed.), Multigrid Methods: Theory, Applications and Supercomputing. LNPAM vol. 110, pp 579-596, Marcel Dekker, New York, 1988.

[18] Gjesdal, T. and Lossius, M. E. H., "Comparison of Pressure Correction Smoothers for Multigrid Solution of Incompressible Flow," International Journal of Numerical Methods in Fluids, vol. 25, pp 393-405, 1997.

[19] Yu, B., Ozoe, H. and Tao, W. Q., "A Modified Pressure-Correction Scheme for the SIMPLER Method, MSIMPLER," Numercial Heat Transfer, Part B, vol. 39, pp 435-449, 2001.

[20] Karki, K. C., "A Calculation Procedure for Viscous Flows at All Speeds in Complex Geometries," Ph.D Dissertation, University of Minnesota, 1986.

[21] Moukalled, F. and Darwish, M., "A Unified Formulation of the Segregated Class of Algorithms for Fluid Flow at All Speeds," Numerical Heat Transfer, Part A, vol. 37, pp 103-139, 2000.

[22] Mathur, S. R. and Murthy, J. Y., "A Pressure-Based Method for Unstructured Meshes," Numerical Heat Transfer, Part B, vol. 31, pp 195-215, 1997.

[23] Kang, S. and Kim, Y., "Pressure-Based Unstructured-Grid Finite-Volume Method for Simulating Laminar Reacting Flows," Numerical Heat Transfer, Part B, vol. 41, pp 53-72, 2002.

[24] Hutchinson, B. R. and Raithby, G. D., "A Multigrid Based on Additive Correction Strategy," Numerical Heat Transfer, vol. 9, pp511-537, 1986.

[25] Yu, B., Tao, W. Q., Wei, J. J., Kawaguchi, Y., Tagawa, T. and Ozoe, H., "Discussion on Momentum Interpolation Method for Collocated Grids of Incompressible Flow," Numerical Heat Transfer, Part B, vol. 42 pp 141-166, 2002.

[26] Warming, R. F. and Beam, R. M., "Upwind Second-Order Difference Schemes and Applications in Aerodynamic Flows," AIAA Journal, vol. 14, pp 1241-1249, 1976.

[27] Leonard, B. P., "A Stable and Accurate Convective Modeling Procedure Based on Quadratic Upstream Interpolation," Computational Methods in Applied Mechanical Engineering, vol. 19, pp 59-98, 1979.

[28] Rajagopalan, R. G. and Yu, C. J., "Use of Lagrange Interpolation in Modeling Convective Kinematics," Numerical Heat Transfer, Part B, vol. 36, pp 233-240, 1999.

[29] Rai, M. M., "Navier-Stokes Simulation of Blade-Vortex Interaction Using High-Order Accurate Upwind Scemes," AIAA Paper 87-0543, 1987.

[30] Chin, K.L. "Numerical simulation of non-lifting flow over two-dimensional elliptic cylinders," MS Thesis, Iowa State University, 1991.

[31] Sutikno, Wirogo, "Flux Correction Method: An Accurate Approach to Fluid Flow Modeling," Ph.D Dissertation, Iowa State University, 1997.

[32] Kelkar, K. M., "Numerical Study of Stability of Fluid Motion," Ph.D. Thesis, University of Minnesota, 1988.

[33] Cebeci, T. "Calculation of Three-Dimensional Boundary Layers-II. Three - Dimensional Flows in Cartesian Coordinates," AIAA Journal, vol. 13, pp 1056-1064, 1975.

[34] Dyke, M.V. "An Album of Fluid Motion," The Parabolic Press, Stanford, California, 1988.

[35] Harlow, F.H. and J.E. , "Numerical Calculation of Three-Dimensional Time Dependent Viscous Incompressible Flow of Fluid with Free Surface," Physics of Fluids, vol. 8, pp 2182, 1965.

[36] Caretto, L.S., Curr, R.M. and Spalding, D.B.,"Two Numerical Methods for Three-Dimensional Boundar Layers," Computer Methods in Applied Mechanics and Engineering, vol. 1, pp 39, 1972.

[37] Zori, Laith, "Towards All Speeds Euler/Navier-Stokes Flow Solutions on Unstructured Meshes," Ph.D Dissertation, Iowa State University, 1996.

[38] Purohit, Prabir, "Comparative Study of Two Schemes for Time Accurate Viscous Incompressible Flows," MS Thesis, Iowa State University, 2000.

[39] Anderson, D. A., Tannehill, J. C. and Pletcher, R. H., "Computational Fluid Dynamics and Heat Transfer," McGraw-Hill Book Company, New York, 1984.

[40] Schilichting, H., "Boundary Layer Theory," McGraw-Hill Book Company, New York, 1968.

[41] Kelkar, K. M. and Patankar, S. V., "Numerical Prediction of Vortex Shedding Behind a Square Cylinder," International Journal for Numerical Methods in Fluids, vol. 14, pp 327-341, 1992.

[42] Jackson, C. P., "A Finite Element Study of the Onset of Vortex Shedding in Flow Past Variously Shaped Bodies," Journal of Fluid Mechanics, vol. 182, pp 23-45, 1987.

[43] Ghia, U., Ghia, K. N. and Shin, C. T., "High-Re Solutions for Incompressible Flow Using the Navier-Stokes Equations and a Multigrid Method," Journal of Computational Physics, vol. 48, pp 387-411, 1982.

[44] Giannakoglou, K. C. and Politis, E. S., "A Pressure Correction Scheme Using Coupled Momentum Equations," Numercial Heat Transfer, Part B, vol. 32, pp 419-435, 1997.

[45] Spalding, D. B., "Mathematical Modelling of Fluid Mechanics, Heat Transfer and Mass Transfer Processes," Mechanical Engineering Department, Rep. HTS/80/1, Imperial College of Science, Technology and Medicine, London, 1980.